Cr_2Nb-BASED ALLOY DEVELOPMENT

C. T. Liu, P. F. Tortorelli, J. A. Horton, D. S. Easton, J. H. Schneibel,
L. Heatherly, C. A. Carmichael, M. Howell, and J. L. Wright

Oak Ridge National Laboratory
Oak Ridge, Tennessee 37831

ABSTRACT

Two-phase Cr-Cr_2Nb alloys (designated as CN alloys) were prepared by arc melting, followed by directional solidification, HIPping, or hot extrusion at 1450 to 1500°C. The microstructure of CN alloys containing 6 to 12 at.% Nb depended strongly on alloying additions, heat treatment, and material processing. Tensile properties were sensitive to defects. Hot extrusion at 1480°C was most effective in reducing as-cast defects and refining the cast Cr-Cr_2Nb eutectic structure and thus improving ductility. Beneficial alloying elements that modified the eutectic microstructure, improved oxidation resistance, or increased high-temperature strength were identified. One particular composition had a room-temperature fracture strength of 548 MPa and an ultimate tensile strength of 388 MPa, and 23% elongation at 1200°C. Another CN alloy showed a fracture toughness of 7.6 MPa$\sqrt{m}$ at room temperature and 24.4 MPa$\sqrt{m}$ at 1000°C. Silicide coatings applied by a pack cementation process substantially improved the oxidation resistance of the Cr-Cr_2Nb alloys at 950 and 1100°C.

INTRODUCTION

The objective of this task is to develop a new generation of structural materials based on intermetallic alloys for use as critical hot components in advanced fossil energy conversion systems. The intermetallic phase, Cr_2Nb, with a complex cubic structure (C-15)[1,2] has been selected for this development because of its high melting point (1770°C),[2-4] relatively low material density (7.7 g/cm^2),[5] excellent high-temperature strength (at 1000 to 1250°C),[6,7] and potential resistance to oxidation and corrosion.[3,8,9] This intermetallic phase, like many other Laves phases, has a wide range of compositional homogeneity[2,4] suggesting the possibility of improving its mechanical and metallurgical properties by alloying additions.

The major engineering concern with Cr_2Nb and other A_2B Laves phases is their poor fracture toughness and fracture resistance at ambient temperatures.[3,6,7,10] The single-phase Cr_2Nb is very hard (~800 DPH) and brittle at room temperature.[11] Because of this brittleness, the development effort has concentrated on two-phase structures containing the hard intermetallic phase Cr_2Nb and the softer Cr-rich solid solution phase. Previous studies indicate that the two-phase CN alloys exhibited significant plastic deformation prior to fracture under compressive tests at room temperature.[6,7,11] The alloys showed excellent compressive strength at room and elevated temperatures, with the yield strength much superior to nickel-base superalloys and Ni_3Al alloys at and above 1000°C. The CN alloys, however, showed poor fracture strength in tension at ambient temperatures.

Potential applications of $Cr-Cr_2Nb$ alloys include hot components (for example, air heat exchangers and turbine blades) in advanced energy conversion systems and heat engines, wear-resistant parts in coal handling systems (e.g., nozzles), drill bits for oil/gas wells, and valve guides in diesel engines. Current studies are focused on enhancement of fracture resistance in tension at ambient temperatures and oxidation resistance above 1000°C. This report summarizes recent progress on controlling microstructure and improving the mechanical and metallurgical properties and the high-temperature corrosion behavior of $Cr-Cr_2Nb$ alloys through alloying additions, material processing, and heat treatment.

ALLOY PREPARATION AND PROCESSING

$Cr(Nb)-Cr_2Nb$ alloys weighing 400 g were prepared by arc melting and drop casting in a copper mold (2.5 cm diam x 7.6 cm long) preheated at 100 to 300°C. High-purity niobium and chromium metal chips were used as charge materials. The alloy ingots generally contain certain defects, including oxide inclusions and as-cast porosity ranging in size from a few to several hundred microns. The alloys also exhibit a coarse eutectic structure including interconnected Cr_2Nb plates, which adversely affect their mechanical (tensile) properties.

In order to minimize the casting defects and to refine the cast eutectic structure, selected alloy ingots were clad inside molybdenum billets and hot extruded at 1450 to 1500°C at an extrusion ratio of 4 to 1. Some alloys were successfully hot extruded into 1.3 cm bar stock, and others were cracked into pieces. The tendency for cracking was not simply correlated with alloy composition. It appeared that the cracking may be related to casting defects.

Preparation of CN alloys using elemental powders has just been initiated. In this case, the powders were mixed completely to give the correct alloy compositions and then placed inside molybdenum cans. The filled cans were then degassed in a vacuum chamber and sealed by electron-beam welding. They were hot extruded at 1480°C to produce CN alloys. Initial results indicate the as-extruded bars contained many foreign particles which were identified as aluminum and niobium oxides by energy dispersive x-ray spectroscopy (EDS). The amount of the oxide phase depended on the way the powders were prepared prior to insertion into the molybdenum cans. Significant recent progress was made in decreasing the amount of the oxide phases by reducing interstitial contamination during the powder processing.

MICROSTRUCTURAL ANALYSIS

Alloying additions, heat treatment, and material processing all strongly affect the microstructure of Cr(Nb)-Cr_2Nb alloys. Figure 1 compares the as-cast microstructure of two alloys, CN-96 and -97 containing 12% Nb and other alloying additions. (All compositions are at.% unless otherwise noted.) The compositional difference of the two alloys is that CN-97 had 0.1 wt% of a minor alloying addition (designated as X5). As shown in Fig. 1, the base alloy CN-96 exhibits a typical lamellar-type eutectic structure (Fig. 1a) while the doped alloy CN-97 shows blocky particles in the eutectic structure. In these photos, the Cr-rich phase appears as light gray while the Cr_2Nb is darker. The primary Cr-rich patches precipitated out fine Cr_2Nb particles after annealing at 1200 to 1300°C (as shown in Fig. 2 for CN-103).

Hot extrusion at 1450 to 1500°C was apparently effective in breaking the interconnected Cr_2Nb phase in the eutectic structure. This is shown in Fig. 3 for CN-90 containing 6% Nb and other alloying additions. The coarse Cr_2Nb plates that formed around primary Cr-rich patches (Fig. 3a) were broken into blocky particles (Fig. 3b) after hot extrusion at 1480°C.

The alloys CN-80, -85, and -87 were examined by transmission electron microscopy (TEM). All the alloys were hot extruded at 1480°C and annealed for 3 d at 1200°C. Alloy disks were prepared by ion milling at 6 kV and were examined in a Philips CM30 at 300 kV. Figure 4 is a TEM micrograph showing Cr_2Nb particles observed in CN-85 which was annealed for 3 d at 1200°C. The blocky particles contain numerous microtwins. This may be due to the C14 → C15 transformation. The study of the crystal structure of these particles

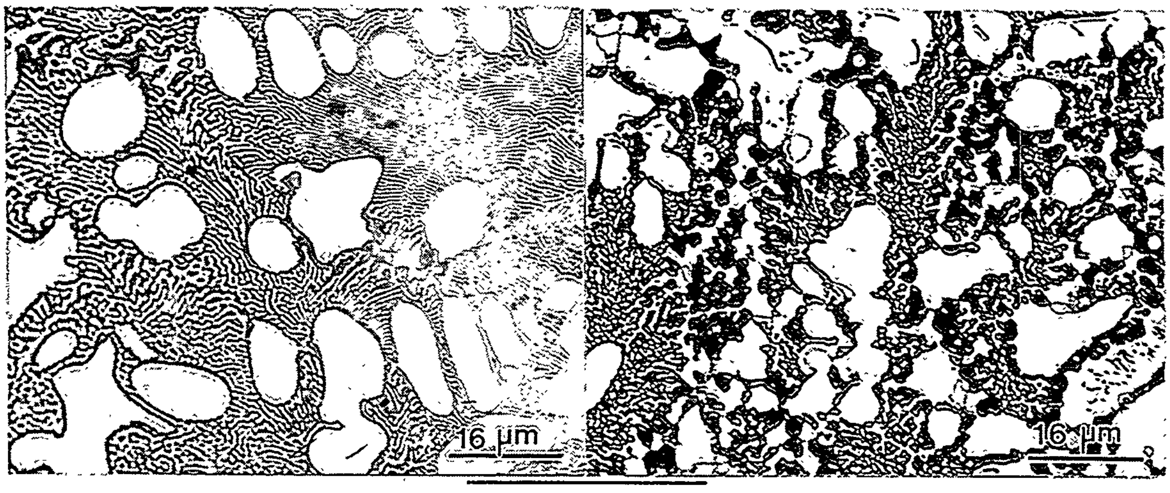

(a) (b)

Fig. 1. Optical micrograph of as-cast (a) CN-96 and (b) CN-97 containing 12 at.% Nb and other alloying additions. The difference in composition is that CN-97 has 0.1 wt% X5.

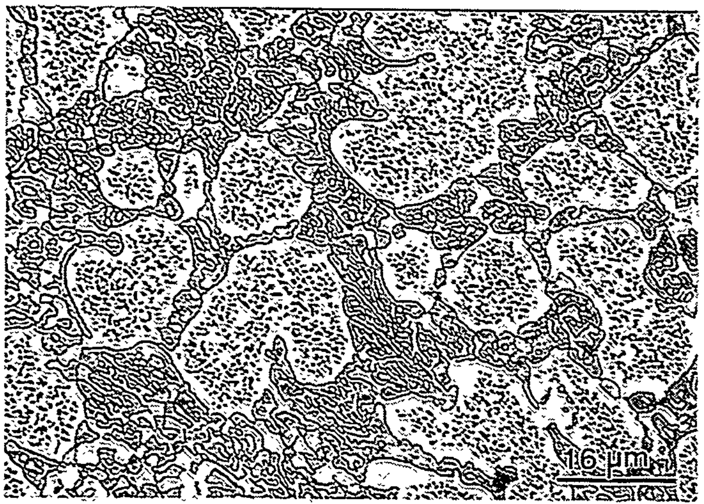

Fig. 2. Optical micrograph of CN-103 containing 10 at.% Nb and 0.1 wt% X5. The alloy was annealed for 1 d at 1300°C and 2 d at 1200°C.

---

in CN-80, -85, and -87 dissolves a small amount (≤1%) of niobium. The Cr_2Nb-type phase, on the other hand, contains more than 27% Nb, and the exact amount of niobium in this phase depends on the partitioning of alloying additions in the CN alloys. The element X1 partitions more or less equally in the Cr_2Nb and the Cr-rich phases in CN-80 and -85, and preferentially in the Cr_2Nb phase in CN-87 (containing 20% X4). A careful examination of the Cr_2Nb compositions suggest X1 essentially occupies the chromium subsites. The element X2 in CN-85 and -87 partitions strongly in the Cr_2Nb-type phase, as shown in Table 1. The element X4 was distributed roughly equal in the two phases in CN-87. The partitioning behavior of these alloying elements could not be rationalized by considering both reactivity and atomic size of the alloying elements.

TENSILE PROPERTIES

Button-type tensile specimens with gage dimensions 0.31 cm diam x 0.95 cm long were machined by electro-discharge machining, followed by grinding. The tensile specimens

MICROSTRUCTURAL ANALYSIS

Alloying additions, heat treatment, and material processing all strongly affect the microstructure of Cr(Nb)-Cr_2Nb alloys. Figure 1 compares the as-cast microstructure of two alloys, CN-96 and -97 containing 12% Nb and other alloying additions. (All compositions are at.% unless otherwise noted.) The compositional difference of the two alloys is that CN-97 had 0.1 wt% of a minor alloying addition (designated as X5). As shown in Fig. 1, the base alloy CN-96 exhibits a typical lamellar-type eutectic structure (Fig. 1a) while the doped alloy CN-97 shows blocky particles in the eutectic structure. In these photos, the Cr-rich phase appears as light gray while the Cr_2Nb is darker. The primary Cr-rich patches precipitated out fine Cr_2Nb particles after annealing at 1200 to 1300°C (as shown in Fig. 2 for CN-103).

Hot extrusion at 1450 to 1500°C was apparently effective in breaking the interconnected Cr_2Nb phase in the eutectic structure. This is shown in Fig. 3 for CN-90 containing 6% Nb and other alloying additions. The coarse Cr_2Nb plates that formed around primary Cr-rich patches (Fig. 3a) were broken into blocky particles (Fig. 3b) after hot extrusion at 1480°C.

The alloys CN-80, -85, and -87 were examined by transmission electron microscopy (TEM). All the alloys were hot extruded at 1480°C and annealed for 3 d at 1200°C. Alloy disks were prepared by ion milling at 6 kV and were examined in a Philips CM30 at 300 kV. Figure 4 is a TEM micrograph showing Cr_2Nb particles observed in CN-85 which was annealed for 3 d at 1200°C. The blocky particles contain numerous microtwins. This may be due to the C14 → C15 transformation. The study of the crystal structure of these particles

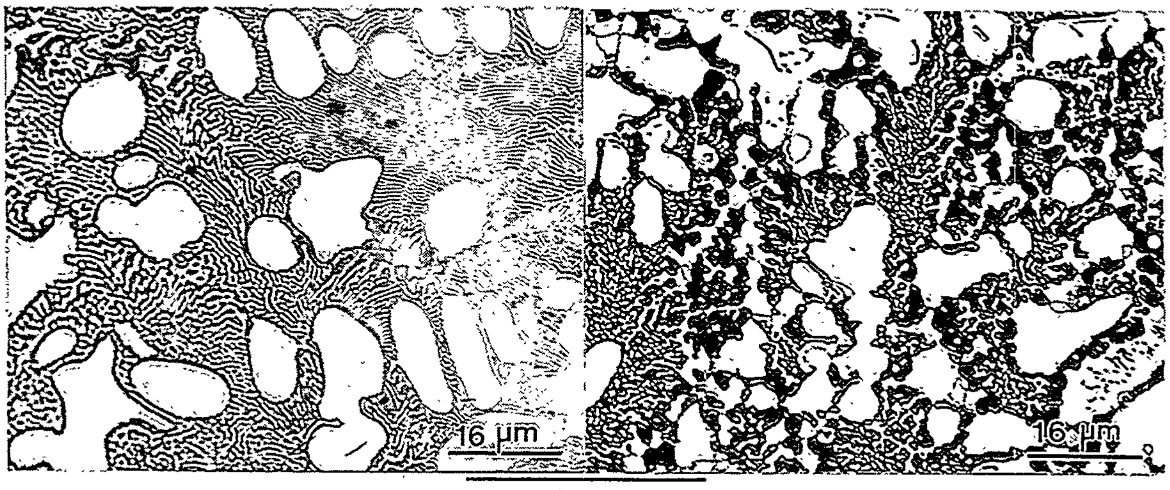

(a) (b)

Fig. 1. Optical micrograph of as-cast (a) CN-96 and (b) CN-97 containing 12 at.% Nb and other alloying additions. The difference in composition is that CN-97 has 0.1 wt% X5.

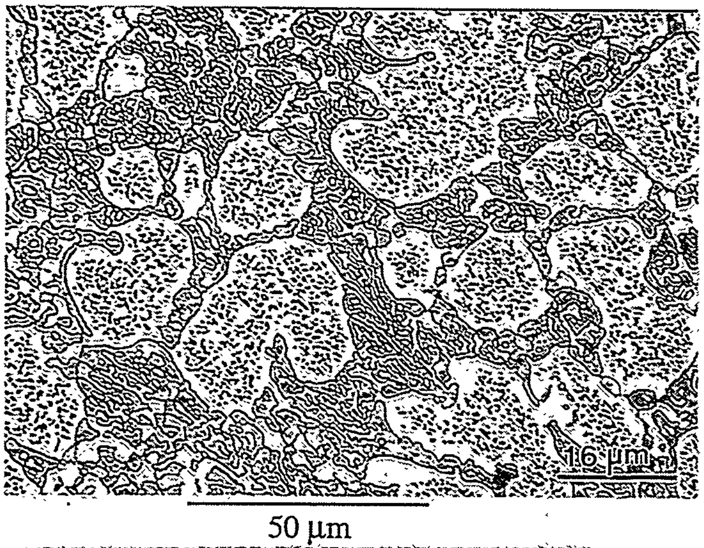

Fig. 2. Optical micrograph of CN-103 containing 10 at.% Nb and 0.1 wt% X5. The alloy was annealed for 1 d at 1300°C and 2 d at 1200°C.

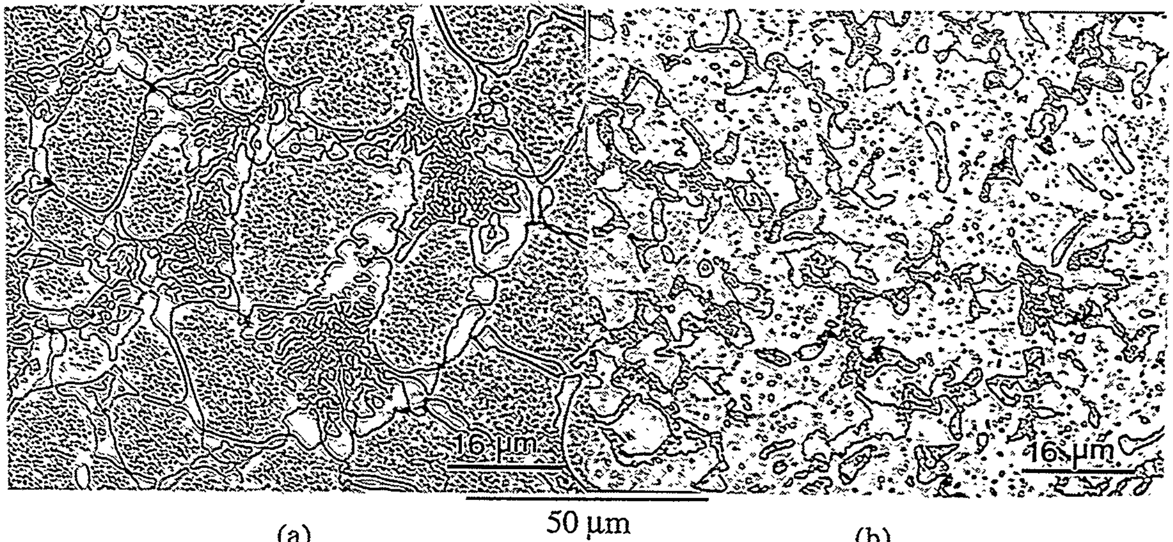

(a) (b)

Fig. 3. Comparison of optical micrograph of CN-90 in (a) as-cast plus 1 d at 1200°C anneal and (b) hot extrusion at 1480°C plus 1 d at 1200°C anneal.

is in progress. Dislocations and dislocation networks are generally observed in the Cr-rich phase, but they are very seldom observed in Cr_2Nb particles.

An EDAX 9100 spectrometer was used to perform EDS in conjunction with the TEM studies. The EDS analyses were made on precipitates that intersected the ion milling perforations, thereby minimizing the contributions from surrounding matrix material. The results were averaged and are shown in Table 1. Here X1, X2, X3, and X4 represent the beneficial elements added to the Cr-Nb alloys. X1 was added for refining the coarse eutectic structure, X2 was for improving oxidation resistance, X3 for enhancing the high-temperature strength, and X4 for ease of fabrication. The Cr-rich solid solution (that is, the matrix phase)

Fig. 4. TEM micrograph of CN-85 (Cr-Nb-1.5Al-5X1-4X2) hot extruded at 1480°C.

Table 1. Partitioning of Alloying Additions in CN Alloys* as Determined by EDS/TEM

Alloy (at. %)	Cr_2Nb Phase (at. %)	Cr-rich Matrix (at. %)
CN-80: Cr-12Nb-1.5Al-6X1	Nb = 33 Cr = 59 X1 = 6 Al = 2	Nb = 1 Cr = 90 X1 = 8 Al = 1
CN-85: Cr-6Nb-1.5Al-5X1-4X2	Nb = 32 Cr = 51 X1 = 7 X2 = 10 Al = 0	Nb = 1 Cr = 90 X1 = 6 X2 = 1.5 Al = 1.5
CN-87: Cr-8Nb-1.5Al-5X1-4X2-20X4	Nb = 27 Cr = 27 X1 = 10 X2 = 10 X4 = 24 Al = 2	Nb = 0.4 Cr = 73.5 X1 = 4.8 X2 = 2.3 X4 = 16.5 Al = 2.5

*The alloys were fabricated by hot extrusion at 1480°C and annealed for 1 to 3 d at 1200°C.

in CN-80, -85, and -87 dissolves a small amount (≤1%) of niobium. The Cr_2Nb-type phase, on the other hand, contains more than 27% Nb, and the exact amount of niobium in this phase depends on the partitioning of alloying additions in the CN alloys. The element X1 partitions more or less equally in the Cr_2Nb and the Cr-rich phases in CN-80 and -85, and preferentially in the Cr_2Nb phase in CN-87 (containing 20% X4). A careful examination of the Cr_2Nb compositions suggest X1 essentially occupies the chromium subsites. The element X2 in CN-85 and -87 partitions strongly in the Cr_2Nb-type phase, as shown in Table 1. The element X4 was distributed roughly equal in the two phases in CN-87. The partitioning behavior of these alloying elements could not be rationalized by considering both reactivity and atomic size of the alloying elements.

TENSILE PROPERTIES

Button-type tensile specimens with gage dimensions 0.31 cm diam x 0.95 cm long were machined by electro-discharge machining, followed by grinding. The tensile specimens were polished by "0"-grade Emery paper and tested in an Instron testing machine at room temperature in air and at 1200°C in vacuum at a crosshead speed of 0.25 cm/min. Since the tensile properties are sensitive to defects in the alloys, the CN alloys at room temperature were tested using different fabrication conditions to show the defect effect. Table 2 summarizes the tensile results for CN alloys in as-cast, directionally solidified, hot-isostatically pressed (HIPped), and hot extruded conditions. Note that all the specimens were annealed 1 to 3 d at 1200°C prior to tensile testing.

The alloy Cr-5.6Nb-1.5Al-6X1 prepared by arc melting showed a fracture strength at room temperature of 143 MPa. The fracture strength increased to 294 MPa when the alloy was prepared by directional solidification via levitation-zone remelting at the University of Tennessee. The strength further increased to 399 MPa when the arc-cast material was HIPped at 1480°C at 413 MPa (60 ksi). HIPping was used to reduce cast defects in the CN alloys. The best fracture strength at room temperature was obtained for a specimen produced by hot extrusion at 1480°C, which supposedly further reduced cast defects and refined the cast microstructure in CN alloys. A fracture strength as high as 548 MPa was obtained for hot-extruded Cr-12Nb-1.5Al-6X1 (CN-80).

At 1200°C, the CN alloys exhibited significant plastic deformation in tension, with 23% elongation for CN-80, which also had excellent strength at this temperature (see Table 2). For comparison, the strength of Ni-base superalloys, the state-of-the-art high-temperature materials, drops to almost nil at 1200°C. The strength appeared to increase with the niobium

Table 2. Effect of Processing and Alloy Composition on Tensile Properties of CN Alloys

Alloy Composition	Processing*	Fracture Strength (MPa)	Yield Strength (MPa)	Elongation (%)
		Room Temperature		
Cr-5.6Nb-1.5Al-6X1	AM	143		
Cr-5.6Nb-1.5Al-6X1	DS	294		
Cr-5.6Nb-1.5Al-6X1	HIP	399		
Cr-6.0Nb-1.5Al-5X1-4X2 (CN-90)	HE	435		
Cr-12Nb-1.5Al-6X1 (CN-80)	HE	548		
		1200°C		
Cr-6.0Nb-1.5Al-5X1-4X2-2X3 (CN-90)	HE	384	302	13.4
Cr-10Nb-1.5Al-5X1-4X2 (CN-89)	HE	269	238	1.6
Cr-12Nb-1.5Al-6X1 (CN-80)	HE	388	290	23.0

*AM = arc melt; DS = directional solidification; HIP = hot isostatic pressing; HE = hot extrusion at 1480°C.

concentration (or the amount of the Cr_2Nb phase). The data suggest that alloying with 2% X3 significantly increases the strength of CN alloys at 1200°C.

The fracture mode of CN-80 was examined by scanning electron microscopy (SEM). The alloy showed a mixture of both brittle cleavage fracture and intergranular fracture at room temperature. On the other hand, it exhibited a ductile fracture with a dimple appearance at 1200°C. It is known that Cr-based alloys can be embrittled by as little as 100 ppm (or less) of nitrogen or oxygen.[12,13] In order to detect segregation of these interstitial elements in CN-alloys, CN-80 was fractured in an ultra-high vacuum and analyzed by Auger electron spectroscopy (AES). Limited analyses gave no indication of nitrogen or oxygen segregated to grain-boundary facets or cleavage planes in this alloy.

FRACTURE TOUGHNESS

The fracture toughness of CN-87 (Cr-8Nb-1.5Al-5X1-4X2-20X4) hot extruded at 1480°C was determined by three-point bend testing of Chevron-notched specimens. The alloy exhibited a fracture toughness of 7.6 MPa√m at room temperature. The toughness increased substantially with temperature, to 18.3 and 24.4 MPa√m at 800 and 1000°C, respectively. The alloy was so ductile at 1200°C that it could not be fractured by bend testing. The fracture toughness of CN-87 at room temperature is comparable to that of a Cr_2Hf/Cr alloy reported recently by Kumar and Miracle.[12] Figure 5 shows the crack growth modes in CN-87 at room temperature and 800°C. The alloy exhibited a mixed fracture mode at room temperature (Fig. 5a) and a more ductile fracture with Cr-rich patches necking down to a chisel point at 800°C (Fig. 5b).

(a) (b)

Fig. 5. SEM fractographs of CN-87 hot extruded at 1480°C and fractured by bend testing at (a) room temperature and (b) 800°C.

HIGH-TEMPERATURE OXIDATION BEHAVIOR

It has been previously demonstrated[9] that the presence of significant concentrations of element X1 substantially increased the isothermal oxidation rates and spallation susceptibilities of $Cr\text{-}Cr_2Nb$ alloys, while the addition of X2 completely offset these deleterious effects. The presence of this latter element resulted in the best overall oxidation behavior of all $Cr\text{-}Cr_2Nb$ compositions.[9] The effects of X2 were manifested as relatively low weight gains, substantially reduced scale cracking and spallation, and elimination of the dependence of oxidation behavior on niobium content (that is, on the relative amounts of the Cr-rich and eutectic phases). Its beneficial influence was attributed to improvement in the oxidation resistance of the Cr-rich regions (despite its partitioning to the Cr_2Nb phase),[9] which otherwise showed preferential susceptibility to degradation upon exposure to high-temperature air.[8,14] Recent work has shown that the positive effect of X2 on oxidation resistance is maintained under the more severe oxidation conditions associated with thermal cycling. This is shown by the cyclic oxidation results in Fig. 6: the alloy containing X2 (CN-87, see Table 1) showed relatively low weight gains and significantly improved spallation resistance (as characterized by the weight of spalled material) when compared to a Cr-Cr_2Nb composition containing X1 (CN-80).

Element X2 continued to impart a beneficial effect on the rate of isothermal weight gain and spallation resistance up to 1100°C, as shown by comparison of the curves for uncoated CN-80 and -87 in Fig. 7a and b, respectively. However, the oxidation rate at this temperature was still relatively high (as it is for all chromia-formers). Therefore, it was deemed necessary to examine the possibility of using coatings to reduce the oxidization at higher temperatures. To this end, some preliminary experiments were conducted by depositing a germania-doped silicide coating on CN-80 and CN-87 by pack cementation at The Ohio State University.[15] The details of the coating process for these alloys are described elsewhere.[16] In isothermal microbalance exposures in dry air, specimens coated in this manner exhibited very low weight gains at 950 and 1100°C (Fig. 7). The oxidation rate was essentially controlled by the

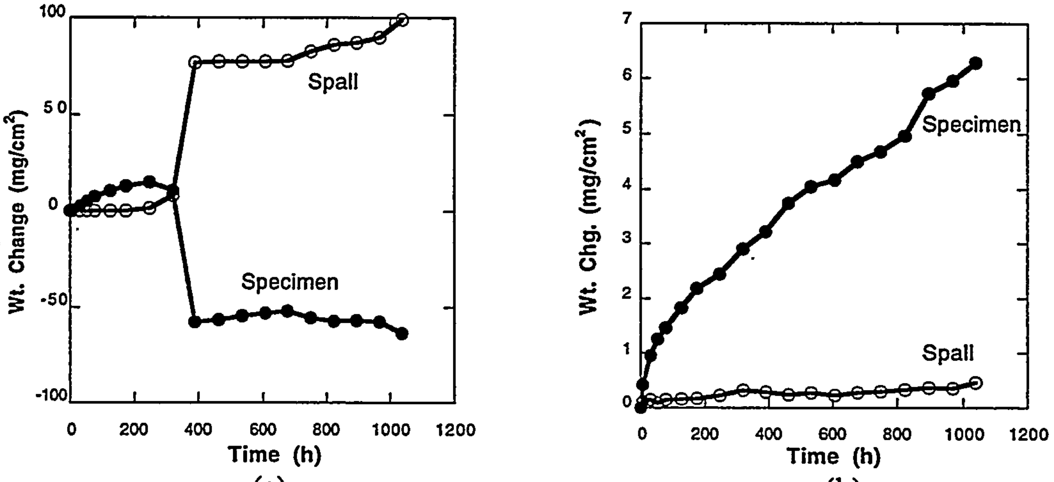

(a) (b)

Fig. 6. Weight change versus time for specimens cyclically oxidized in air at 950°C. Each point represents one thermal cycle. Closed and open symbols represent weight changes of the specimen and spalled material, respectively. (a) CN-80 (b) CN-87

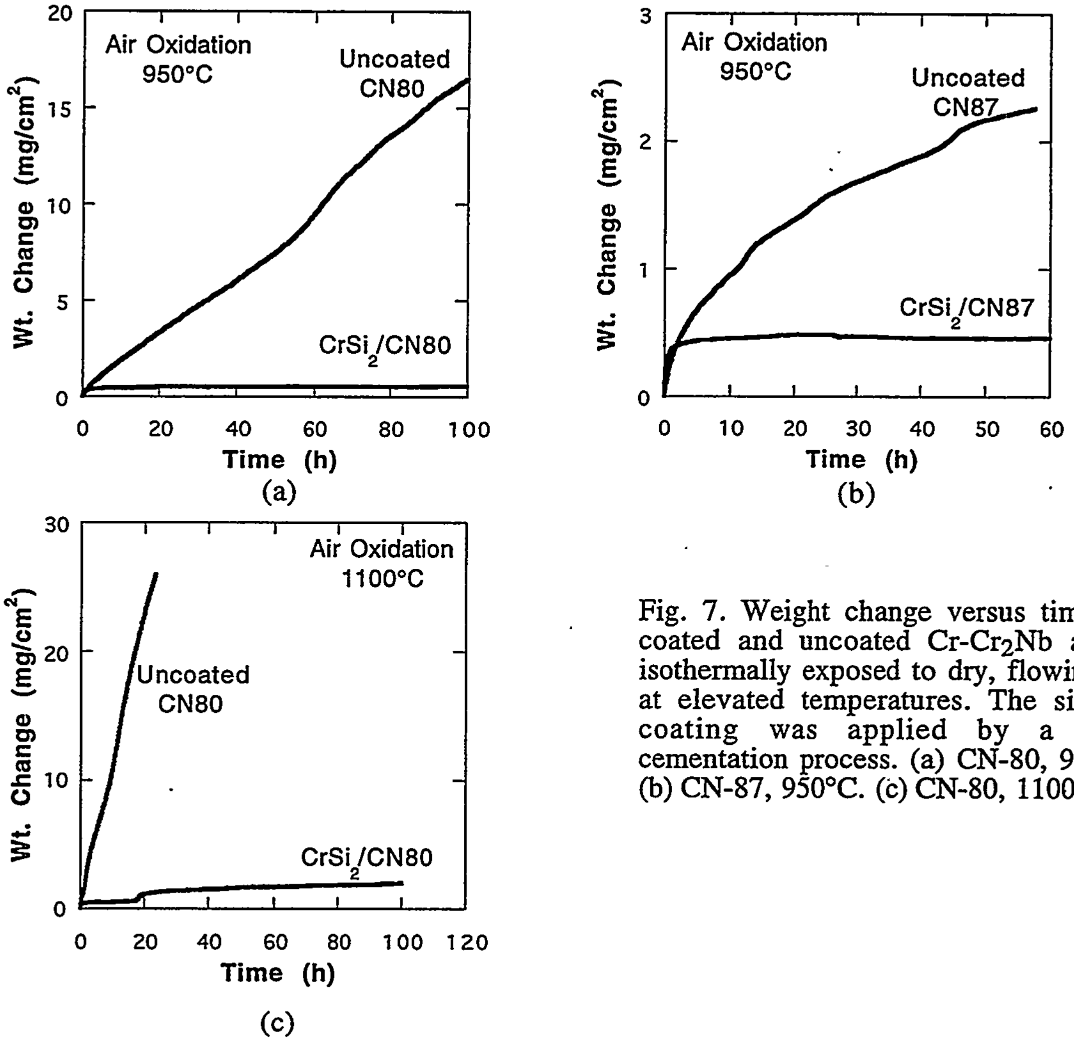

Fig. 7. Weight change versus time for coated and uncoated Cr-Cr_2Nb alloys isothermally exposed to dry, flowing air at elevated temperatures. The silicide coating was applied by a pack cementation process. (a) CN-80, 950°C. (b) CN-87, 950°C. (c) CN-80, 1100°C.

coatings as there was little difference between the 950°C gravimetric results for coated CN-80 and CN-87 (compare Fig 7a with 7b) despite the significant differences in their oxidation rates when uncoated.

While these initial results with coated Cr-Cr_2Nb are quite encouraging, particularly as the coatings have not yet been optimized for these substrates,[16] the influence of thermal stresses produced during cyclic oxidation on the integrity and adherence of these surface layers, and of the oxide scales that formed on them, must be assessed in some detail. In one microbalance experiment, the exposure was twice interrupted by cooling to room temperature with subsequent reheating to the oxidation temperature. The results, shown in Fig. 8, indicated an abrupt weight gain (probably due to cracking of the scale on the coating) after a thermal cycle, but a rapid healing of any cracks such that the same low oxidation rate was quickly reestablished. While final conclusions regarding the utility of this approach for

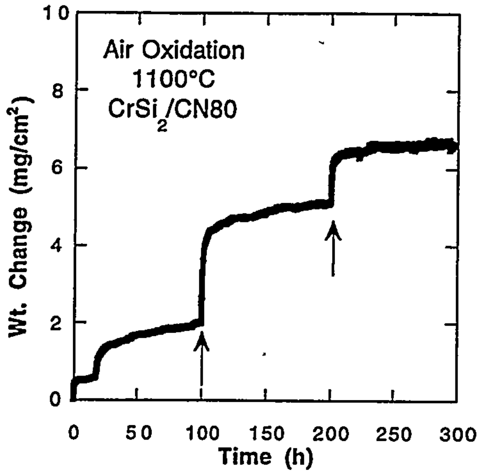

Fig. 8. Weight change versus time for silicide coated CN-80 isothermally oxidized in air at 1100°C. Arrows indicated times at which specimen was cooled to room temperature and then reheated to the exposure temperature.

corrosion protection of these alloys await more rigorous cyclic oxidation testing and coating optimization, the present results indicate that such surface treatments offer excellent promise as effective routes to oxidation resistance for temperatures (such as 1100°C) where the superior strength of Cr-Cr_2Nb alloys can be exploited.

SUMMARY AND CONCLUSIONS

Two-phase Cr-Cr_2Nb alloys (designated as CN alloys) were prepared by arc melting, followed by directional solidification, HIPping, or hot extrusion at 1450 to 1500°C. The secondary processing was used to reduce cast defect structures in CN alloys.

The microstructure of CN alloys containing 6 to 12% Nb depended strongly on alloying addition, heat treatment, and material processing. Hot extrusion at 1480°C was most effective in reducing as-cast defects and refining the cast Cr-Cr_2Nb eutectic structure.

Several beneficial alloying elements have been identified. Element X1 refined the coarse eutectic structure but reduced oxidation resistance. X2 substantially improved both isothermal and cyclic oxidation resistance. X3 strengthened CN alloys at high temperatures. X5 is used to control the morphology of the eutectic structure.

Tensile properties were sensitive to defects in CN alloys. The best results were obtained from hot-extruded CN-80 (Cr-12Nb-1.5Al-6X1) which showed a fracture strength of 548 MPa at room temperature, and an ultimate tensile strength of 388 MPa, with an elongation of 23%, at 1200°C.

The alloy CN-87 fabricated by hot extrusion at 1480°C showed a fracture toughness of 7.6 MPa$\sqrt{m}$ at room temperature. The toughness increased substantially with temperature and reached 24.4 MPa$\sqrt{m}$ at 1000°C.

A silicide coating applied by a pack cementation process substantially improved the oxidation resistance of the Cr-Cr_2Nb alloys at 950 and 1100°C. Such surface layers offer the potential to afford corrosion resistance to these alloys at temperatures (such as 1100°C) at which thermally grown oxides on CN compositions are not protective and, thus, may allow the superior strength of Cr-Cr_2Nb alloys to be exploited.

ACKNOWLEDGMENTS

The authors thank C. G. McKamey and S. J. Pawel for their reviews of the manuscript. This research was sponsored by the Fossil Energy Advanced Research and Technology Development (AR&TD) Materials Program, U. S. Department of Energy, under contract DE-AC05-84OR21400 with Martin Marietta Energy Systems, Inc.

REFERENCES

1. F. Laves, p. 124 in Theory of Alloy Phases, American Society for Metals, Metals Park, OH, 1956, .
2. D. J. Thoma and J. H. Perepezko, Mat. Sci. and Eng. **A156**, 97-108 (1992).
3. H. J. Goldschmidt and J. A. Brand, J. Less-Common Met. **3**, 44 (1961).
4. T. B. Massalski, J. L. Murray, L. H. Bennett, and H. Baker (eds.), Binary Alloy Phase Diagram, American Society for Metals, Metals Park, OH, 1986.
5. A. I. Taub and R. L. Fleischer, Science **243**, 616 (1989).
6. C. T. Liu, pp. 375-383 in *Proc. 6th Annual Conf. Fossil Energy Materials*, N. C. Cole and R. R. Judkins (comp.), U. S. Department of Energy, July 1992.
7. C. T. Liu, J. A. Horton, and C. A. Carmichael, pp. 297-307, in *Proc. 7th Annual Conf. on Fossil Energy Materials*, N. C. Cole and R. R. Judkins (comp.), U. S. Department of Energy, July 1993.
8. P. F. Tortorelli, L. J. Carsen, and J. H. DeVan, pp. 309-318 in *Proc. 7th Annual Conf. on Fossil Energy Materials*, N. C. Cole and R. R. Judkins (comp.), U. S. Department of Energy, July 1993.
9. P. F. Tortorelli and J. H. DeVan, pp. 391-400 in *Proc. 8th Annual Conf. on Fossil Energy Materials*, N. C. Cole and R. R. Judkins (comp.), U. S. Department of Energy, August 1994.
10. C. T. Liu, J. A. Horton, and C. A. Carmichael, pp. 377-390 in *Proc. 8th Annual Conf. on Fossil Energy Materials*, N. C. Cole and R. R. Judkins (comp.), U. S. Department of Energy, August 1994..
11. M. Takeyama and C. T. Liu, Mat. Sci. and Eng. **A132**, 61 (1991).
12. K. S. Kumar and D. B. Miracle, Intermetallics **2**, 257-274 (1994).
13. H. L. Wain, F. Henderson, S.T.M. Jonstone, J. Inst. Met. **83**, 1954-55 (1993).
14. P. F. Tortorelli and J. H. DeVan, "The Nature of Scales Grown on Binary Cr-Nb Alloys," pp. 229-236 in *Proc. Symp. on Oxide Films on Metals and Alloys*, B. R. MacDougall, R. S. Alwitt, and T. A. Ramanarayanan (eds.), Proceedings Vol. 92-22, The Electrochemical Society, 1992.
15. M. A. Harper and R. A. Rapp, pp. 379-86 in Heat Resistant Materials, K. Natesan and D. J. Tillack, (eds.), ASM International, Materials Park, OH, 1991.
16. Y-R. He and R. A. Rapp, "Pack Cementation Cr-Al Coating of Steels and Ge-Doped Silicide Coating of Cr-Nb Alloy," these proceedings.

INVESTIGATION OF AUSTENITIC ALLOYS FOR ADVANCED HEAT RECOVERY AND HOT GAS CLEANUP SYSTEMS

R. W. Swindeman and W. Ren

Oak Ridge National Laboratory
P. O. Box 2008
Oak Ridge, TN 37831-6155

ABSTRACT

Alloys for design and construction of structural components needed to contain process streams and provide internal structures in advanced heat recovery and hot gas cleanup systems were examined. Emphasis was placed on high-strength, corrosion-resistant alloys for service at temperatures above 1000°F (540°C). Data were collected that related to fabrication, joining, corrosion protection, and failure criteria. Alloys systems include modified type 310 and 20Cr-25Ni-Nb steels and sulfidation-resistance alloys HR120 and HR160. Types of testing include creep, stress-rupture, creep crack growth, fatigue, and post-exposure short-time tensile. Because of the interest in relatively inexpensive alloys for high temperature service, a modified type 310 stainless steel was developed with a target strength of twice that for standard type 310 stainless steel.*

INTRODUCTION

The objective of the research on austenitic alloys is to provide databases and design criteria that will assist contractors in selecting optimum alloys for construction of components needed to contain process streams in advanced heat recovery and hot gas cleanup systems. Typical components include: steam line piping and superheater tubing for low emission boilers (600 to 700°C), heat exchanger tubing for topping cycle systems (650 to 800°C), foil materials for recuperators on advanced turbine systems (700 to 750°C), heat exchanger tubing for pulsed combustors (650 to 950°C), and tubesheets, plenums, and liners for hot gas cleanup systems (850 to 1000°C). The near term objective is to gather data that will permit the consideration of a modified

---

* Research sponsored by the U.S. Department of Energy, Office of Fossil Energy, Advanced Research and Technology Development Materials Program {DOE/FE AA 15 10 10 0, Work Breakdown Structure element ORNL-2(B)] under contract DE-AC05-84OR21400 with Martin Marietta Energy Systems, Inc.

310 stainless steel and a modified 20Cr-25Ni-Nb stainless steel for applications to 925°C in oxidizing environments or to 870°C slightly sulfidizing environments. Planned future work includes the collection of data that will permit the consideration of aluminide clad stainless steels for applications to 1000°C in sulfidizing environments.

BACKGROUND

In the United States, new power generation needs are being met by the use of co-generation and the installation of medium-size gas turbines. Research in the fossil power industry is largely focused on condition assessment and the repair of aging components. Research related to inspection, damage assessment, and repair is actively supported by fossil power and petrochemical industries. In both industries, replacement of components with "new" and "advanced" materials is sometimes required, and research on the performance of the advanced materials for such components is in progress. Development of advanced materials for the fossil power industry is largely performed in Japan under sponsorship of the Electric Power Research Institute (1). Alloys such as tungsten-vanadium-modified 2 1/4 Cr, 9Cr, and 12Cr steels have reached ASME Code status. These steels are candidates for the construction of piping, headers, and tubing in the low emission boiler (LEB) project (2). More research is needed before the complex metallurgical constitution of these alloys is fully understood. Austenitic stainless steels for service to higher temperatures in the fossil power industry include niobium-modified 310 stainless steel (3) and titanium-zirconium-modified 20Cr-25Ni-Nb stainless steel (4). Both of these alloys are intended for superheater tubing, and service temperatures are limited to approximately 730°C. Both steels are candidates for heat exchanger tubing in the LEB and the advanced topping cycle. For higher temperature service in the petrochemical industry, a commercial modified alloy 800 has been developed (5), and, for sulfidation resistance, a commercial cobalt-bearing alloy has been produced (6). Both alloys are "new" and much has to be learned about their high temperature performance. Three commercial stainless steels that have been used in the construction of components in advanced fossil energy systems include type 310S stainless steel, a silicon-aluminum modified steel, and a rare earth modified steel. Compositions are listed in Table 1. A careful review of the performance and costs of the materials indicated that there was a need for an additional material. A modified 310 stainless steel having strength equivalent to alloy 800H would have applications above 800°C (7).

Table 1. Typical Compositions of High Temperature Austenitic Alloys (wt%)

ELEMENT	310HCbN	NF-709	HR-120	HR-160	RA85H	253MA
Fe	Balance	Balance	36	4	Balance	Balance
Ni	20	25	37	Balance	14.5	11
Cr	25	20	25	28	18.5	21
Co				30		
C	0.05	0.07	0.05	0.05	0.2	0.08
Si	0.5	0.5	0.6	2.8	3.5	1.7
Mn	1.6	1	0.7	0.5	0.8	0.6
Nb	0.4	0.25	0.7			
Mo		1.5				
N	0.25	0.18	0.2			0.17
Al			0.1		1.0	
Ti		0.06	0.1			
B		0.004	0.004			
Rare earth						0.04

Notes: NF-709 is a trademark of Nippon Steel Corporation, HR-160 and HR-120 are registered trademarks of Haynes Alloys, International, RA85H is a registered trademark of Rolled Alloys, Inc., and 253MA is a registered trademark of AVESTA AB.

EXPERIMENTAL WORK ON MODIFIED 310 STAINLESS STEEL

Commercial alloys were obtained from alloy suppliers, and small heats of experimental alloys were purchased from various sources. Products were fabricated into convenient forms (plates and sheets) for weldability studies, mechanical testing, and corrosion testing. Short-time tensile and stress-rupture testing was used to establish optimum solution treating conditions, and longer creep and stress-rupture testing was performed in the temperature range of interest for the alloys.

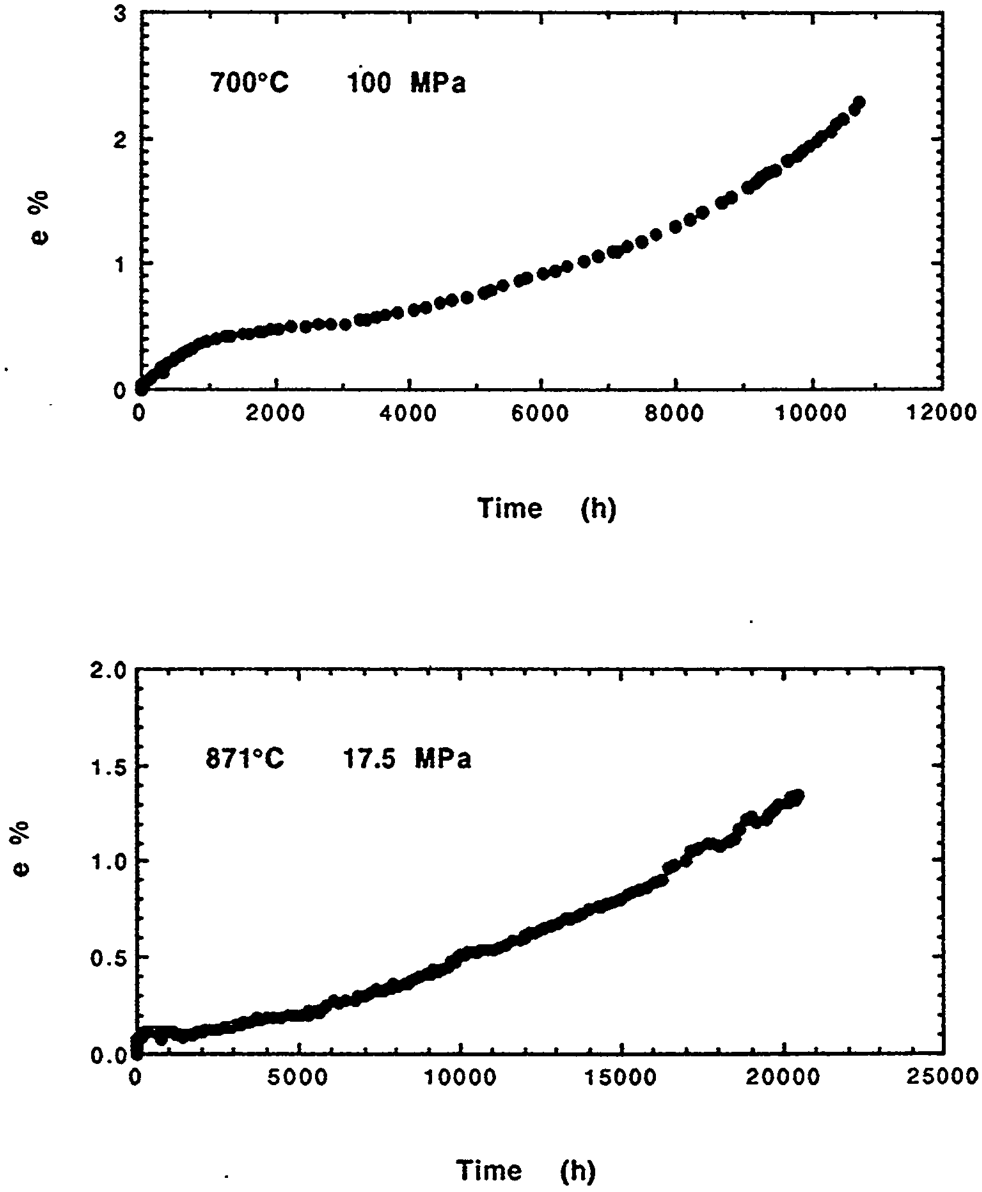

Fig. 1. The 310TaN stainless steel exhibits very little primary creep at all temperatures.

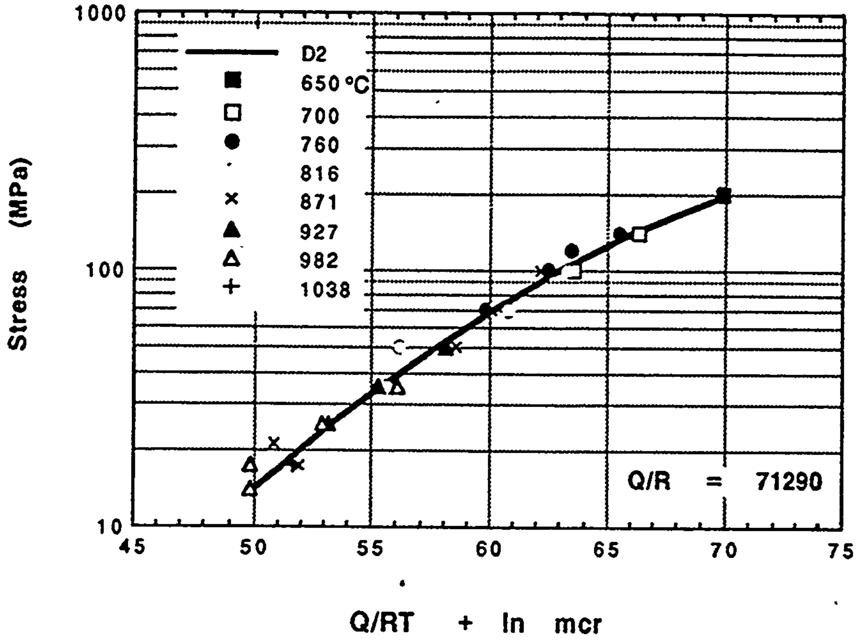

Fig. 2. Parametric analysis of MCR data produced an activation energy near 144 Kcal and a stress exponent near 5.

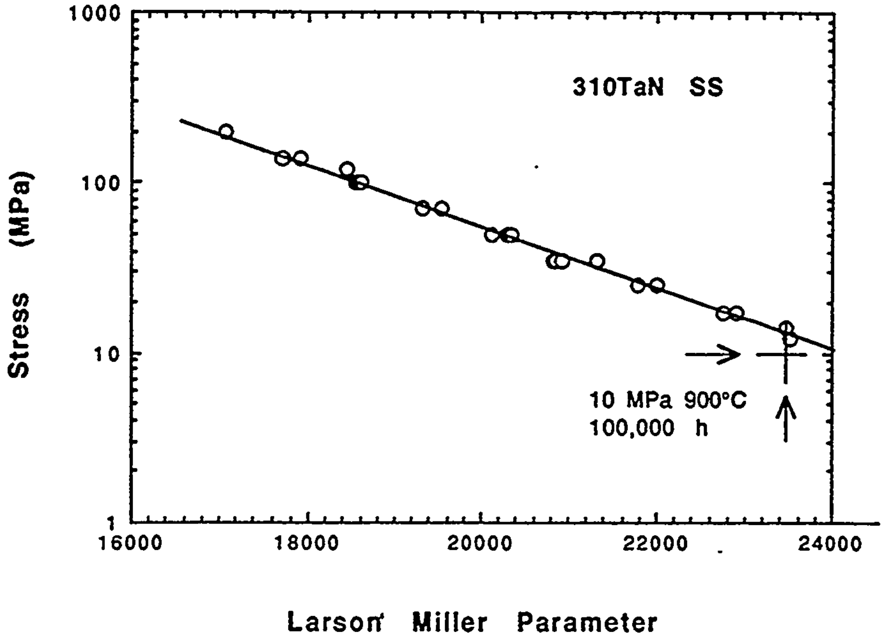

Fig. 3. Parametric analysis of rupture data to 10,000 h suggests that the target strength can be achieved.

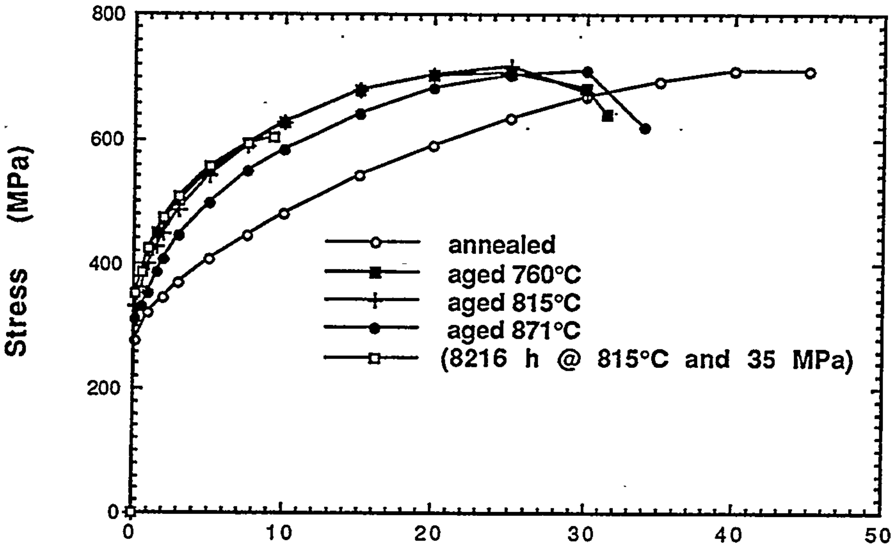

Fig. 4. Aging for 1000 hours produces a reduction of ductility in 310TaN stainless steel.

For modified 310 stainless steel it was found that an anneal at 1200° C produced the best creep-rupture strength for temperatures above 800° C. Creep curves to time beyond 10,000 hours indicated relatively stable behavior, as shown the creep curves plotted in Fig. 1. The minimum creep rates determined from tests in the temperature range of 650 to 1038° C were correlated on the basis of a constant activation energy near 144 kcal/mole. The trend is shown in Fig. 2. Larson-miller parametric analysis of the stress-rupture data for the modified 310 stainless steel indicated that a single parametric constant near 15 correlated rupture data over a broad range of temperatures and times, as shown in Fig. 3. Analysis further indicated that the target strength of 10 MPa for 100,000 h at 900° C could be achieved. Tensile and bend tests were performed on aged specimens. Room temperature tensile stress versus strain curves for aged specimens were compared to unaged material in Fig. 4. It was observed that 1000 h of aging reduced the ductility of modified 310 stainless steel by 30 per cent.

DESIGN CRITERIA FOR VERY HIGH TEMPERATURES

Components in several advanced fossil energy systems are expected to experience very high temperatures, and the potential for creep damage, fatigue, thermal-fatigue, and creep-fatigue crack growth are significant. Issues that are of concern include the proper selection of design margins on life. To some extent, design engineers rely on construction codes such as those developed by the

American Petroleum Institute or the American Society of Mechanical Engineers. However, several of the candidate materials for components are not code-approved materials, and, even for the code-approved materials, data for design at very high temperatures are often lacking. For these reasons, exploratory research on creep, creep-fatigue, fatigue, and crack growth of several candidate alloys has been in progress (8,9).

Early work involved studies of alloy 333 and 556, which were candidates for used in pressurized fluidized bed (PFBC) hot gas cleanup systems. More recently alloy 160 has been investigated. Techniques for creep- and fatigue-crack growth measurements were developed for temperatures to 950°C, and experiments were performed on alloy 160. Tensile and creep tests were included on base metal and weld metal.

PUBLICATIONS

1. M. Ohgami, et al., "Mechanical Properties of 9Cr-0.5Mo-1.8W Steel Tubes Exposed in a Fossil Power Plant, paper presented at the International Symposium on Improved Technology for Fossil Power Plants-New & Retrofit Applications, March 1-3, 1993, Washington, D.C.

2. D. Sopocy, et al., "Using the State of the Art Power Plant SOAPP Workstation for Planning and Conceptual Design, paper presented at the International Symposium on Improved Technology for Fossil Power Plants-New & Retrofit Applications, March 1-3, 1993, Washington, D.C.

3. K. Yoshikawa, et al., Development of New Boiler Tubes with High Elevated Temperature Strength and Corrosion Resistance,^{2} paper 5-167, First International Conference on Improved Coal Fired Power Plants, EPRI publication CS-5581-SR, Electric Power Research Institute, Palo Alto, California, 1988.

4. T. Takahashi, el al., Development of a High Strength 25Ni-20Cr Steel for Tubes in Ultra Supercritical Power Boilers,^{2} paper 41-1 in Second International Conference on Improved Coal Fired Power Plants, EPRI publication GS-6422, Electric Power Research Institute, Palo Alto, California, 1989.

5. S. C. Ernst and G. Y. Lai, "A New High Strength Fe-Ni-Cr-Nb-N Alloy for Elevated Temperature Applications,^{2} pp. 115-121 in Heat Resistant Materials, ASM International, Materials Park, Ohio, 1991.

6. C. M. Anthony, S. K. Srivastava, and G. Y. Lai, pp. 667-73 in Heat Resistant Materials, ASM International, Materials Park, Ohio, 1991.

7. R. W. Swindeman, The Potential of Modified Type 310 Stainless Steel for Advanced Fossil Energy Applications, ORNL-TM-12057, Oak Ridge National Laboratory, Oak Ridge, TN March, 1992.

8. R. W. Swindeman and D. L. Marriott, "Criteria for Design with Structural Materials in Combined-Cycle Applications above 815° C,² J. Engineering for Gas Turbines and Power, **116**, 352-59 April, 1994 .

9. W. Ren, et al., Creep and Creep Crack Propagation Behavior of Haynes HR160 Superalloy, Final Report for SURA/ORAU/ORNL 1994 Summer Cooperative Program, October , 1994.

FIRESIDE CORROSION TESTING OF CANDIDATE SUPERHEATER TUBE ALLOYS, COATINGS, AND CLADDINGS - PHASE II

J. L. Blough
M. T. Krawchuk
S. F. Van Weele

Foster Wheeler Development Corporation
12 Peach Tree Hill Road
Livingston, NJ 07039

ABSTRACT

A number of developmental and commercial tubing alloys and claddings have previously been exposed in Phase I to laboratory fireside corrosion testing simulating a superheater or reheater in a coal-fired boiler. This program is exposing samples of TP 347, RA-85H, HR-3C, 253MA, Fe_3Al + 5Cr, 310 modified, NF-709, 690 clad, and 671 clad, which showed good corrosion resistance from Phase I, to the actual operating conditions of a 250-MW, coal-fired boiler. The samples were installed on air-cooled, retractable corrosion probes, installed in the reheater cavity, and are being controlled to the operating metal temperatures of an existing and advanced-cycle coal-fired boiler. The exposure will continue for 4000, 12,000, and 16,000 hours of operation. After the three exposure times, the samples will be metallurgically examined to determine the wastage rates and mode of attack.

The probes were commissioned November 16, 1994. The temperatures are being recorded every 15 minutes, and the weighted average temperature calculated for each sample. Each of the alloys is being exposed to a temperature in each of two temperature bands—1150 to 1260°F and 1260 to 1325°F. After 2000 hours of exposure, one of the corrosion probes was cleaned and the wall thicknesses were ultrasonically measured. The alloy performance from the field probes will be discussed.

INTRODUCTION

High-temperature fireside metal wastage in conventional coal-fired steam generators can be caused by gas-phase oxidation or liquid-phase coal-ash corrosion. Gas-phase oxidation is usually not a problem if tube and support materials are selected for their oxidation resistance at operating temperatures and for spalling, flaking, or other reactions to their environment. Coal-ash corrosion, on the other hand, usually results in accelerated attack and rapid metal wastage—even of stainless steels. The cause of this type of corrosion is generally accepted as the presence of liquid sulfates on the surface of the metal beneath an overlying ash deposit[1-4].

While substantial progress has been achieved through laboratory testing, actual utility service exposures are evidently necessary to verify any conclusions drawn from laboratory testing. A number of important environmental parameters cannot be fully simulated in the laboratory[5]:

- The actual composition of the deposits formed on the tubes is more complex than the composition of the simulated ash.
- The SO_3, formed by heterogeneous reaction on cooled surfaces, is variable.
- Very large temperature gradients occur within the ash deposits.
- The ash and fuel gas move past tubes at high velocity; the rate varies with design.
- The composition of the corrosive deposits changes with time.
- Metal and flue gas temperatures fluctuate.
- Fly-ash erosion removes the protective oxides, exposing a clean surface to fresh ash.

Foster Wheeler Development Corporation (FWDC) has performed a number of literature reviews and recent updates discussing the variables affecting the corrosion mechanism[6-8]. Additionally, Foster Wheeler is conducting two sizable research projects—one a laboratory and in situ field testing at three utilities of commercially available alloys[5,9-14] and this program (ORNL-FW2), combining laboratory and field testing to more completely cover the controlling variables for a longer duration[10].

PHASE I RESULTS

In Phase I of this ORNL program, "Fireside Corrosion Testing of Candidate Superheater Tube Alloys, Coatings, and Claddings," 20 commercial and developmental alloys were evaluated[10]. The coupons of the metals were exposed to synthetic coal ash and synthetic flue gases at 650 and 700°C (1202 and 1292°F) for up to 800 hours.

Chromium content was found to be the largest factor in determining the resistance of an alloy to liquid coal-ash corrosion. For stainless steels and nickel alloys, additions of chromium up to 25 percent provide increased resistance to coal-ash attack; however, above the 25-percent chromium level, there appears to be minimal benefit from more chromium, possibly because of the higher nickel content of those alloys. Silicon and aluminum were also beneficial, but to a lesser extent. The iron aluminide intermetallics also show a chromium dependence. Aluminides containing 5-percent chromium performed markedly better overall than those containing 2-percent chromium. The more resistant alloys show lower corrosion rates at longer exposure times, indicating the formation of a passive layer; the less-resistant alloys exhibit increasing corrosion rates at longer exposures. Lower-chromium alloys generally suffered greater wastage rates at the higher testing temperature [700°C (1292°F)], while higher-chromium alloys suffered the same amount of wastage at 650 (1202) as at 700°C (1292°F).

Both the alkali content in the ash and SO_2 concentration in the flue gas affect the corrosivity of the alkali-iron trisulfates in the ash layer. An increase in either resulted in a more corrosive environment and higher wastage rates.

PHASE II CORROSION PROBE TESTING

In this project, the field tests will comprise corrosion probe testing, coal characterization, and deposit analysis. The coals and their deposits, which are formed on the tube surfaces, will be analyzed to provide fuel characterization, a deposit analysis data bank, and possibly a corrosivity index for predicting corrosivity under various combustion conditions. The equipment and the procedures for this phase have been previously used and perfected at three different utilities for over 3 years of in situ testing at each station.

The utility for test exposures should be burning an aggressive fuel to adequately evaluate the candidate alloys. The coal being burned at Tennessee Valley Authority's (TVA's) Gallatin Station had been previously analyzed, and numerous corrosion indices predicted high corrosivity in addition to the fact that installed T22 and Type 304SS tubing experienced about 7 years of life in the superheaters and reheaters of Units 1 and 2.

Selection of Materials for Corrosion Probes

FWDC laboratory-tested 20 different materials[10]. Because this quantity was impractical from both an economic and a probe-length standpoint, fewer (the nine listed in Table 1) had to be selected for the field tests. These materials provide a range of compositions and cost for both the commercially available and developmental alloys and claddings.

Field Corrosion Probe Design

The corrosion probes were designed to provide realistic exposures of metal samples to both actual boiler environments and also at the higher anticipated metal temperatures of an advanced plant. The parameters are independence from the main boiler, removal without a boiler outage, and a fail-safe design, one that removes the probe from the boiler if there are any malfunctions. With these features, years of testing will not be compromised with a sudden system overheating.

The probes will be exposed for 4000, 12,000, and 16,000 hours. This will be accomplished by utilizing two probe test locations. At one test location, the probe will be exposed for 16,000 hours. At

Table 1. Chemical Composition of Candidate Alloys (%)

Alloy	Cr	Ni	Others
Type 347	17-19	9-13	(Nb + Ta) = 10 × C (min.)
85 H	18	15	Al = 1, Si = 3.9
NF 709	20	25	Mo = 1.5, Mn = 1.0, Si = 0.6
690 Clad	30	58	
671 Clad	48	52	
Fe_3Al + 5% Cr	5	---	Al = 17
HR-3C	25	20	Nb = 0.4
253 MA	21	11	Si = 1.7
Modified 310	25	20	Modified

the other test location, the probe will be removed after 4000 hours and a new probe inserted for the remaining 12,000 hours.

Each probe is a 2.56-m (8.4-ft)-long, 60.20-mm (2.37-in.)-OD tube that extends into the furnace for approximately 2.3 m (7.6 ft). Ring samples [38.1 mm (1.5 in.) wide] of the candidate alloys listed in Table 1 were installed at the end of the probe farthest from the furnace wall. The probe is cooled by air that flows in the annular region between the probe tube ID and the tapered inner tube OD. The tapered inner tube was designed to obtain two bands of temperature on the outer surface of the samples. The alloy samples were duplicated in such a manner as to expose each alloy to a temperature in each of the temperature bands [621 to 677°C (1150 to 1250°F) and 677 to 727°C (1250 to 1340°F)].

Each probe has a retraction mechanism, and three K-type thermocouples in duplicate to monitor the mean tube wall at the beginning and end of each test section group. A 19.95-mm (3/4-in.) O.D. thermowell with sheathed thermocouple was mounted between the corrosion probes to measure flue gas temperature. Each probe has its own cooling-air control valve.

The control system monitors the selected control thermocouple and modulates the airflow to maintain an average surface metal temperature for each temperature band. The probes retract automatically if failure of the cooling-air supply system or any other malfunction (instrument signal, power failure, or computer failure) causes the probe temperature to exceed the set limit of 746°C (1375°F) for 2 minutes. FWDC personnel access the field computer automatically for probe status and temperature data each morning at 6 a.m. or manually through its modem.

The locations in this plant (shown in Figure 1) were chosen because of cavity access and because they best represent the locations for the reheater or superheater outlet on the "Advanced Cycle" unit.

The ideal coal-ash corrosion probe exposure is if only one coal is being burned at the plant. This practice is not common at many utilities; in fact, many are buying coal on the spot market. Gallatin burns a number of eastern high-sulfur coals, mainly Island Creek, Warrior, Dotiri, and Pattiki, which are known to be corrosive and prone to alkali-iron-trisulfate formation. The Borio Index for these coals typically range from 2.0 to 4.1, and the chloride level is 450 to 3000 ppm.

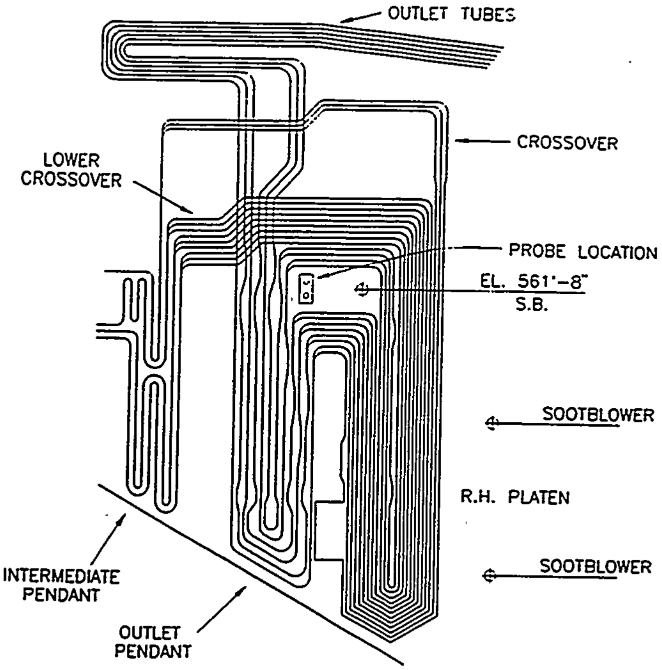

Fig. 1. Side elevation of reheater at TVA Gallatin Unit 2

Post-Exposure Analysis

Quarterly Examinations

During the quarterly inspections, FWDC personnel at the site will manually retract the probes, selectively remove deposits, and make ultrasonic wall thickness measurements on the "A" samples of the probe set.[*] The "B" probe will be left untouched at this time. The quarterly inspections will

---

[*] To aid in describing the operations, "A" (inspected quarterly) and "B" (untouched) have been assigned to the two probes in a set. The operations will be performed on the "A" or "B" probes in each 4000-, 12,000-, and 16,000-hour-exposure set.

provide preliminary nondestructive corrosion data before the three destructive examinations. With these data, corrosion can be tracked, and a total loss of data can be avoided if there is a catastrophic failure. The automatic retraction feature, if cooling air is lost and test specimen temperatures become excessive, minimizes the possibility of such a catastrophic failure.

The laboratory analysis of the removed deposits at FWDC will characterize the composition and determine whether alkali sulfates are present and aid in interpreting the effect of fuel changes on coal-ash corrosion.

Destructive Testing

At 4000, 12,000, and 16,000 hours, probes (A-1," "A-2," and "B" respectively) will be removed and sent to FWDC for metallurgical evaluation, which includes:

- Visual examination and selective photographic documentation
- Selective removal of deposits
- Disassembly of probes
- Cutting of two transverse sections through the center of the ring sample
- Light grit blasting and NaOH cleaning of one transverse ring section of each sample
- Visual examination of the cleaned samples
- Wall thickness measurements at 45-deg points or maximum loss areas on the leading 180-deg side of cleaned transverse ring from each alloy
- Mounting of the uncleaned ring samples to analyze the scale/deposit
- Microscopic measurement of the penetration and calculation of total metal loss
- Selective SEM/EDX examination to analyze corrosion mechanism.

Exposure Results to Date

The 4000- and 16,000-hour corrosion probes continued to be exposed in the reheater cavity of the TVA Gallatin Station Unit 2. The temperature plots for March are shown in Figure 2. The upper curve is the flue gas temperature [average 807°C (1484°F)] measured by a separate thermowall. The lower two bands are the mean wall thermocouples at the beginning and end of each test section in the two probes. The nine alloys listed in Table 1 are contained in each test section. The weighted average temperature is calculated for each test section in each of the two probes and is shown in Table 2.

On March 8, 1995, the probes were pulled for maintenance and ultrasonic inspection of the 4000-hour probe. On each ring the measurements were taken at two cleaned locations of approximately 10:00 and 2:00 with the oncoming flue gas at 12:00. Thickness losses were calculated, and the range of wall loss is given in Table 3. These thickness losses were obtained from an ultrasonic

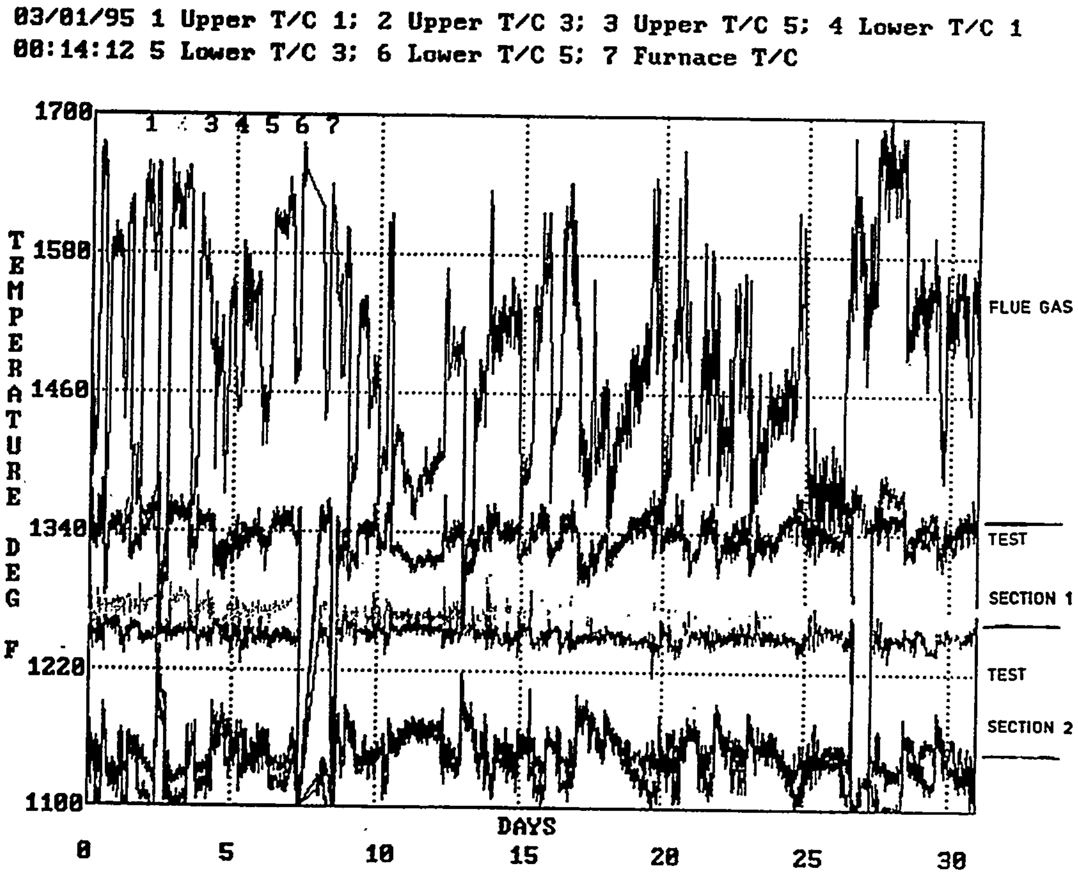

Fig. 2. Temperature profile, March 1995.

Table 2. Average Exposure Temperature

Test Section	4000-Hour Probe [°C (°F)]	16,000-Hour Probe [°C (°F)]
1	726-683 (1339-1261)	723-678 (1334-1252)
2	683-618 (1261-1144)	678-619 (1252-1147)

reading and, therefore, should be taken as only relative values. They do not include any internal penetration measurements and are not as accurate as micrometer and microscopic examination. Figure 3 shows the two probes in the retracted position. The nearby soot blower can be seen to the right of the corrosion probes. The 4000-hour probe was carefully cleaned (as shown in Figure 4) with a wire wheel and/or sanding disk to remove the deposit and scale without removing any metal.

The thickness losses for each alloy are generally higher, as would be expected, in the hotter Section 1 samples vs. the Section 2 sample. There are some exceptions, but these results are only interim ultrasonic measurements.

Table 3. Ultrasonic Measurement Results (mils)

Material	Test Section 1 Thickness Loss	Test Section 2 Thickness Loss
800HT	1-4	
800HT	0-6	0-3
85H	0-4	0-2
347	0-2	0-6
NF709	0	0-5
253MA	4-5	2-6
671	6-14	8-9
690	0	0-5
Fe_3Al	0	0
310	0-2	0-4
800HT	0-5	0
800HT		0

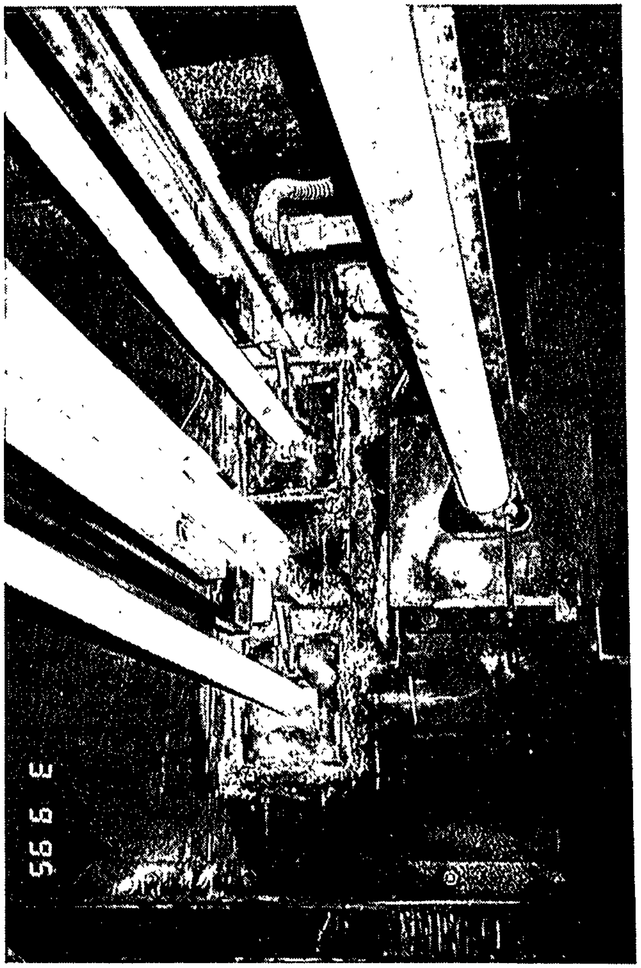

Fig. 3. Corrosion probe in retracted position.

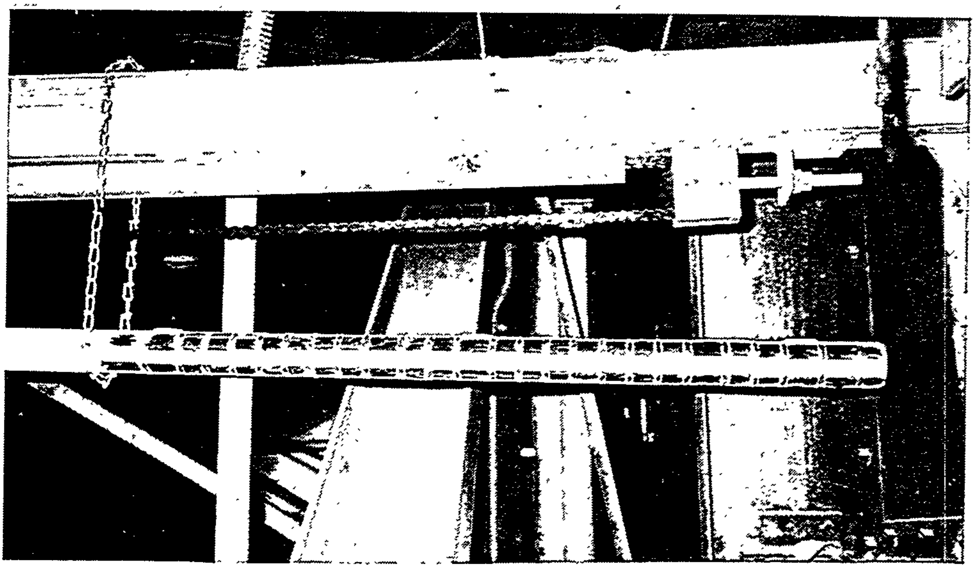

Fig. 4. Cleaned 4000-hour probe.

There was quite a variation in the thickness readings and, therefore, no elemental dependency could be determined. The stability of the readings on the 671 sample was a problem, but there was a consistently higher loss than would have been expected from the previous lab data.

Again, these ultrasonic readings every 2000 hours are a check on the status of the alloys and determine relative losses, not absolute measurements which can only be done when microscopic examination for penetration is performed.

CONCLUSIONS

The air-cooled retractable corrosion probes are working successfully and are providing exposure of each of the nine alloys to two different temperatures. The ultrasonic readings indicate that the exposure at the TVA Gallatin Unit 2 is aggressive.

Future metallographic and corrosion deposit analyses will verify the wastage rates and corrosive attack mechanisms (i.e., coal ash, erosion-assisted oxidation, etc.).

REFERENCES

1. W. Nelson and C. Cain, Jr., "Corrosion of Superheaters and Reheaters of Pulverized-Coal-Fired Boilers," *Transactions of the ASME, Journal of Engineering for Power,* July 1960, pp. 194-204.

2. W. T. Reid, "Formation of Alkali Iron Trisulphates and Other Compounds Causing Corrosion in Boilers and Gas Turbines," Project Review July 1, 1966-June 30, 1968, prepared by Battelle Memorial Institute, Columbus, OH, June 1968.

3. W. T. Reid, *External Corrosion and Deposits: Boilers and Gas Turbines,* American Elsevier Publishing Company, New York, 1974.

4. G. J. Hills, "Corrosion of Metals by Molten Salts," *Proceedings of the Marchwood Conference: Mechanism of Corrosion by Fuel Impurities,* Johnson and Littler, eds., Butterworths, London, 1963.

5. J. L. Blough, G. J. Stanko, M. Krawchuk, W. Wolowodiuk, and W. Bakker, "In Situ Coal Ash Corrosion Testing for 2 Years at Three Utilities," International EPRI Conference on Improved Technology for Fossil Power Plants New and Retrofit Applications, Washington, DC, March 1-3, 1993.

6. I. M. Rehn, "Fireside Corrosion of Superheater and Reheater Tubes," Palo Alto, CA: Electric Power Research Institute, 1980. CS-1653.

7. I. M. Rehn, "Fireside Corrosion of Superheater Alloys for Advanced Cycle Steam Plants," Palo Alto, CA: Electric Power Research Institute, 1987. EPRI 5195.

8. S. Van Weele and J. L. Blough, "Literature Search Update—Fireside Corrosion Testing of Candidate Superheater Tube Alloys, Coatings, and Claddings," Livingston, NJ: Foster Wheeler Development Corporation, September 1990. FWC/FWDC/TR-90-11.

9. W. Wolowodiuk, S. Kihara, and K. Nakagawa, "Laboratory Coal Ash Corrosion Tests," Palo Alto, CA: Electric Power Research Institute, July 1989. GS-6449.

10. S. Van Weele and J. L. Blough, "Fireside Corrosion Testing of Candidate Superheater, Tube Alloys, Coatings, and Claddings," Livingston, NJ: Foster Wheeler Development Corporation, August 1991. ORNL/SUB/89-SA187/02.

11. S. Kihara, K. Nakagawa, A. Ohtomo, H. Aoki, and S. Ando, "Simulating Test Results for Fireside Corrosion of Superheater & Reheater Tubes Operating at Advanced Steam Conditions in Coal-Fired Boilers, *High Temperature Corrosion in Energy Systems,* TMS/AIME, M. F. Rothman, ed., 1984, pp. 361-376.

12. W. Wolowodiuk, et al., "Coal-Ash Corrosion Investigations," *Proceedings of the First International Conference on Improved Coal-Fired Power Plants.* Palo Alto, CA: Electric Power Research Institute, November 1986.

13. J. L. Blough, M. T. Krawchuk, G. J. Stanko, and W. Wolowodiuk, "Superheater Corrosion Field Test Results," Palo Alto, CA: Electric Power Research Institute, November 1993. TR-103438.

14. J. L. Blough and W. T. Bakker, "Measurement of Superheater Corrosion Caused by Molten Alkali Sulfates," First International Conference on Heat-Resistant Materials, to be presented at the ASM International, Lake Geneva, WI, September 22-26, 1991.

15. T. Hammond, W. Wolowodiuk, J. L. Blough, J. Brooks, "Replacement of Reheater at TVA's Gallatin Station Unit 2," presented at the Third International Conference on Improved Coal-Fired Power Plants (ICPP), San Francisco, April 1991.

16. R. W. Borio and R. P. Hensel, "Coal-Ash Composition as Related to High-Temperature Fireside Corrosion and Sulfur-Oxides Emission Control," *Transactions of the ASME, Journal of Engineering for Power,* Vol. 94, 1972, pp. 142-148.

A NOVEL CARBON FIBER BASED POROUS CARBON MONOLITH

T. D. Burchell, J. W. Klett, and C. E. Weaver

Oak Ridge National Laboratory
P.O. Box 2008
Oak Ridge, Tennessee 37831-6088

ABSTRACT

A novel porous carbon material based on carbon fibers has been developed. The material, when activated, develops a significant micro- or mesopore volume dependent upon the carbon fiber type utilized (isotropic pitch or polyacrylonitrile). The materials will find applications in the field of fluid separations or aa a catalyst support. Here, the manufacture and characterization of our porous carbon monoliths are described.

INTRODUCTION

A novel adsorbent carbon composite material has been developed[1,2] comprising carbon fibers and a binder. The material, called carbon fiber composite molecular sieve (CFCMS), was developed through a joint research program between Oak Ridge National Laboratory (ORNL) and the University of Kentucky, Center for Applied Energy Research (UKCAER).

The materials are manufactured from milled carbon fibers and powdered phenolic resin, which are slurried in water and vacuum molded. The molding process allows the manufacture of slabs, tubes or more complex geometries with contoured surfaces. The "green" (as molded) artifact is heated at 130°C to cure the phenolic resin and then carbonized at 650°C. The resultant monoliths have bulk densities in the range 0.2 - 0.4 g/cm^3 and crush strength of 1 - 2 MPa. Two carbon fiber types have been utilized in our work to date. First, petroleum-pitch derived isotropic carbon fibers have been fabricated into monoliths and activated in steam or CO_2 at 850°C. The material develops significant microporosity, with mean pore sizes in the range 0.5 - 1.0 nm, and micropore volumes in the range 0.2 - 0.5 cm^3/g. Second, monoliths have been manufactured from polyacrylonitrile (PAN) derived carbon fibers. These materials develop significant mesoporosity in the size range 2-50 nm and mesopore volumes typically exceeding 0.5 cm^3/g, making them potential catalyst support materials. In both cases the composites are strong and porous, allowing fluids to easily flow through the material.

The isotropic pitch derived carbon fiber porous carbon monolith, when activated, provides a high micropore surface area (> 1900 m^2/g) capable of rapid adsorption and desorption. The activated fiber micropore distribution is very narrow, with mean micropore sizes < 1 nm, allowing molecular sieving on the basis of molecular size and shape. A potentially large application for our carbon-fiber based porous monoliths is gas separation using the Pressure Swing Adsorption (PSA) process.

Separation by adsorption is based on the selective accumulation of one or more components of a gas mixture on the surface of a microporous solid. When a gaseous mixture is exposed to an absorbent for sufficient time, an equilibrium is established between the adsorbed phase and the gas phase. The gas phase becomes richer in the less selectively adsorbed component. The attractive forces responsible for adsorption are of the Van der Waals type. Desorption can be achieved either by increasing the temperature of the system or by reducing the adsorbate pressure. The desorption step also regenerates the adsorbent surface for reuse during the subsequent adsorption step. Thus, the adsorptive separation process consists of a cyclic sequence of adsorption and desorption steps. When desorption is achieved by decreasing the pressure, the process is called pressure swing adsorption. One of the components of a gas mixture is selectively adsorbed at higher partial pressure and desorbed subsequently by lowering the partial pressure. The change in partial pressure of the component gas can be caused either by decreasing the total pressure, changing the composition of the gaseous mixture, or by a combination of both.

Here we report the synthesis and characterization of CFCMS material, particularly with respect to micropore and mesopore structure. Moreover, the results of CO_2 uptake studies on microporous monoliths are reported.

EXPERIMENTAL

Nitrogen adsorption isotherms were measured at 77 K using our Autosorb-1 instrument. Micropore size analysis used a variety of methods, including the Brunauer, Emmett and Teller[3] (BET) method for surface area and the Dubinin-Redushkevich (DR) method for micropore volume and micropore size. Additional micropore size estimates were obtained using the Horvath-Kawazoe (HK) and Dubinin-Astakhov (DA) methods. Mesopore (2-50 nm) and macropore (>50 nm) size, area, and volume data were obtained using a Micromeritics Autopore II mercury intrusion apparatus. Intrusion measurements were performed over the pressure range vacuum (~10μm Hg) to 90,000 psia. Equilibration times of 10 and 60 seconds were used for the low and high pressure measurements, respectively. CFCMS materials were subjected to microstructural examination using an ISI SS40 scanning electron microscope (SEM). CO_2 uptake was measured using a Mettler thermal microbalance. Specimens were thoroughly outgassed by heating them to 300°C under vacuum on the microbalance. The specimens were then cooled under vacuum to room temperature and the balance back-filled with CO_2. The weight loss and gain was measured when the specimen temperature was swung from 30 to 110°C and back to 30°C.

RESULTS AND DISCUSSION

CFCMS Synthesis

The CFCMS material was fabricated at ORNL using a process initially developed by the DOE for the production of thermal insulators for NASA space missions[4]. Carbon fibers derived from either isotropic petroleum pitch, or PAN, were mixed in a water slurry with powdered phenolic resin. The slurry was transferred to a molding tank and the water drawn through a porous mold under vacuum. The resulting green artifact was dried, cured in air at 60°C, and stripped from the mold. The composite was cured at ~150°C in air prior to carbonization at 650°C under an inert gas. The CFCMS synthesis route is illustrated in Fig. 1. A schematic diagram of the molding arrangement is shown in Fig. 2. The fabrication process allows the manufacture of slab or tubular forms. Moreover, we believe that it will be possible to mold contoured plates, and tubes, to near net shape via this synthesis route. Once carbonized, CFCMS is readily machined to more complex geometries. Typical carbonized bulk densities of our CFCMS materials are 0.3-0.4 g/cm^3.

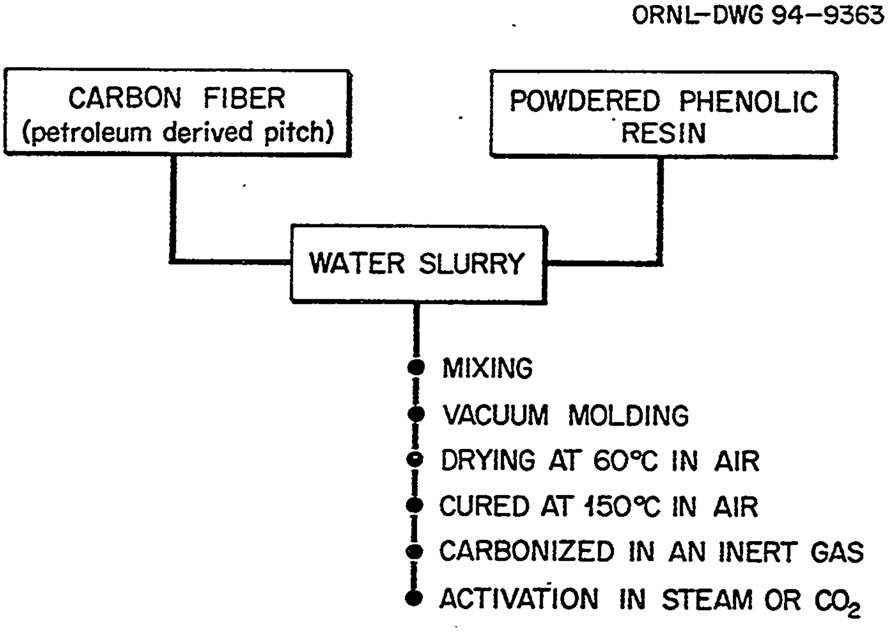

Fig. 1. CFCMS synthesis route.

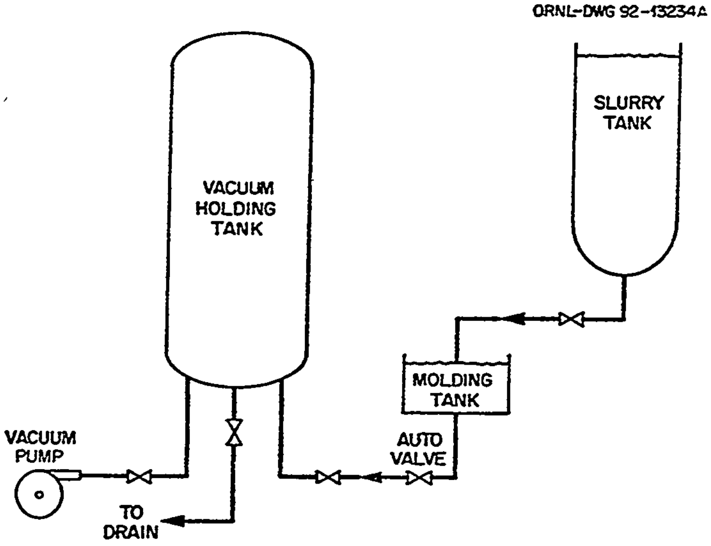

Fig. 2. Schematic illustration of the CFCMS molding apparatus.

Characterization

Microporous Carbon Fiber Monoliths

Figure 3 (×200 magnification) shows the structure of our CFCMS material manufactured from isotropic pitch derived carbon fibers. The chopped fibers are bonded at their contact points. The carbon fibers are approximately 10-20 μm diameter, whereas the macro-voids between the fibers are typically >30 μm in size. The resultant open structure allows free flow of fluids through the material and ready access to the carbon fiber surface. Previously, we reported the carbon fiber length distribution[1]. The distribution mode is ~400 μm and the fiber lengths are widely distributed and range from 100 to 1000 μm. Mercury porosimetry data for the CFCMS material in the unactivated condition are shown in Fig. 4, and indicate the macropore size range to be approximately 10-100 μm. The macropores are the voids between the fibers, and mercury porosimetry data for macropore sizes are in agreement with visual observations made from SEM images (Fig. 3).

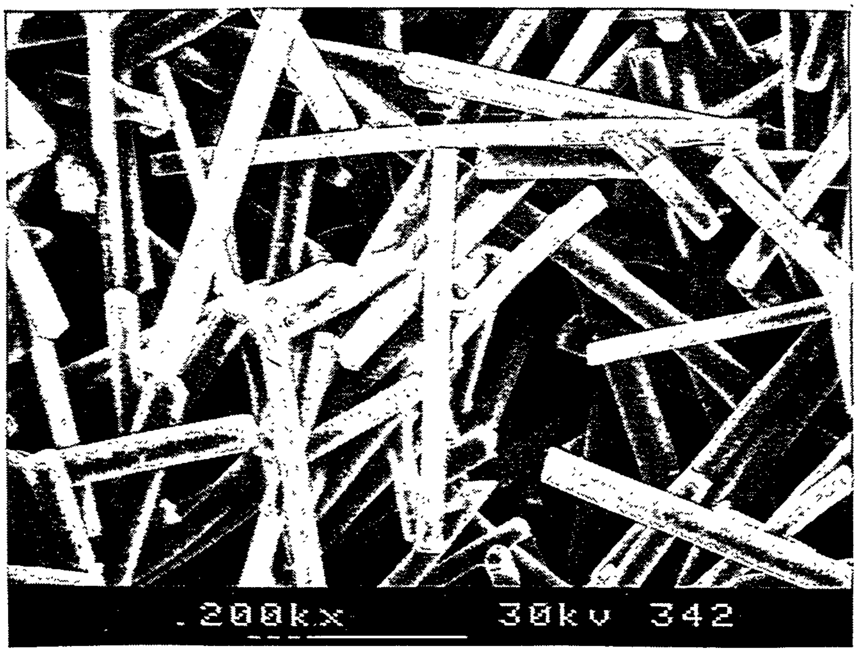

Fig. 3. SEM micrograph of carbon fiber composite molecular sieve (magnification x 200).

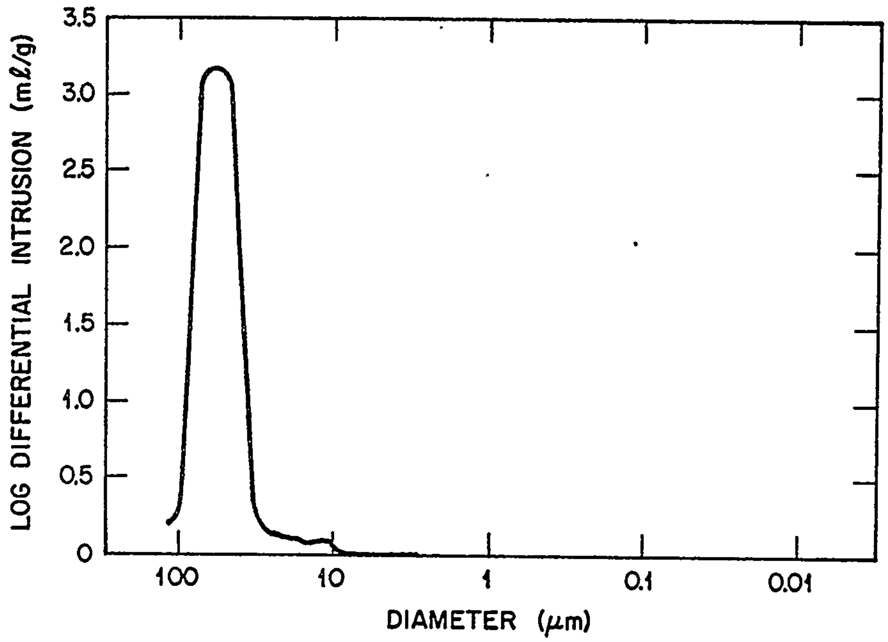

Fig. 4. CFCMS macropore size distribution for a pitch derived carbon fiber monolith obtained from mercury intrusion data.

A series of CFCMS materials were prepared at ORNL and activated at UKCAER. Details of the activation conditions are given in Table 1 along with the results of our analysis of the microporosity.

Table 1. Activation conditions and micropore characterization data.

Spec. Ident.	Activation Conditions				Micropore Analysis Data				
	Temp (°C)	Time (mins)	Agent	Burn -off (%)	BET Area (m^2/g)	Micropore Width (nm)			DR Pore Vol (cm^3/g)
						HK	DA	DR	
160	800	30	H_2O	7	394	0.48	1.3	0.58	0.20
161A	950	10	CO_2	6	292	0.48	1.8	1.21	0.13
161B	950	10	CO_2	6	281	0.47	1.9	1.34	0.10
166	800	180	H_2O	17	762	0.48	1.48	0.75	0.39
167	800	360	H_2O	28	891	0.49	1.5	0.76	0.49
170	950	180	CO_2	32	1132 1038	0.47	1.6	0.78 0.76	0.48
46	850	90	H_2O	28	1461	0.62	1.3	0.67	0.73

The BET surface areas reported in Table 1 ranged from 281 to 1461 m^2/g, and the mean micropore size (DR method) varied from 0.58-1.34 nm. Moreover, the micropore volumes (DR method) varied from 0.1 - 0.73 cm^3/g. The large surface area, combined with a large volume of micropores, suggests these materials might have a strong affinity for the adsorption of light gases. Therefore, CO_2 adsorption studies were performed, and our data are reported in Table 2.

Table 2. CO_2 uptake data and micropore data

Spec. Ident.	CO_2 Uptake data				Micropore Analysis Data				
	Sample Mass (mg)	Wt% CO_2 Uptake	Vol CO_2 Ads. (cm^3)	Spec. CO_2 Ads. Capacity (cm^3/g)	BET Surf. Area (m^2/g)	Micropore Width (nm)			DR Pore Vol (cm^3/g)
						HK	DA	DR	
160	89.50	7.8	3.95	44	394	0.48	1.3	0.58	0.20
161	72.45	6.9	2.53	35	292	0.48	1.8	1.21	0.13
166	89.95	8.9	4.05	45	762	0.48	1.5	0.75	0.39
167	92.27	8.7	4.04	44	891	0.49	1.5	0.76	0.49
170	74.89	10.3	3.9	52	1132	0.47	1.6	0.76	0.48
46	73.88	8.5	3.2	43	1461	0.62	1.3	0.67	0.73
Coconut shell carbon	90.22	8.3	3.8	42	168	0.5	1.6	-	-

Large CO_2 uptakes were measured for the CFCMS samples. As a comparison a commercial coconut shell carbon was evaluated, and was shown to have adsorbed ~20% less CO_2 than our best CFCMS. Moreover, the adsorption process was significantly slower in the case of the coconut shell carbon, where resorption of the CO_2 on cooling from the temperature swing took >2 hours compared with <1 hour for the CFCMS materials. The superior adsorption kinetics of the CFCMS are ascribed to the small diameter of the carbon fibers (10-20 μm) compared to the ~2-3 mm of the coconut shell carbon. The diffusion path for the CO_2 to an adsorption site is, therefore, substantially shorter in the case of the CFCMS. The CO_2 adsorption capacity of CFCMS is clearly related to the BET surface area and micropore volume, as shown in Figs. 5 and 6, respectively. The weight percent of CO_2 adsorbed increases with increasing pore volume and BET surface area, apparently reaching peak adsorption capacity at micropore volumes of ~0.5 cm^3/g and BET surface areas of ~1000 m^2/g (e.g., sample 170). Figure 7 shows CO_2 uptake plotted as a function of micropore size (DR method). The optimum pore size appears to be ~0.8 nm. Significantly, samples 161 and 160 showed the lowest CO_2 uptakes (6.9 and 7.8% respectively), yet they possessed the largest and smallest mean micropore sizes (1.21 and 0.58 nm) respectively, suggesting a strong sensitivity of CO_2 uptake to the micropore size.

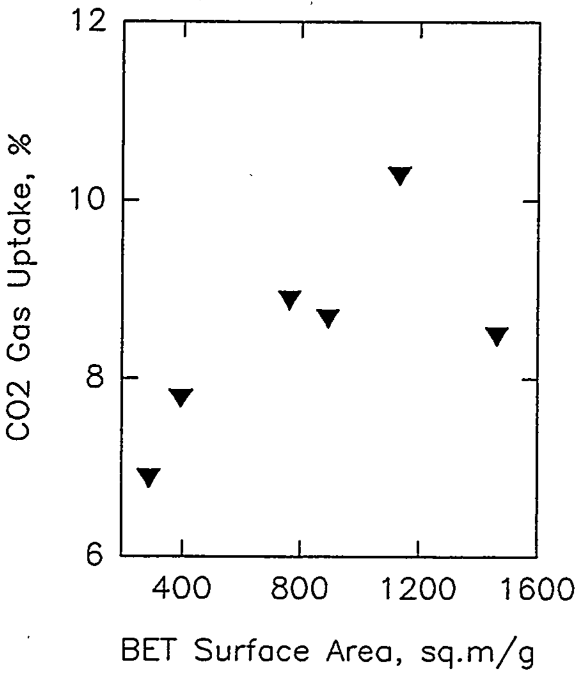

Fig. 5. The relationship between CO_2 uptake and BET surface area for CFCMS.

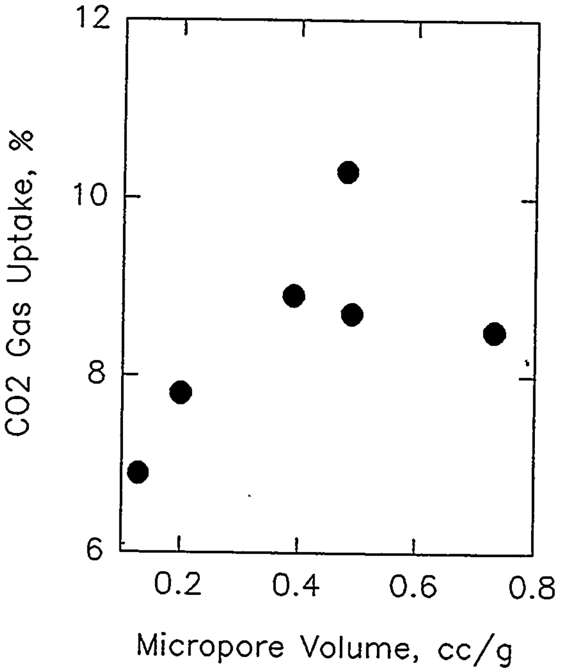

Fig. 6. The relationship between CO_2 uptake and micropore volume for CFCMS.

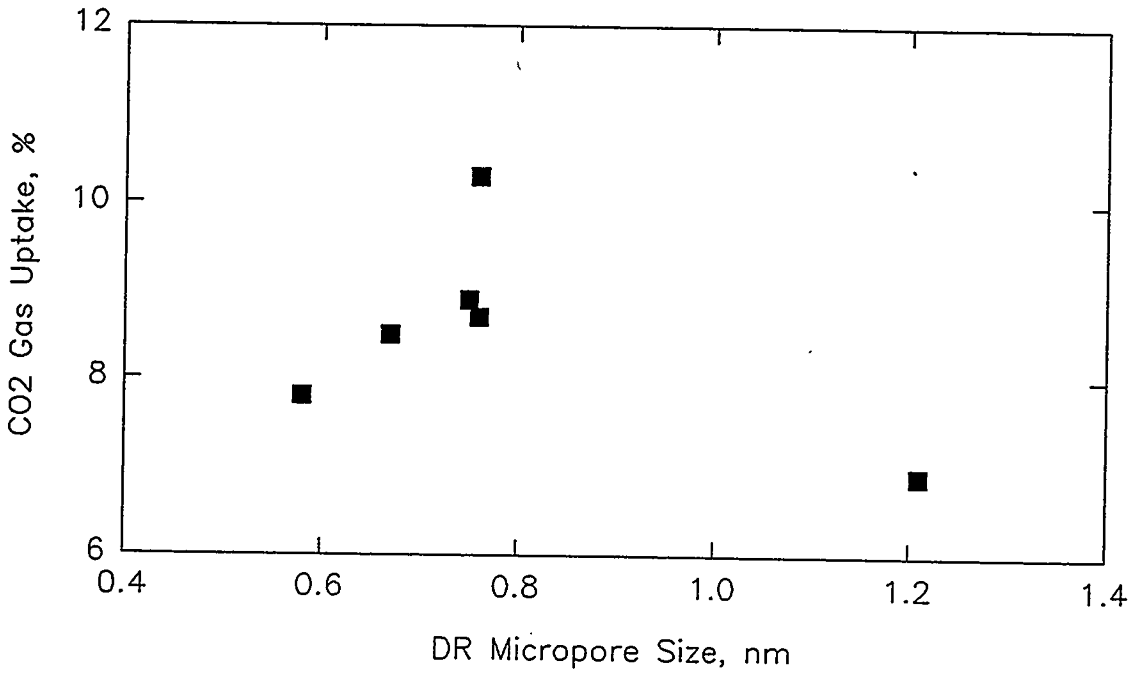

Fig. 7. The relationship between CO_2 uptake and mean micropore size for CFCMS.

Mesoporous Carbon Fiber Monoliths

A series of carbon fiber monoliths[5] were prepared from PAN derived carbon fibers and activated to burn-offs (% weight loss on activation) up to ~22%. Subsequent characterization using mercury porosimetry revealed the material to be highly mesoporous. Figure 8 shows the cumulative mesopore surface area as a function of pore diameter. The surface area is clearly associated with pores of size <50nm, i.e., the mesopores. The carbonized monoliths exhibited surface areas >500 m^2/g and mesopore volumes >1 cm^3/g. In contrast, the as-received PAN fibers exhibited a mesopore volume of only 0.28 cm^3/g. Evidently, the carbonization process radically affects the PAN fiber pore structure, possibly by opening the surface pores sufficiently to make the internal pores accessible. Access to the fiber's internal pore structure could occur when reactive species such as O_2, CO_2, H_2O and CO (which were adsorbed during monolith manufacture) are subsequently desorbed during carbonization and gasify the carbon.

The effect of steam activation on the mesopore volume is shown in Fig. 9. The mesopore volume was found to rapidly decrease with increasing burn-off, from >1 cm^3/g at zero burn-off to <0.4 cm^3/g at ~10% burn-off. Similarly, the mesopore surface area was found to decrease with increasing burn-off, falling from >500 m^2/g at zero burn-off to <200 m^2/g at ~10% burn-off (Fig. 10). The mean mesopore diameter is shown as a function of burn-off in Fig. 11. In the carbonized condition, the carbon fiber monoliths exhibited a mean mesopore width of ~7.2 nm. Activation caused the mean mesopore size to increase, reaching ~8.7 nm at the peak burn-off considered here.

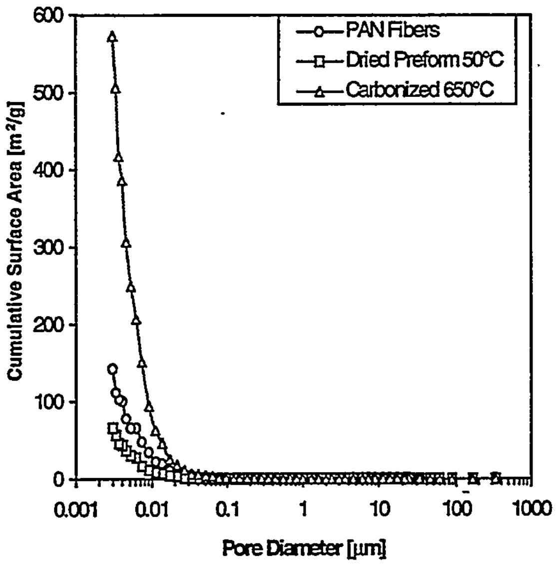

Fig. 8. Mesopore surface area as a function of pore diameter obtained from mercury intrusion data for our PAN derived carbon fiber porous carbon monoliths.

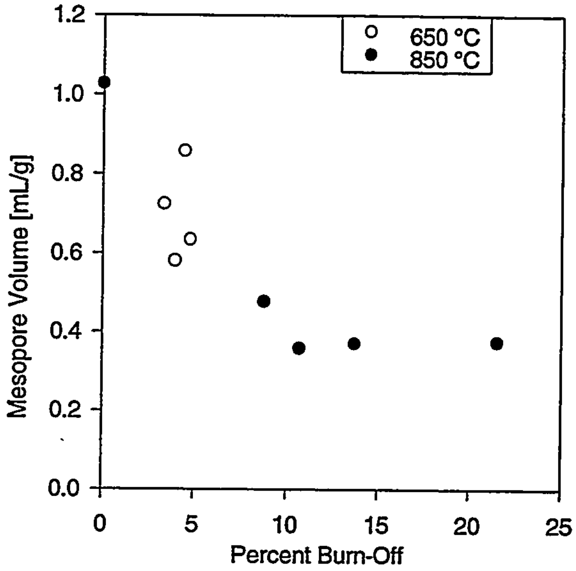

Fig. 9. Mesopore volume as a function of burn-off for our PAN derived carbon fiber porous monoliths.

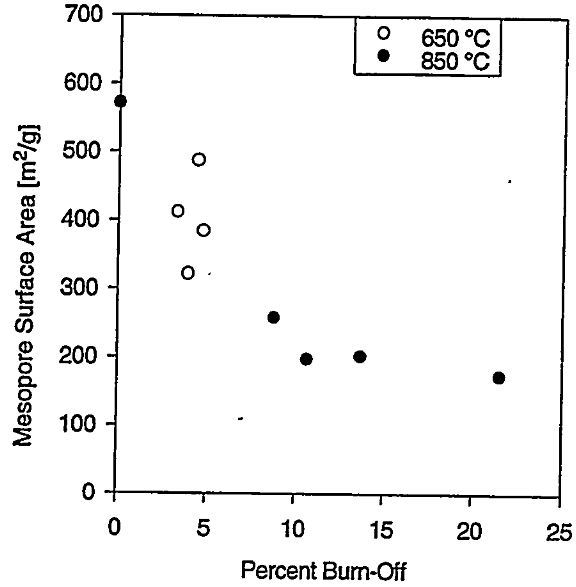

Fig. 10. Mesopore surface area as a function of burn-off for our PAN fiber derived porous carbon monoliths.

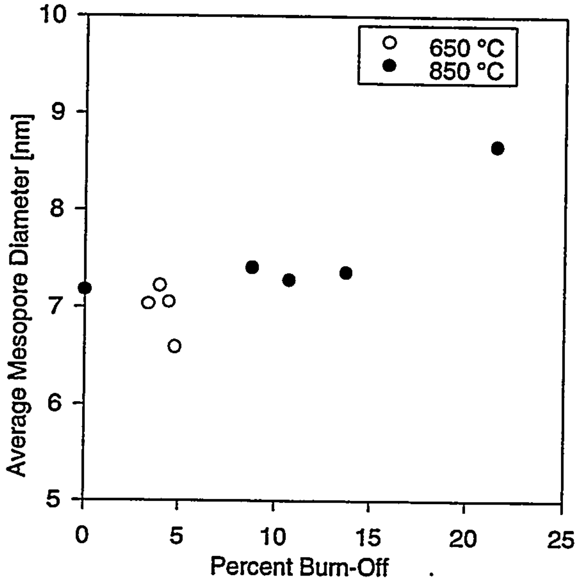

Fig. 11. Mean mesopore diameter as a function of burn-off for our PAN fiber derived porous carbon monoliths.

The large volume of mesopores observed in the PAN derived fiber monoliths is attributed to the fibril structure of PAN carbon fibers[6]. Typically[7], the crystallite size in a PAN fiber is ~1.6 nm. Moreover, there is extensive folding of the fibril nature of these crystallites, creating extensive pore networks in the mesopore size range, as confirmed by the data in Fig. 8. The modest increase of mesopore size with increasing burn-off (Fig. 11) suggests that the steam activation process affected very little change to the internal pore structure of the fiber. However, steam activation substantially reduced both the specific mesopore volume and associated specific mesopore surface area (Figs. 9 and 10). Moreover, SEM examination showed that the carbon fiber diameter reduced substantially during activation, indicating the fibers are consumed radially by a process of gasification of their external surface. The observed variations of pore size, pore volume, and surface area with burn-off could be readily explained if activation of the PAN carbon fibers occurred via a constant penetration depth, moving-front reaction. In such a process the pore structure would first be developed by gasification of the pore walls, increasing the pore size and volume. With further burn-off, the fiber itself is consumed, thus destroying the pore structure. As the reaction front moves from the periphery of the fiber toward its core, reducing the fiber diameter, the total volume of pores being created or developed is reduced. The high mesopore volume in the carbonized monolith suggests that, in this instance, activation is not required. Significant reductions in process time, and a beneficial cost saving, may thus be realized.

CONCLUSIONS

A novel porous monolithic carbon fiber composite material, known as CFCMS, has been developed and shows considerable potential for use in PSA gas separation systems. The material can be fabricated in large sizes yet retains the advantageous gas adsorption and separation properties of its precursor isotropic pitch derived carbon fibers. The CFCMS material structure contains large voids (>30 μm) between the 10-20 μm diameter fibers which allows for free flow of fluids through the material. A series of microporous CFCMS materials have been prepared and characterized. Their CO_2 adsorption characteristics were examined and determined to be superior to a commercially available activated carbon. The CO_2 adsorption capacity of CFCMS materials is related to both the BET surface area and the micropore volume, and appears to be particularly sensitive to the mean micropore size.

Mesoporous CFCMS materials were prepared from PAN derived carbon fibers. The materials exhibited mesopore volumes in excess of 1 cm^3/g and, therefore, are candidates for catalyst support applications. Steam activation of the monoliths increased the mean mesopore size only modestly, but reduced the mesopore volume and mesopore surface area significantly. The largest mesopore volumes were associated with the samples that had not been activated, but rather had only been carbonized. An activation and pore structure development mechanism was postulated to explain the pore characterization data obtained from mercury intrusion analysis.

ACKNOWLEDGEMENTS

Research sponsored by the U.S. Department of Energy, Office of Fossil Energy, Advanced Research and Technology Development Materials Program [DOE/FE AA 15 10 10 0, Work Breakdown Structure Element ORNL-1(E)] under contract DE-AC05-84OR21400 with Martin Marietta Energy Systems, Inc.

REFERENCES

1. T. D. Burchell, "Carbon Fiber Composite Molecular Sieves," in *Proc. Eighth Annual Fossil Energy Materials Conference*, Oak Ridge, Tennessee, May 10-12, 1994. CONF-9405143, ORNL/FMP-94/1, pp. 63-70, Pub. Oak Ridge National Lab., Aug. 1994.

2. Frank Derbyshire, "Activation and Micropore Structure Determination of Carbon Fiber Composite Molecular Sieves," in *Proc. Eighth Annual Fossil Energy Materials Conference*, Oak Ridge, Tennessee, May 10-12, 1994. CONF-9405143, ORNL/FMP-94/1, pp. 137-143, Pub. Oak Ridge National Lab., Aug. 1994.

3. S. Brunauer, P. H. Emmett, and E. Teller, *J. Am. Chem. Soc.,* Vol 60, p. 309 (1938).

4. George C. Wei and JM Robbins, "Carbon-Bonded Carbon Fiber Insulation for Radioisotope Space Power Systems," *Ceramic Bulletin*, Vol. 64, No. 5, p. 691 (1985).

5. J. W. Klett and T. D. Burchell, "Carbon Fiber Carbon Composites for Catalyst Supports," *Proc. 22nd Conf. on Carbon, San Diego, California, July 1995*, Pub. American Carbon Society.

6. R. J. Diefendorf and E. W. Tokarsky, *Polymer Eng. Sci.*, Vol. 15, P. 150 (1975).

7. J. P. Donnet and R. C. Bansal, *Carbon Fibers*, Pub. Marcel Dekker, Inc., New York (1990).

CARBON-FIBER COMPOSITE MOLECULAR SIEVES FOR GAS SEPARATION

M. Jagtoyen, F. Derbyshire, G. Kimber, Y. Q. Fei

University of Kentucky Center for Applied Energy Research,
3572 Iron Works Pike, Lexington KY 40511-8433, USA

ABSTRACT

The progress of research in the development of novel, rigid, monolithic adsorbent carbon fiber composites is described. Carbon fiber composites are produced at ORNL and activated at the CAER using steam or CO_2 under different conditions, with the aims of producing a uniform degree of activation through the material, and of closely controlling pore structure and adsorptive properties. The principal focus of the work to date has been to produce materials with narrow porosity for use in gas separations.

Carbon fiber composites are prepared at ORNL, usually in plate or tubular form, by vacuum molding from water slurries containing phenolic resin and chopped isotropic petroleum pitch fibers. The composites are activated at the CAER in steam or CO_2, using samples of dimensions up to 1.5 x 4 x 12 cm that are cut from the original larger plates. One of the objectives is to produce uniformly activated composites, which is especially critical when attempting to active large monoliths. It has been found that there are appreciable variations in the density and permeability of the as-formed composites that must relate to the forming technique. These variations are expected to exert some influence on the rate and extent of reaction and surface area development. In attempting to uniformly activate the composites, two reactor configurations have been investigated. In the more successful arrangement, steam is introduced at several points along the length of the composite. A reduction in steam partial pressure from 95 vol% to 44 vol% significantly improved the uniformity of surface area distribution. Activation with CO_2 was still better, which is attributed to the much slower reaction rate than with steam.

Measurements of composite dimensions have shown that there is an overall shrinkage during activation. A direct correlation is found between dimensional shrinkage and burnoff, and is similar for CO_2 and steam activation. The causes of the shrinkage are not yet clear. At levels of burnoff above about 40%, the extent of contraction is sufficient to produce stresses that result in fracture.

Activated composites have been evaluated for the separation of CH_4-CO_2 mixtures, and an apparatus has been constructed specifically for this purpose. Samples activated to low burnoff (5-7% wt loss) with low surface areas (from 300-500m^2/g) give much better separation of CO_2 and CH_4, than samples produced at higher burnoff, and there appears to be no benefit in producing composites at burnoffs higher than 10%. The greater separation efficiency obtained at low burn-off means that the most effective CFCMS can be produced at relatively low cost. Continuing work will attempt to define the parameters that influence this gas separation, and whether these are applicable to other gas mixtures.

INTRODUCTION

This project involves collaborative research between the ORNL and the CAER, for the development of novel, rigid, monolithic adsorbent carbon fiber composites that can be produced in single pieces to a given size and shape. The concept has resulted in the filing of a patent application that is held jointly between researchers at these two organizations. Because of their potential molecular sieve properties, the composites have been termed carbon fiber composite molecular sieves, or CFCMS. The carbon fiber composites are produced at the ORNL and activated at the CAER using steam or CO_2 under different conditions, with the aims of producing a uniform degree of activation, and of closely controlling pore structure and adsorptive properties. The principal aims of the work to date have been to produce uniformly activated samples with narrow porosity for use in gas separations, although numerous other areas of application are envisaged.

The project originated in research conducted at the ORNL in the 1980s[1]. A carbon fiber composite material was developed as a low-density, mechanically strong thermal insulator for a radioisotopic heat source on spacecraft for the Galileo and Ulysses Missions. The material was prepared by vacuum molding from water slurries containing chopped carbonized rayon fibers (~ 6.5 μm diameter x ~ 0.15 mm) and a particulate phenolic resin. The slurry was vacuum molded into tubular or plate configuration, followed by drying, curing, and carbonization to 1600°C.

The basis for the present project was to use the above technique to produce high surface area carbon fiber composites through the activation of similar composites, in which porosity is developed in the carbon fibers to produce high surface areas for adsorption. One of the principal changes, compared to the original work, is to utilize lower cost carbon fibers that are produced form isotropic pitches (other types of fiber will also be included in the studies). In recent years, a great interest has developed in the activated forms of such isotropic carbon fibers, where high surface areas can be produced by partial gasification in steam or other oxidizing gas[2,3]. Moreover, while porosity can be generated in most types of carbon fiber, low-modulus fibers produced from isotropic pitch are particularly suited for activation due to their unique structure in which the random packing of small crystallites allows the development of an extensive pore structure. It was also assumed that the ease and kinetics of activation should be much more favorable than with high performance fibers which, in addition to possessing different structure, have been subjected to elevated temperatures. Early results confirmed this supposition, in that it was found that isotropic fibers that had been heat treated to 1600°C were much more difficult to activate than fibers that had been heat treated to 1100°C.

The interest in activated carbon fibers as adsorbents is that they have novel properties that make them more attractive than conventional forms of activated carbons (powder or granular) for certain applications[3]. Among their possible uses, activated carbon fibers are of interest for: the adsorption and recovery of organic vapors; environmental protection; the removal of SO_x and NO_x from flue gas; the improvement of air quality; and water treatment[3-8]. Difficulties in handling and utilizing activated fibers can be surmounted by their incorporation into composites, such as woven and non-woven fabrics, felt, and paper. Hence, the interest in producing rigid adsorbent composites.

This paper provides an account of studies of composite activation, the measurement of physical properties (dimensional changes during activation, gas permeability), and the results of preliminary experiments to evaluate the effectiveness of CFCMS for the separation of gas mixtures.

DISCUSSION OF CURRENT ACTIVITIES

Experimental

Composite Preparation

Carbon fiber composites are prepared at ORNL by vacuum molding from water slurries containing phenolic resin and chopped isotropic petroleum pitch fibers, (P-200, ~ 17.5 µm diameter, average length 380µm, supplied by courtesy of Ashland Carbon Fibers Division, Ashland Inc.). The slurry is vacuum molded into tubular, plate or rod configuration, followed by drying, curing, and carbonization to about 650°C. The carbon fiber composites are supplied to the CAER usually in the form of plates (28 x 12 x 1.5 cm).

Activation

The composites are activated in steam or CO_2, using smaller samples (dimensions 1.5 x 4 x 12 cm) that are cut from the original plates. Activation is conducted in a Lindberg tube furnace at temperatures between 800 and 950°C, for reaction times from 0.5-4 hours. Surface areas and pore size distributions are determined for samples taken from selected areas of the activates, using a 10 port automated surface area analyzer, OMNISORB 610. The high efficiency of this instrument allows the measurement of surface area and the characterization of pore sizes down to 4 A, using nitrogen at 77K and CO_2 at 298K as adsorbents.

Results and Discussion

Activated carbon fibers produced from isotropic petroleum pitch have been reported to develop high surface areas (in some cases up to 2000 $m^2 g^{-1}$), with almost all of the pore volume present in micropores (< 2nm diameter pores)[3]. These properties are retained by the composites, as illustrated in Table 1, where the nitrogen BET surface area is shown as a function of burn-off in steam (percent weight loss during activation). It can be seen that high surface areas can be attained at moderate burn-off.

The pore size distribution is narrow, although it broadens with increasing activation: the average pore width increases from 0.58 to 0.83 nm as the burn-off with steam increases from 16 to 31%. The sample at 16% burn-off has the narrowest pore size distribution with almost all pores less than 6 nm in diameter, while the more activated samples have significant proportions of pores from 6-8 nm in diameter. Depending on the application, a compromise may be required between pore size distribution and total surface area. Samples activated in CO_2 show the same trend in surface area development as the steam activated samples. At comparable levels of burnoff the BET surface area is 566 m^2g^{-1} for steam and 527 m^2g^{-1} for CO_2 while the pore widths are similar, 0.58 nm vs 0.62nm, Table 1.

Table 1: Surface area and average pore size for CFCMS at different levels of burnoff in steam and CO_2

Burnoff	BET(m^2g^{-1})	Average pore size(nm)
Steam (concentration: 97 vol %)		
16	566	0.58
20	936	0.75
31	1240	0.83
CO_2 (concentration: 100 vol %)		
13	512	0.60
18	527	0.62
36	800	0.76

Uniformity of Composites and Activated Composites

One of the main concerns in this work is to be able to uniformly activate the composites: this consideration will become especially critical when attempting to activate large monoliths, where diffusion of activating gas to the center of the artifacts could present a limiting factor. Consequently, a great deal of effort has been taken to ensure uniform activation. Since the start of the project, the activation procedure has been progressively modified in order to establish furnace conditions that will help to realize this objective. One factor that cannot be controlled through the activation however, is the uniformity of the composite blocks as they are received from ORNL. Before discussing further the activation process, the uniformity of the as-received composites will be addressed.

Uniformity of as-received composites. A sample of composite, 28 x 12 x 1.5 cm, supplied by ORNL (UK-10-2) was examined for consistency of density, thickness and permeability by removing 18 nominally 1" cores and measuring them individually.

The results showed that density was the least variable parameter. Even so, the variation was 0.347 to 0.382 g/cc. The thickness of the block was extremely variable with a range of 13.4 to 17.8 mm. The thicker areas did not seem to be directly linked to the higher density areas. Similarly, no correlation was obvious between density and permeability (for measurement details see later section). Thus, there is far from equal resistance to flow over the whole plate area, which could obviously affect the distribution of the activating gas, and the removal of the products of the gasification reactions. These variations in the physical parameters must result from the forming technique and are expected to exert some influence on the rate and extent of activation reaction and surface area development.

Uniformity of Activation. The principal parameters that can be varied in the activation process are, the reactor design and configuration, the partial pressure of the activating gas, total flow rate, temperature and reaction time.

Two different reactor arrangements have been investigated. In the first configuration, steam was introduced at several points along the length of the composite. In the second, the steam was introduced at one end only and passed downstream over the composite. The uniformity of activation was tested by measuring BET surface areas on sub-samples taken from different positions in the composite (dimensions 1.5 x 4 x 12 cm). The first reactor was found to give a much smaller spread of results, with standard deviations in BET surface area of 2-12% as opposed to 18-50% for the other reactor.

Another factor that will influence uniformity of the composites is the partial pressure of the activating gas. In initial experiments, essentially pure steam (95 vol%) was used as the activating agent. Water at a flow rate of 60cc/hr was mixed with nitrogen at 80cc/min. These conditions resulted in non-uniform surface area development throughout the sample (deviation around 10-30%), which was attributed to the high concentration of steam. When the steam concentration was reduced to 61vol % and 44 vol%, the uniformity improved significantly. The standard deviation in surface area along the 12cm length of sample came down to 7 and 2% respectively. In future studies a concentration of 44 vol% H_2O in N_2 or less will be used to achieve uniform activation.

Activation with CO_2 is found to give more uniform surface area development than steam, with only a 8% variation in BET surface area. CO_2 activation gives a slightly different pore size distribution than steam activation[9]. There is a significantly slower reaction rate than with steam, since the larger dimension of the CO_2 molecule results in a slower diffusion into the porous system and is more restricted in its access to the micropores. The CO_2 activation runs were therefore carried out at higher temperatures (850-950°C), for 1-3 hours, and at a rate of 2l/min.

Dimensional Changes

There is an overall shrinkage of the composites during activation. The changes have been measured in all three directions of the composite. A direct correlation is found between dimensional shrinkage and burnoff, and is similar for CO_2 and steam activation.

It has been reported that carbon shrinkage can be caused by direct reaction between O_2 and C, as carbon is directly removed from exterior surfaces. At temperatures above 800°C, oxygen is known to react more than 100 times faster with carbon than steam and CO_2, which leads to a diffusion-controlled reaction involving a shrinking core type of mechanism, and there is minimal contribution to porosity development. In the present studies, there should only be low concentrations of oxygen present, and the causes of the shrinkage are not clear. External burn-off in the activant gas could make some contribution, but this is expected to be small. Another factor might be degradation of the binder. In any event, at high levels of burnoff, above about 40%, the extent of contraction produces stresses in the composites that result in fracture in a plane parallel to the plane of deposition when the composite was first formed by filtration.

Permeability and Adsorptive Properties

The permeability of the composites and activates has been measured by a simple apparatus where the sample under test is sealed in a plastic funnel using foam rubber. Air is passed through the sample at a rate of 15-60 l/min, and the differential pressure over the sample is measured using a water manometer. For a composite of thickness 13mm, an air flow of 15 l/min through a disc of diameter 25 mm (i.e. 30 m^3/min per m^2) generates a pressure differential less than 0.5 psi. This permeability is comparable to that of an equivalent bed depth of 2 mm sized granules, and much higher than for a similar bed of 14 micron sized powder. The high permeability is due to the very open structure of the composites.

The rate of gas adsorption on CFCMS has been compared with that on other carbons by thermogravimetric analysis using NO as the test adsorbate. The rate of adsorption on activated carbon fiber composites is found to be much higher than on a granular commercial coconutshell derived carbon, Figure 1, due to the essential absence of diffusion limitations in the carbon fiber composite. Only when the granular carbon is reduced to a comparable particle size (average diam 14 microns vs 12-15 microns fiber diameter) do the rates begin to correspond. The high adsorption rate is another benefit of the open architecture of the composite since the fibers within are almost as accessible as free fibers. The materials will therefore have high potential for processes requiring rapid adsorption and desorption rates, e.g. gas separation, solvent recovery etc.

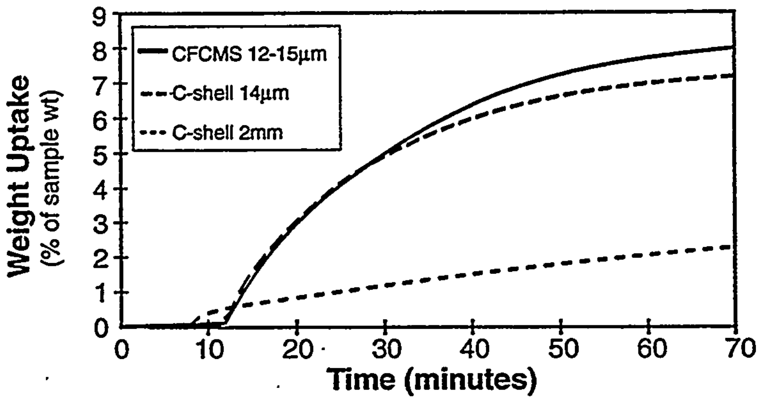
(NO Adsorption at 28°C, no oxygen;
C-shell = Commercial coconut shell carbon)

Figure 1: Adsorption rates of CFCMS compared with a commecial granular activated carbon at two particle sizes, granulars at 2mm and finely ground to 14μm.

Gas Separation

The unique properties of the activated composites - narrow, unimodal pore structure, high surface area, rapid rates of adsorption and desorption, the ability to form specific shapes of high permeability and strength - suggest that, among other applications, they may be suitable for molecular separation on the basis of size and shape. The system CH_4 - CO_2 was selected as the model mixture, following studies of the adsorption of these gases by TGA which showed that the carbons have high capacity for adsorbing CO_2 (up to 10 wt%) while much less methane is adsorbed, Figure 2.

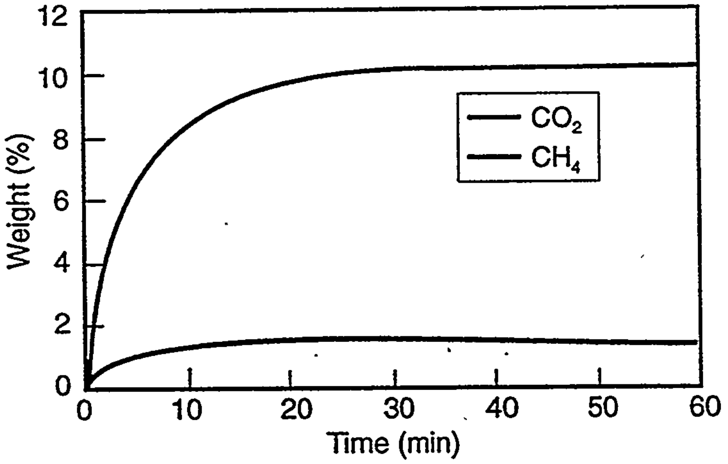

Average pore width, L = 0.74 nm
BET surface area = 822m^2/g

Figure 2: Adsorption of CH_4 and CO_2 on CFCMS using TGA (STP).

An apparatus was then constructed to examine the effectiveness of CFCMS for gas separation, Figure 3. Samples have been tested using a mixture of 75% CH_4 and 25% CO_2. The composition and flow rate of the emergent gases are detected as a function of time using a mass spectrometer and a mass flow meter. The sample is sealed in place using a rubber seal. Helium is first purged through the system and when the gas analysis indicates that virtually pure helium is emerging at the outlet, the valve is switched and the 75%CH_4/ 25% CO_2 mixture is introduced at a fixed controlled flow rate (usually 50 ml/min). The outlet flow rate and composition is then monitored and recorded for 10 minutes. Initially, for an activated sample there is a period of time when the outlet flow is very low, as most of the CH_4 and CO_2 flowing into the sample is adsorbed. Then, relatively pure methane begins to be detected. After about 10 minutes, the outlet gas composition has returned to that of the original mixture 75% CH_4, 25% CO_2. The volumes of gas produced per gram of composite with 95%, 90% and 85% CH_4 concentration are then calculated.

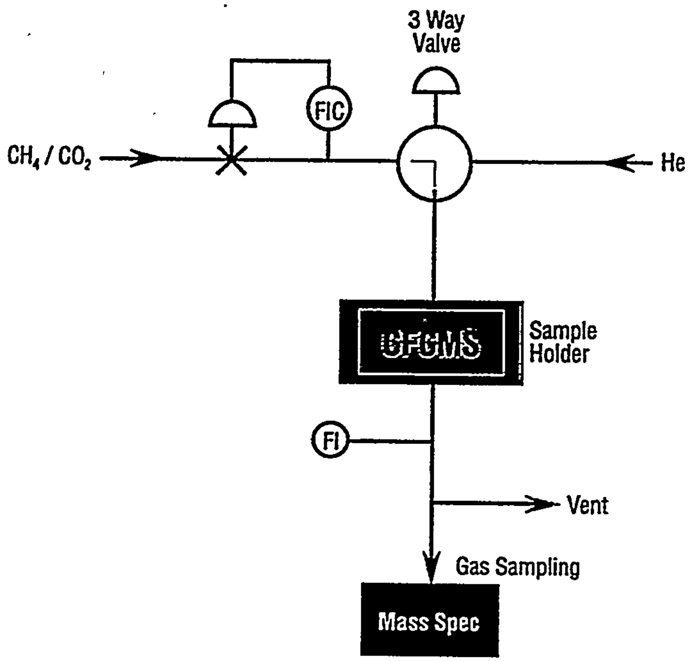

Figure 3: Schematic Arrangement of Apparatus for testing Gas Separation.

Results of the gas separation experiments are shown in Table 2. Samples activated to low burnoff (5-7% wt loss) and low surface areas (from 300-500m^2/g) show excellent separation of CO_2 and CH_4, compared to samples produced at higher burnoff (10-30% wt. loss, surface area 500-1000m^2/g). The volumes of effluent gas produced at 95 and 90% methane concentration are shown in Table 2 as a function of burn-off. The most effective carbons are produced at low burn-off, and there appears to be no benefit in producing composites at burnoffs higher than 10%. The same trend is reflected in the relationship between micropore volume and efficiency for separation, Table 2, from which it appears that the ideal micropore volume should be less 0.15 cc/g. These results are rather unexpected. The greater separation efficiency obtained at low burn-off means that the most effective CFCMS can be produced at relatively low cost. However, there remain the questions of defining the parameters that influence this gas separation, and whether these are applicable to other gas mixtures.

The influence of average pore diameter on the separation process and production of high purity methane is shown in Figure 4. From these data, the optimum pore diameter is seen to be in the range 0.7 - 1.0 nm. However, other parameters such as surface chemistry cannot be neglected. Future work will be directed to further elucidating the CFCMS parameters that are most important to the separation process.

Table 2: Volume of CH_4 produced at 95-85% concentration from a mixture of 75%CH_4/25%CO_2

Sample	Cumul. vol of CH_4 out(cc)		Burn -off	Activation			BET	pore	pore
	95%	90%	(wt %)	agent	temp (°C)	time (hr)	s.area (m^2/g)	volume (cc/g)	diameter (A)
SA124	-	47	24	CO_2	900	3	632	0.2	5.8
SA139	33	69	8	H_2O	850	1/4	444	0.26	12.0
SA 132	35	67	8	CO_2	850	2	424	0.19	7.6
SA 135	39	78	12	CO_2	850	4	548	0.23	5.9
SA 136	44	80	7	CO_2	1000	1/60	291	0.11	11.0
SA 137	53	87	7	CO_2	950	1/6	397	0.13	8.8

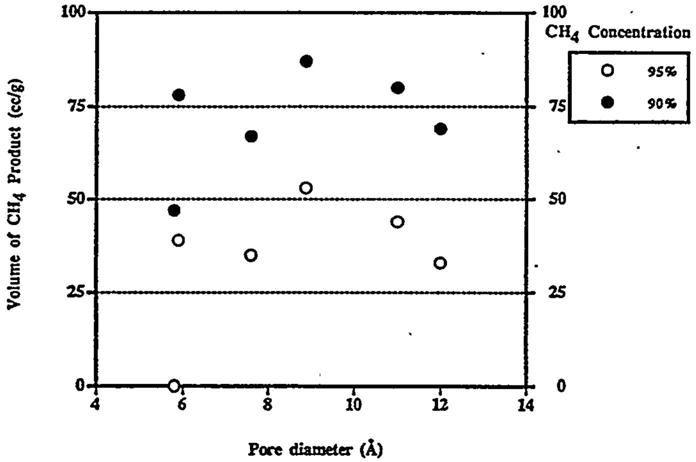

Figure 4: **Relationship of average pore diameter to volume of effluent gas produced with high CH_4 purity.**

REFERENCES

1. G. C. Wei, and J. M. Robbins, Ceramic Bull., 64(5), p. 691, 1985.
2. M. W. Thwaites, M. L. Stewart, B. E. McNeese, and M. Sumner, Fuel Proc. Tech., 34, 137, 1993.
3. M. Suzuki, Proc. Biennial Carbon Conference, Buffalo, 1993.
4. I. Mochida, Y-N. Sun, H. Fijitsu, S. Kisamori, and S. Kawano, Nippon Kagaku Kaishi, (J. Chemical Society of Japan), 6, 885-890, 1991.
5. I. Mochida, T. Hirayama, S. Kisamori, S. Kawano, and H. Fijitsu, Langmuir, 8 (9), 2290, 1992.
6. K. L. Foster, R. G. Fuerman, J. Economy, S. M. Larson, and M. J.Rood, Chem. Mater., 4, 1068-1073, 1992.
7. J. Economy, K. Foster, A. Andreopoulos, and H. Jung, Chemtech, 597-603, October 1992.
8. M. Suzuki, Water Science technology, 23, p. 1649, 1991.
9. T. Wigmans, Carbon Vol. 27. No. 1. pp. 13-22, 1989.

STABILITY OF SOLID OXIDE FUEL CELL MATERIALS

T.R. Armstrong, L.R. Pederson, J.W. Stevenson, and P.E. Raney

Materials Sciences Department
Pacific Northwest Laboratory[1]
P.O. Box 999
Richland, WA 99352

ABSTRACT

The phase stability and sintering behavior of materials used in SOFCs has been evaluated. The sintering behavior of Ca and Sr doped lanthanum manganite (the preferred SOFC cathode material) is highly dependent on the relative proportion of A and B site cations in the material. Ca and Sr doped lanthanum chromite (the preferred interconnect material) have been shown to rapidly expand in reducing atmospheres at temperatures as low as 700°C. This expansion is due to the reduction of Cr^{4+} to Cr^{3+} in reducing environments.

INTRODUCTION

Doped lanthanum chromite and lanthanum manganite have been extensively studied over the past two decades for use in high-temperature solid oxide fuel cells (SOFC). Lanthanum chromite for use as an interconnect and lanthanum manganite as the SOFC cathode. The requirements on materials used in SOFCs is severe. The chosen interconnect material must be stable in both oxidizing and reducing atmospheres, have a high electronic conductivity, high thermal conductivity, a thermal expansion match to yttria stabilized zirconia, and be chemically compatible with the other fuel cell materials. The material chosen for the cathode must be stable in air at 1000°C and have high electronic conductivity. The thermal expansion must be compatible with the yttria-stabilized zirconia (YSZ) electrolyte, and chemical interaction with the electrolyte and interconnect materials must be minimal. Also, the cathode material must maintain a porous microstructure during operation to allow adequate diffusion of gaseous oxygen through the cathode to the cathode/electrolyte interface

---

[1] Operated for the U.S. Department of Energy by Battelle Memorial Institute under contract DE-AC06-76RLO 1830

Reproducible fabrication of SOFCs requires a thorough knowledge of the sintering behavior of the chosen cathode and interconnect material. Important factors affecting densification include temperature, type and amount of dopant, and cationic stoichiometry (i.e., relative proportion of A and B site cations). Additionally, these materials must be stable over a wide range of temperatures and oxygen partial pressures. The objective of this work is two-fold: 1) to evaluate the sintering behavior of doped lanthanum manganite with and without the addition of sintering aides and 2) to evaluate the phase stability of lanthanum chromite over a range of oxygen partial pressures and temperatures.

SINTERING OF LANTHANUM MANGANITE

Doped $LaMnO_3$ has a perovskite-type structure. The sintering behavior of these manganites is highly dependent on the ratio of A-site cations (La, Sr, Ca) to B-site cations (Mn) in the material. LSM-16, LSM-24, and LCM-20 were prepared with A/B cation ratios of 0.91, 0.95, 0.98, 1.00, 1.02, and 1.05. LSM-10 with A/B = 0.98 was also prepared. Since A and B sites are present in a 1:1 ratio, and all ions present in the structure occupy regular lattice sites[1], those ratios would correspond to $(La_{1-y}M_y)_{0.91}MnO_3$, $(La_{1-y}M_y)_{0.95}MnO_3$, $(La_{1-y}M_y)_{0.98}MnO_3$, $(La_{1-y}M_y)MnO_3$, $(La_{1-y}M_y)Mn_{0.98}O_3$, and $(La_{1-y}M_y)Mn_{0.95}O_3$ (M = Ca or Sr), respectively, assuming single phase materials. While compositions near the stoichiometric point (A/B = 1) were single phase perovskites, other compositions contained small amounts of additional phases, as discussed below. Although manganites can also exhibit oxygen nonstoichiometry, that nonstoichiometry in highly doped manganites tends to be relatively small[2]. For convenience, therefore, an oxygen stoichiometry of 3 (rather than $3 \pm \delta$) is used in this article.

Sintered (1350°C for 1 hour) densities for LSM-16, LSM-24 and LCM-20 (calcined at 650°C for 0.5 hour) are shown as a function of A/B cation ratio in Figure 1. The green densities were essentially independent of A/B cation ratio, whereas the sintered densities were highly dependent on the A/B ratio, with A-cation deficient compositions (A/B ratio < 1) exhibiting substantially higher densities than the stoichiometric and B-cation deficient manganites. This pronounced effect of A/B cation ratio on densification behavior was also observed in measurements of the linear shrinkage of green compacts as a function of temperature. For example, sintering shrinkage plots for LSM-24 are shown in Figure 2.

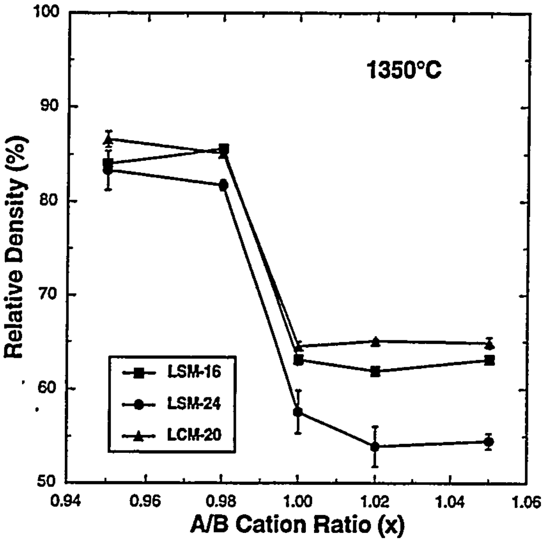

Figure 1. Relative densities of lanthanum manganites as a function of A/B ratio. Specimens sintered in air at 1350°C for 1 hour.

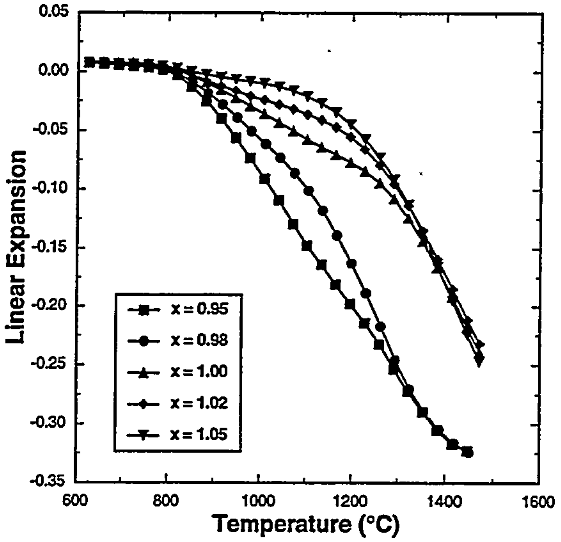

Figure 2. Sintering shrinkage plots for LSM-24 with varying A/B ratio. Specimens heated at 2°C/min in air.

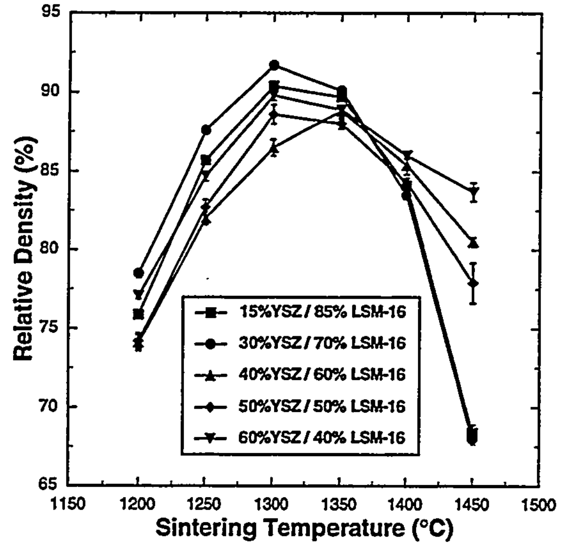

Figure 3. Relative densities of LSM-16/ YSZ mixtures sintered in air at the indicated temperatures.

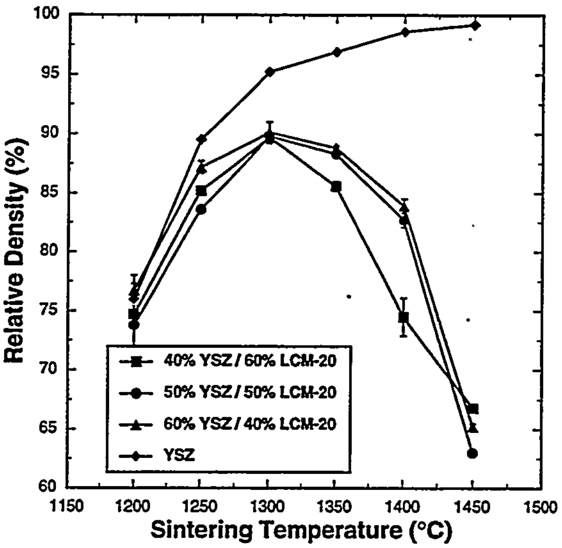

Figure 4. Relative densities of LCM-20/ YSZ mixtures sintered in air at the indicated temperatures.

These plots show an enhancement of shrinkage for the A cation deficient manganites. The shape of these shrinkage plots is consistent with a solid state sintering mechanism, with no signs of sudden shrinkage events (nearly vertical regions in the plot) resulting from liquid phase formation.

The higher densities obtained in the A-site cation deficient manganites suggests that the diffusion of A-site cations is the limiting factor in mass transport during densification[3]. Preparation of manganites with A/B < 1.00 should result in an excess concentration of A-site vacancies within the structure. When additional A-site vacancies are present in the structure, A-site cation diffusion occurs more readily, allowing for higher sintered densities. This agrees with conclusions drawn by van Roosmalen et al.[4] for undoped lanthanum manganite. Since sintered density was not significantly affected by B-site cation deficiency, the diffusion of B-site cations does not appear to be a limiting factor during sintering.

Sintered densities of mixtures of YSZ/LSM-16 and YSZ/LCM-20 are shown in Figures 3 and 4, respectively. Sintered densities for YSZ alone (also shown in Figure 4) increased uniformly with increasing sintering temperature. For the manganite/YSZ mixtures, however, densities increased with increasing temperature until reaching a maximum around 1300°C. At higher temperatures, the densities tended to decrease substantially with increasing temperature. High porosity is essential for the SOFC cathode. It is clear from Figures 3 and 4 that the degree of porosity of the sintered mixtures can be varied over a wide range by changing the sintering temperature. In practice, the introduction of pore formers, such as organic materials which can be removed at low temperatures, may be a preferable means of obtaining the desired level (and morphology) of porosity.

One of the potential advantages of the addition of YSZ to lanthanum manganite is an improved thermal expansion match between the cathode and the YSZ. The average TECs (between 25 and 1000°C) of LSM-16 (10.0×10^{-6} K^{-1}) and LCM-20 (10.5×10^{-6} K^{-1}) were close to that of YSZ (10.2×10^{-6} K^{-1}). The average TEC for LSM-24 was considerably higher (11.2×10^{-6} K^{-1}). These observed values for Sr-doped lanthanum manganite are similar to those reported by Aizawa et al.[5] and somewhat lower than values reported by Srilomsak et al.[6]. For LCM-20, the deviation from YSZ could be eliminated by adding 15% or 50% YSZ. For LSM-16, the addition of 50% YSZ also resulted in a close match to YSZ. However, a 15% addition of YSZ to LSM-16 did not improve the match to YSZ but instead resulted in an increased thermal expansion (11.1 x 10^{-6} K^{-1}).

Some SOFC designs require co-sintering of the cathode and YSZ. Successful co-sintering requires a close match in the sintering behavior of both materials. Plots of sintering shrinkage (with and without YSZ additions) as a function of temperature are shown for LSM-16 and LCM-20 in Figures 5 and 6, respectively. The mismatch between the shrinkages of YSZ and the manganites without YSZ additions is apparent. In the case of LSM-16, the addition of 15 vol.% YSZ improved the match to YSZ significantly, except at high temperature (above 1400°C) where there was evidence of swelling of the specimen. Increasing the addition to 50 vol.% had little further effect on the shrinkage behavior. For LCM-20, the match was improved slightly by the YSZ additions. At high temperatures, substantial swelling was observed in the YSZ/LCM specimens; swelling also occurred to a lesser degree in the YSM/LSM specimens. This swelling may occur as a result of oxygen evolution from the perovskite lattice at elevated temperatures. If the specimen has sintered sufficiently to close off the internal pores from the surface, oxygen leaving the lattice will be trapped within the bulk of the specimen and may cause bloating. This mechanism may explain the low densities observed for the YSZ/manganite mixtures sintered at high temperatures (Figures 3 and 4).

The sintering behavior of doped lanthanum manganite and yttrium manganite was determined to be highly sensitive to changes in the A/B cation ratio. Manganites synthesized with a deficiency of A-site cations exhibited enhanced densification behavior relative to B-site cation deficient manganites. Maximum sintered densities of mixtures of lanthanum manganite and YSZ were obtained by sintering at 1300°C. Higher sintering temperatures resulted in lower densities. The addition of YSZ to the manganites resulted in reduced electrical conductivity but allowed for tailoring of the thermal expansion and sintering shrinkage. Small quantities of $La_2Zr_2O_7$ were formed during sintering of mixtures of YSZ and slightly A cation deficient manganites (i.e., A/B = 0.98). The formation of $La_2Zr_2O_7$ during sintering was suppressed in mixtures of YSZ and Mn-enriched manganites (A/B = 0.91). Thus, judicious selection of the A/B cation ratio and amount of YSZ addition may result in SOFC cathodes with adequate electrical conductivity, thermal expansion and sintering shrinkage matched to the YSZ electrolyte, and minimal deleterious interaction with the YSZ.

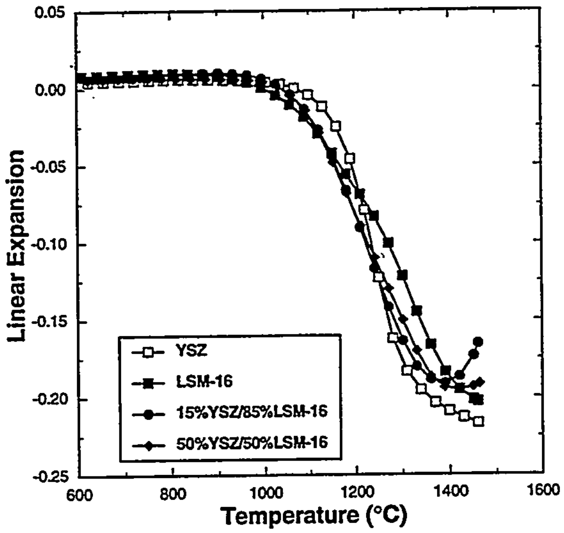

Figure 5. Sintering shrinkage plots for LSM-16/YSZ mixtures. Specimens heated at 2°C/min in air.

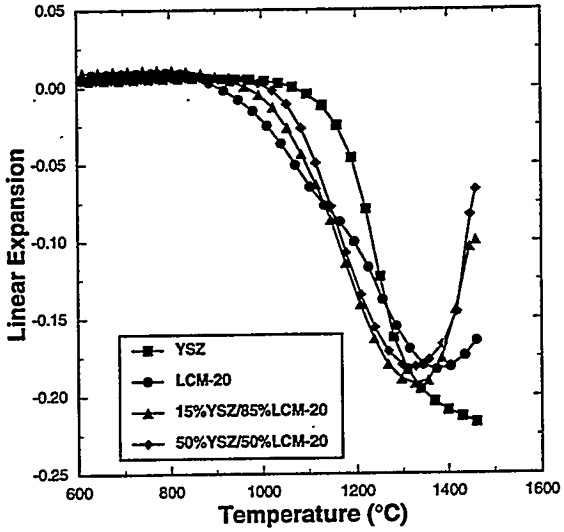

Figure 6. Sintering shrinkage plots for LCM-20/YSZ mixtures. Specimens heated at 2°C/min in air.

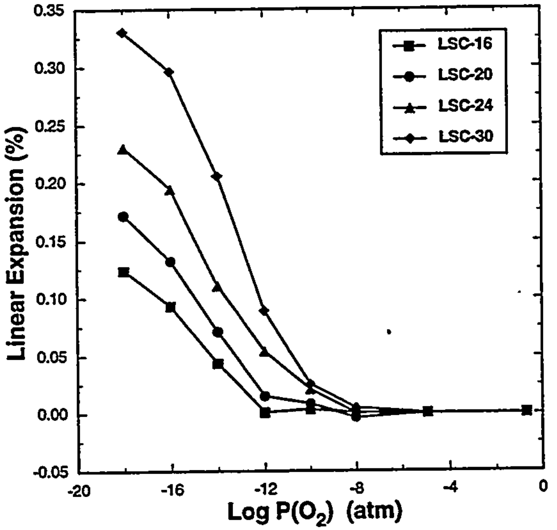

Figure 7. Linear Expansion of $La_{1-x}Sr_xCrO_3$ as a Function of Oxygen Partial Pressure at 1000°C.

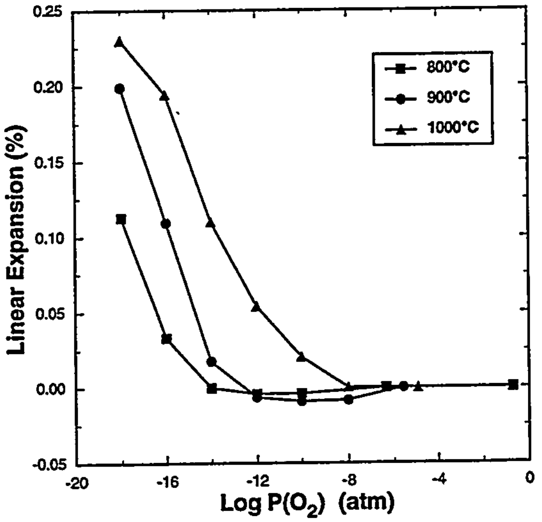

Figure 8. Linear Expansion of LSC-24 as a Function of Temperature and Oxygen Partial Pressure.

close match to YSZ. However, a 15% addition of YSZ to LSM-16 did not improve the match to YSZ but instead resulted in an increased thermal expansion (11.1 x 10^{-6} K^{-1}).

Some SOFC designs require co-sintering of the cathode and YSZ. Successful co-sintering requires a close match in the sintering behavior of both materials. Plots of sintering shrinkage (with and without YSZ additions) as a function of temperature are shown for LSM-16 and LCM-20 in Figures 5 and 6, respectively. The mismatch between the shrinkages of YSZ and the manganites without YSZ additions is apparent. In the case of LSM-16, the addition of 15 vol.% YSZ improved the match to YSZ significantly, except at high temperature (above 1400°C) where there was evidence of swelling of the specimen. Increasing the addition to 50 vol.% had little further effect on the shrinkage behavior. For LCM-20, the match was improved slightly by the YSZ additions. At high temperatures, substantial swelling was observed in the YSZ/LCM specimens; swelling also occurred to a lesser degree in the YSM/LSM specimens. This swelling may occur as a result of oxygen evolution from the perovskite lattice at elevated temperatures. If the specimen has sintered sufficiently to close off the internal pores from the surface, oxygen leaving the lattice will be trapped within the bulk of the specimen and may cause bloating. This mechanism may explain the low densities observed for the YSZ/manganite mixtures sintered at high temperatures (Figures 3 and 4).

The sintering behavior of doped lanthanum manganite and yttrium manganite was determined to be highly sensitive to changes in the A/B cation ratio. Manganites synthesized with a deficiency of A-site cations exhibited enhanced densification behavior relative to B-site cation deficient manganites. Maximum sintered densities of mixtures of lanthanum manganite and YSZ were obtained by sintering at 1300°C. Higher sintering temperatures resulted in lower densities. The addition of YSZ to the manganites resulted in reduced electrical conductivity but allowed for tailoring of the thermal expansion and sintering shrinkage. Small quantities of $La_2Zr_2O_7$ were formed during sintering of mixtures of YSZ and slightly A cation deficient manganites (i.e., A/B = 0.98). The formation of $La_2Zr_2O_7$ during sintering was suppressed in mixtures of YSZ and Mn-enriched manganites (A/B = 0.91). Thus, judicious selection of the A/B cation ratio and amount of YSZ addition may result in SOFC cathodes with adequate electrical conductivity, thermal expansion and sintering shrinkage matched to the YSZ electrolyte, and minimal deleterious interaction with the YSZ.

STABILITY OF LANTHANUM CHROMITE IN REDUCING ENVIRONMENTS

$(La_{1-x}Sr_x)CrO_3$ and $(La_{1-x}Ca_x)CrO_3$ powders, where x was varied from 0.1 to 0.4, were synthesized using the glycine-nitrate process[7]. All powders synthesized for this study had an A/B cation ratio equal to unity. The powders were precalcined at 650°C for 0.5 hour to decompose any residual organic material and then calcined at 1000°C for 1 hour. The powders were uniaxially pressed into bars at 55 MPa followed by isostatic pressing at 138 MPa for dilatometric studies. Samples were sintered in air at 1500° to 1650°C for 5 hours. Additional samples were prepared with the general formula $La_{0.7}Ca_{0.3}(Cr_{0.9}M_{0.1})O_3$ (where M was Ti, Co, Fe, Ni, Zn, Ga, Al, Mn or Cu) to evaluate the effects of isovalent and aliovalent B-site dopants on the dimensional stability.

The dependence of the physical properties of sintered lanthanum chromites upon ambient oxygen partial pressure and temperature (using electrical conductivity, dilatometry, thermogravimetric analysis, and oxygen permeation measurements) were studied. $La_{1-x}A_xCrO_3$ and $Y_{1-x}Ca_xCrO_3$, where A is Ca or Sr and x was varied from 0.1 to 0.4 were evaluated in this study. The oxygen partial pressure was varied using a CO_2 buffered Ar - 4%H_2 gas system, enabling expansion measurements to be made over a partial pressure range from 10^{-5} to 10^{-18} atmosphere at 800, 900, and 1000°C

Figure 7 is a plot of the isothermal linear expansion of $La_{1-x}Sr_xCrO_3$ where x was varied from 0.15 to 0.5 as a function of the oxygen partial pressure at 1000°C. All samples evaluated showed no effect of reducing environment from ambient pressure to 10^{-8} atmosphere. As the P(O2) was lowered further, the samples steadily expanded. The critical oxygen partial pressure (onset of expansion) was the same for all samples 10^{-10} atm. The data further show that the expansion increases with increasing acceptor dopant concentration. Similar results were observed for the $La_{1-x}Ca_xCrO_3$ and $Y_{1-x}Ca_xCrO_3$ systems, however, the magnitude of the expansion varies slightly.

Figure 8 shows the effect of decreasing $P(O_2)$ on the linear expansion of LSC-24 as a function of temperature. This sample showed no effect of reducing environment from ambient pressure to 10^{-8} atmosphere at 1000°C. As the $P(O_2)$ was lowered further, the sample steadily expanded, reaching a maximum expansion of ≈0.23% at 10^{-18}

atmospheres. Figure 8 also clearly shows that the onset (critical oxygen partial pressure) of expansion moved towards lower oxygen partial pressures with decreasing temperature. Both figures 7 and 8 indicate that the magnitude of expansion decreases with decreasing temperature.

Acceptor doping of lanthanum chromite (substitution of Sr or Ca for La) can be charge compensated either electronically (through the conversion of Cr^{3+} to Cr^{4+}) or ionically (through the creation of oxygen vacancies), as shown by the electroneutrality relation in Equation 1 (Kroger-Vink notation; brackets denote concentration).

$$[Sr_{La}^{'}] = [Cr_{Cr}^{\bullet}] + 2[V_O^{\bullet\bullet}] \tag{1}$$

At high oxygen partial pressures, this compensation is electronic, as verified experimentally in a study by Pederson and Dake using XPS[8] in which the Cr^{4+} concentration was found to be equivalent to the A-site acceptor concentration. At low oxygen partial pressures, charge compensation is dominated by the formation of oxygen vacancies, as shown in Equation 2.

$$La_{1-x}^{x}M_{x}^{'}Cr_{1-x}^{x}Cr_{x}^{\bullet}O_{3}^{x} \rightarrow La_{1-x}^{x}M_{x}^{'}Cr_{1-x+2\delta}^{x}Cr_{x-2\delta}^{\bullet}O_{3-\delta}^{x}[V_{O}^{\bullet\bullet}]_{\delta} + \frac{\delta}{2}O_2 \tag{2}$$

TGA analysis on these samples by the authors has verified an appreciable decrease in mass due to oxygen evolution during reduction[9]. The weight loss (vacancy formation) and gain due to oxygen removal and uptake from the lattice correspond well with the observed reversible linear expansion as well as with electrical conductivity measurements carried out by others[10,11]. Based on this information, it would be expected that increasing the acceptor concentration in lanthanum chromites would result in increased expansion upon reduction as the higher initial concentration of Cr^{4+} is reduced to Cr^{3+}, resulting in an increased concentration of oxygen vacancies in the lattice.

The removal of oxygen from the perovskite lattice results in an increase in lattice cell dimensions, and, therefore, an increase in specimen volume as indicated by Srilomsak et al.[12] and Armstrong et al.[9]. The observed expansion may result from the increase in cation size accompanying the reduction of Cr^{4+} to Cr^{3+} and/or an electrostatic repulsive forces

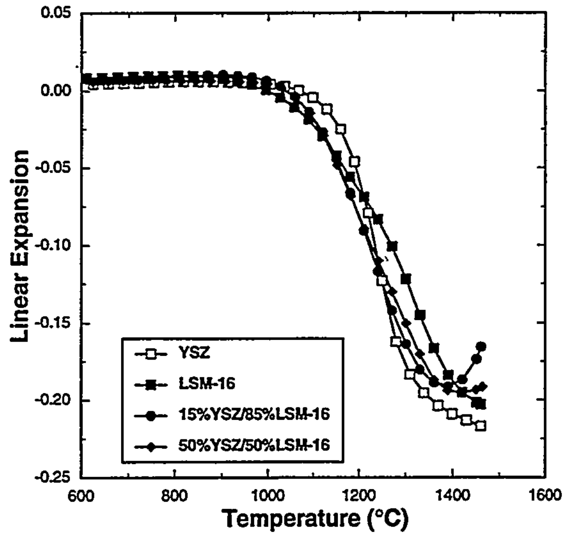

Figure 5. Sintering shrinkage plots for LSM-16/YSZ mixtures. Specimens heated at 2°C/min in air.

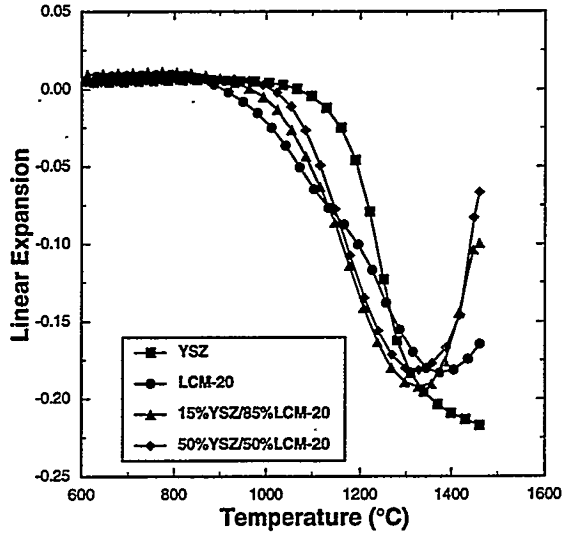

Figure 6. Sintering shrinkage plots for LCM-20/YSZ mixtures. Specimens heated at 2°C/min in air.

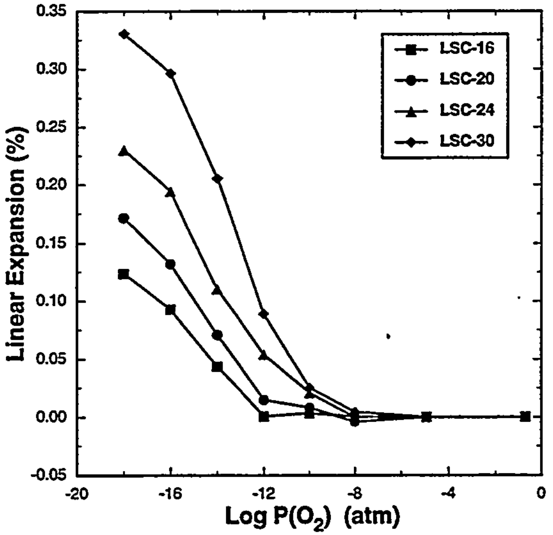

Figure 7. Linear Expansion of $La_{1-x}Sr_xCrO_3$ as a Function of Oxygen Partial Pressure at 1000°C.

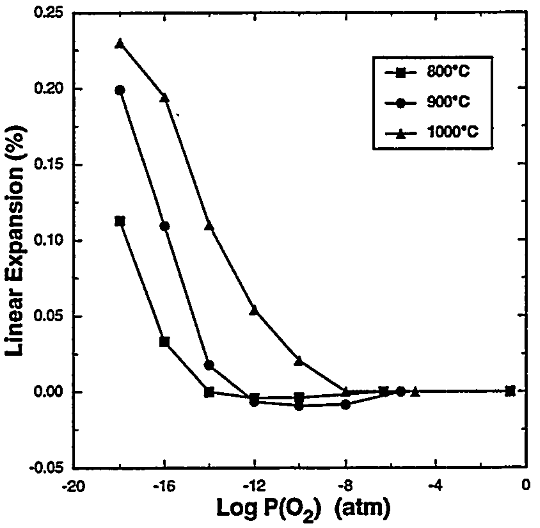

Figure 8. Linear Expansion of LSC-24 as a Function of Temperature and Oxygen Partial Pressure.

between adjacent Cr cations separated by oxygen vacancies.

Figure 9 shows data for linear expansion as a function of dopant content from this study and from Schafer and Schmidberger[13] in 10^{-15} atm $P(O_2)$ at 1000•C. In both studies, it is apparent that the relationship between expansion and dopant content was approximately linear over a wide range of composition. The relationship between sample expansion and dopant concentration (denoted by the slope) is 0.013% expansion/mole % dopant for LSC and 0.015% expansion /mole% dopant for LCC materials. It is clear, however, (from the fact that the linear fits shown in Figure 9 have negative y-intercepts) that this linearity cannot hold for very low dopant levels. The data presented in Figure 9 show very good agreement over the entire composition range for the LSC materials. However, there is a large disparity between the expansion measurements for the two sets of LCC data presented in this figure. The data presented by the authors are similar to that of LSC. The data by Schafer and Schmidberger[13] show a significant deviation. While still linear, their data shows nearly a 1:1 correlation between the expansion and the Ca concentration. The data of Schafer more closely match the expansion data at 10^{-18} atmospheres obtained in the present investigation.

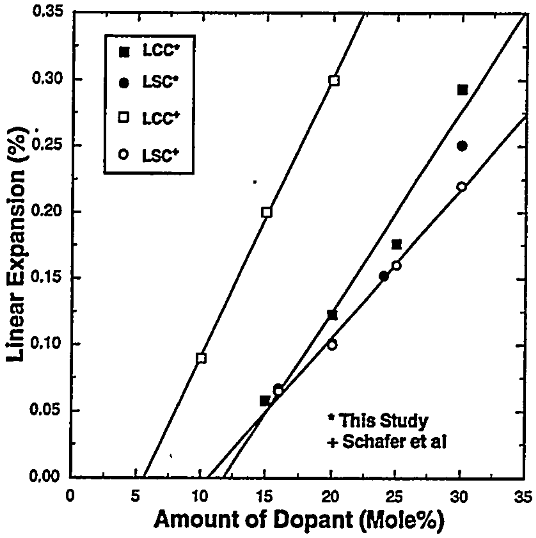

Figure 9. Maximum Linear Expansion at 10-15 atm (1000°C) for LSC and LCC compared to Similar Data From Ref. 13.

REFERENCES

1. B.C. Tofield and W.R. Scott, J. Solid State Chem., **10**, 183 (1974).

2. J.W. Stevenson, M.M. Nasrallah, H.U. Anderson, and D.M. Sparlin, J. Solid State Chem., **102**, 175 (1993).

3. J.W. Stevenson, P.F. Hallman, T.R. Armstrong, and L.A. Chick, Accepted J. Am. Ceram. Soc.**78** [3] 507 (1995)

4. J.A.M. van Roosmalen, E.H.P Cordfunke, and J.P.P. Huijsmans, Solid State Ionics, **66**, 285 (1993).

5. M. Aizawa, H. Nishiyama, A. Ueno, M. Kuroishi, S. Yoshino, K. Eguchi, and H. Arai, Proc. 36th Int. SAMPE Symp., p. 1231 (1991).

6. S. Srilomsak, D.P. Schilling, and H.U. Anderson, in 1st Intl. Symp. on SOFC/1989,
S.C. Singhal, Editor, PV 89-11, p.129, The Electrochemical Society Proceedings Series, Pennington, NJ (1989).

7. L. A. Chick, L. R. Pederson, G. D. Maupin, J. L. Bates, L. E. Thomas, and G. J. Exarhos, Mater. Lett., **10**, 6 (1990).

8. L. R. Pederson and L. S. Dake, in Ceramic Transactions, 5, Advanced Characterization Techniques for Ceramics, ed. by W. S. Young, G. L. McVay and G. E. Pike (1988).

9. T. R. Armstrong, J. W. Stevenson, P. E. Raney, and L. R. Pederson, 1994 Fuel Cell Seminar Abstracts, p. 105, Courtesy Associates (1994).

10. I. Yasuda and T. Hikita, J. Electrochem. Soc., 140, 1689 (1993).

11. H. U. Anderson, J. H. Kuo, and D. M. Sparlin, in Proceedings of the 1st Int. Symposium on Solid Oxide Fuel Cells, ed. S. C. Singhal, Electrochem. Soc., Pennington, NJ, p. 111 (1989).

12. S. Srilomsak, D. P. Schilling and H. U. Anderson, in Proceedings of the 1st Int. Symposium on Solid Oxide Fuel Cells, ed. S. C. Singhal, Electrochem. Soc., Pennington, NJ, p. 129 (1989).

13. W. Schafer and R. Schmidberger, in High Tech Ceramics, Ed. by P. Vincenzini, Elsevier Science Publishers, p. 1737 (1987).

Ceramic Catalyst Materials

A. G. Sault and T. J. Gardner
Fuel Science Department
Sandia National Laboratories
Albuquerque, NM 87185-0710

A. Hanprasopwattanna, J. Reardon, and A. K. Datye
Department of Chemical and Nuclear Engineering
University of New Mexico
Albuquerque, NM 87131

ABSTRACT

Hydrous titanium oxide (HTO) ion-exchange materials show great potential as ceramic catalyst supports due to an inherently high ion-exchange capacity which allows facile loading of catalytically active transition metal ions, and an ability to be cast as thin films on virtually any substrate. The ion-exchange capacity arises from the inclusion of sodium ions within the titania matrix during synthesis. Thin film forms of titania and HTO materials possess several advantages over the bulk oxide forms for catalyst support applications. By coating titania and HTO materials onto inexpensive, high surface area substrates such as silica and alumina, the economics of using these materials is greatly improved, particularly for the HTO materials, which are substantially more expensive in the bulk form than other oxide supports. In addition, the development of thin film forms of these materials allows the catalytic and mechanical properties of the final catalyst formulation to be separately engineered. In order to fully realize the potential of thin film forms of titania and HTO, improved methods for the deposition and characterization of titania and HTO films on high surface area substrates are being developed. By varying deposition procedures, titania film thickness and substrate coverage can be varied from the submonolayer range to multilayer thicknesses on both silica and alumina. HTO films can also be formed, but the quality and reproducibility of these films is not nearly as good as for pure titania films. The films are characterized using a combination of isopropanol dehydration rate measurements, point of zero charge (PZC) measurements, BET surface area, transmission electron microscopy (TEM), and elemental analysis. In order to assess the effects of changes in film morphology on catalytic activity, the films are being loaded with MoO_3 using either incipient wetness impregnation or ion-exchange of heptamolybdate anions followed by calcining. The MoO_3 is then sulfided to form MoS_2, and tested for catalytic activity using pyrene hydrogenation and dibenzothiophene (DBT) desulfurization, model reactions that simulate reactions occurring during coal liquefaction. Comparison with bulk titania and HTO supports, as well as uncoated silica and alumina, demonstrates the superiority of the thin film materials as supports for MoS_2 catalysts. In addition to use as supports for MoS_2 catalysts, the thin film materials are also being investigated as supports for rhodium catalysts for alkane hydrogenolysis, and iron catalysts for selective dehydrogenation. Results of catalytic activity measurements are being correlated with characterization results to determine the influence of changes in film properties on catalyst activity.

INTRODUCTION

The use of thin film materials as catalysts for coal liquefaction and related reactions provides several potentially important advantages over conventional catalyst technology. First, the use of thin films deposited on inexpensive high surface area substrates allows the use of relatively expensive catalytic materials in a cost effective manner. Many potentially useful catalytic materials are too expensive to be used in a bulk form, but become economical in thin film form due to lower raw materials costs. Second, the ability to tailor the catalytic properties of thin film materials independently of the physical properties of the support increases catalyst design flexibility. Changes can be made in catalytic properties without changing physical factors that affect reactant and product diffusion within catalyst particles. Third, thin film technology allows the use of materials with advantageous catalytic properties that lack the structural strength needed in commercial applications. By coating a structurally weak material onto a much stronger substrate, catalysts can be designed that incorporate previously unusable catalytic functions while maintaining the mechanical strength needed to withstand the physical demands encountered in commercial catalytic reactors. Fourth, the properties of thin film materials may differ in important ways from the corresponding bulk materials. Thus, thin film catalyst materials offer the potential to access new catalytic behaviors unattainable with bulk materials.

Two materials that could benefit from development of thin film forms are titania and hydrous titanium oxide (HTO) ion exchange materials. Titania-supported catalysts often show significantly different catalytic behavior than silica or alumina supported catalysts, but the surface areas of bulk titania materials are generally inferior to those obtainable with silica or alumina. Thus, development of titania thin film technology would allow application of the catalytic properties of titania supports without the disadvantage of low surface area. HTO materials are formed by the reaction of a metal alkoxide (*e.g.*, titanium tetraisopropoxide (TTIP)) with a solution of NaOH in a suitable solvent (*e.g.*, methanol or toluene), followed by hydrolysis with an acetone/water mixture.[1] The resulting amorphous powders have surface areas on the order of 300 m^2/g, and contain up to one sodium ion for every two titanium atoms. These sodium ions can be quantitatively exchanged for metal cations in aqueous solution, providing a simple and effective method for preparing supported metal catalysts. With proper control of ion-exchange conditions, high metal loadings can be achieved with essentially atomic dispersion.[2,3] For certain classes of metals, these high dispersions can be retained even after reduction to the metallic state,[4] resulting in extremely efficient usage of expensive noble metals. Furthermore, experimental sulfided NiMo/HTO catalysts exhibit activities for reactions relevant to coal liquefaction exceeding those of currently available commercial catalysts.[1] In spite of these encouraging results, HTO materials suffer from high manufacturing costs and poor mechanical properties . Thus, HTO materials would also benefit greatly from the further development of thin film forms. Within the context of the DOE Fossil Energy Materials Program, the emphasis of this project is to study sulfided NiMo thin film catalysts for coal liquefaction, but it is important to note that the technology resulting from this project has general applicability for a number of diverse catalytic applications. Thus, in addition to studies of sulfided NiMo catalysts supported on thin titania and HTO films, we are also investigating the use of these materials as supports for metal catalysts for hydrogenolysis (cracking) and oxide catalysts for selective dehydrogenation.

DISCUSSION OF CURRENT ACTIVITIES

In previous work,[5] emphasis was placed on the development of deposition techniques for coating nonporous silica spheres with titania and HTO films. We have now extended these studies to high surface area silica and alumina materials. Substantial effort is also being devoted to loading these films with MoS_2 and testing the resulting materials for hydrodesulfurization (HDS) of DBT. This model reaction is highly relevant to direct coal liquefaction, since heteroatom removal is an important step in the liquefaction process.

Titania Thin Film Characterization

The use of specific rates of isopropanol dehydration to measure titania surface areas on silica has been developed as part of this program. Because titania is several orders of magnitude more active for isopropanol dehydration than silica, the rate of isopropanol dehydration over titania coated silica materials can be used to calculate the titania surface area alone. Calibration of the technique is provided by measurement of the reaction rate on bulk titania materials with known BET surface area. While the basic technique is well established, several outstanding issues with regard to this measurement have been addressed and resolved within the past year. The first issue regards the effects of impurities on the measured rates. It is well known that sodium is a strong poison for dehydration catalysts. Because many high surface area silica materials contain sodium as an impurity, sodium must be removed by acid treatments prior to application of the titania coating and measurement of dehydration rates. Even though silica itself is inactive for dehydration, it is apparent from studies of films prepared on washed (low Na) and unwashed (high Na) silica that sodium can migrate from the silica onto the titania film and thereby poison activity, resulting in artificially low activities and an underestimation of titania surface areas.

A second issue involves the effect of pretreatment on specific dehydration activities of titania coatings. For virtually all films studied, dehydration rates over untreated films correspond to titania surface areas that exceed the BET surface area of the material as a whole. Clearly, specific dehydration rates over the untreated films must be substantially higher than over the bulk titania materials used for calibration. After pretreating the titania films in flowing helium at 500°C, titania surface areas measured by dehydration are always equal to or lower than the total BET surface area. In cases where the two techniques agree, the entire silica surface must be covered by titania. In cases where the titania surface area is less than the total, only partial coverage has been obtained. These pretreatment studies clearly show that the use of bulk titania materials to calibrate specific rates of isopropanol dehydration is valid only for films pretreated at 500°C or higher, and that films treated at lower temperatures have a very different surface structure and specific activity than the bulk materials.

Both sodium content and pretreatment affect the specific activity of HTO materials as well. Acidification of HTO materials to remove sodium is facile compared to removal of sodium from silica, since sodium ions present in HTO are designed to be easily ion-exchangeable. The question of pretreatment and correspondence between the specific activity of bulk standards and thin film materials remains problematic, however. Comparisons among the activities of three bulk HTO samples pretreated at different temperatures demonstrate the difficulties involved. As the pretreatment temperature rises from 300°C to 500°C, the BET surface area drops from 321 m^2/g to 107 m^2/g, and the specific dehydration rate falls from 9.8×10^{-8} $moles/m^2/s$ to 1.6×10^{-6} $moles/m^2/s$. A change in surface structure must accompany the loss in surface area and result in the observed drop in specific activity. Even after accounting for the effects of pretreatment temperature, the use of bulk HTO standards to calibrate HTO film surface area measurements is currently unsatisfactory. For pretreatment at either 400 or 500°C, HTO film surface areas derived from isopropanol dehydration exceed the total BET surface areas by 50-100%. This result indicates that under the pretreatment conditions attempted to date, the structure of the thin film HTO materials does not correspond to that of the bulk HTO materials. While this result currently precludes the use of isopropanol dehydration for measurement of HTO film surface areas, it does provide an important indication that HTO films may be fundamentally different from the bulk materials. Further work is in progress to resolve this issue.

A final issue with regard to the use of isopropanol dehydration to measure titania surface area arises in the extension of this technique to alumina substrates. While α-Al_2O_3 is inactive for dehydration reactions,[6] and therefore amenable to the isopropanol dehydration method for determining titania film surface area, it is available only with very low surface areas (~10 m^2/g). γ-Al_2O_3 is available with higher surface areas, and is therefore more desirable as a film substrate material, but suffers from the drawback of possessing a high dehydration activity.[6] Consequently, the dehydration reaction cannot differentiate between surface area due to titania and surface area of the γ-Al_2O_3 substrate. For this reason, we investigated a different method for determining film surface area, based on measurement of the point of zero charge (PZC).[7] PZC can be determined either by measuring the mobility of suspended solid particles under the influence of an applied electric field, or by measuring the asymptotic pH obtained in a suspension of the solid as the concentration of solid becomes large. Since different materials have different PZC's, is has been asserted that the PZC of a mixture of solids varies linearly with the fractional surface area of each phase.[7] This method has been tested for physical mixtures of titania and silica and a linear relationship is found (figure 1). Using this relationship as a calibration,

Figure 1: Point of Zero Charge Calibration Curve

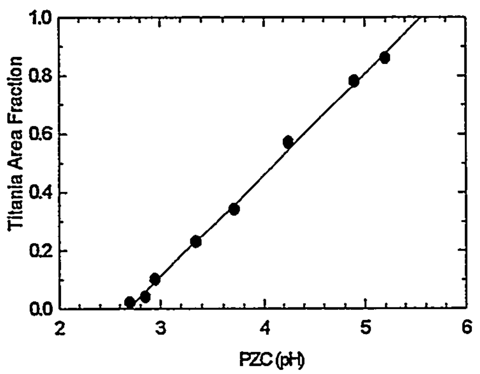

the PZC method was used to measure the titania surface area of titania coated silica materials, and compared to the results of isopropanol dehydration. The comparison gives fair agreement (±20%) between the two techniques, and provides confidence that the PZC method is valid for thin films, as well as physical mixtures of two components.

Titania Thin Film Formation and Characterization on Silica

In the past, much effort was dedicated to the growth of monolayer and multilayer films on nonporous silica spheres. These spheres present several advantages over high surface area silica, including ease of characterization by TEM and an absence of problems related to diffusion limitations during dehydration activity measurements, but suffer from the disadvantage that they have low surface areas (12 m^2/g) and are therefore not practical for industrial application. In the past year we have completed work on titania films on the spheres, and extended this work to high surface area silica gels using the knowledge gained with the spheres to guide our efforts.

Multilayer films of titania on silica spheres have been prepared and total and specific surface areas measured. These films are prepared by careful addition of controlled amounts of water to a solution of titanium *t*-butoxide (TBOT) in ethanol, followed by addition of silica spheres and refluxing of the mixture at the boiling point of ethanol. After refluxing, the spheres are filtered, washed with ethanol, and dried under vacuum. As reported in a previous annual report,[5] the multilayer films are clearly visible as 2-10 nm layers in TEM images, and appear uniform, smooth and dense. In spite of this appearance, isopropanol dehydration and total BET surface area measurements show that the surface area of the films can be up to six times greater than that of the uncoated silica spheres (70 m^2/g *vs.* 12 m^2/g). Furthermore, the multilayer film surface areas decrease with pretreatment temperature, but in the best case, the surface area after pretreatment at 500°C remains four times greater than that of the uncoated spheres. This surface area undoubtedly arises from cracking or porosity in the films, as TEM indicates that surface roughness is insufficient to account for the surface area.

Attempts to coat high surface area silica gels with multilayer titania coatings using the technique developed for silica spheres met with little success. Apparently the sensitivity of TBOT to hydrolysis in the presence of water results in some minor precipitation of titania, which, while insufficient to negatively impact film growth on spheres, blocks pore entrances in high surface area silicas and prevents multilayer formation. In an attempt to avoid this problem, we are investigating the use of water soluble precursors, such as the lactamide complex $[CH_3CH(O)CO_2NH_2]_2Ti(OH)_2$. A silica gel with a surface area of 159 m^2/g was dispersed in an aqueous solution of the lactamide precursor, with urea added to induce precipitation, and the mixture was then refluxed for 20 hours. After filtering, washing with water, drying, and calcining at 550°C for 16 hours, the resulting material contained 39 wt% titania, and possessed a surface area of 350 m^2/g as measured by both

BET and isopropanol dehydration. Thus, the surface area of the material was effectively doubled by the addition of the titania coating, and the entire silica surface was coated. TEM images (figure 2) of this sample show the amorphous silica matrix, as well as the presence of 2-4 nm anatase crystallites dispersed throughout the material. The presence of these crystallites is consistent with the increased surface area.

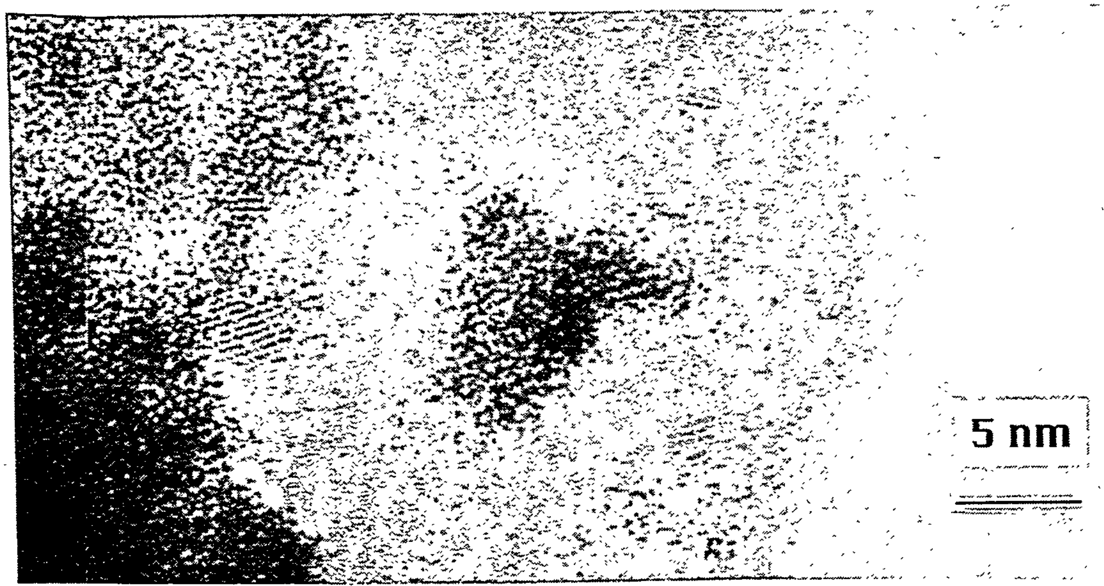

Figure 2: TEM Image of Silica Gel Coated with 39 wt% Titania Film

HTO Thin Film Formation and Characterization on Silica

HTO coatings cannot be formed by the same process used for titania films since the hydrolysis of the titanium precursor is much faster in the presence of NaOH, and refluxing a mixture of the HTO precursor solution with silica spheres results in heterogeneous precipitation of bulk HTO particles and very poor film qualities. The best HTO films are formed by filtering the HTO precursor through the silica spheres, and then washing the spheres with hexane and water to complete the hydrolysis. This procedure results in submonolayer coverages of the HTO film on the silica spheres as measured by isopropanol dehydration, and TEM shows the films to be much rougher than titania films. These submonolayer HTO films are now being used to sort out differences in Rh^{3+} ion-exchange behavior between bulk and thin film HTO materials, and also to investigate how changes in rhodium ion-exchange parameters affect the rhodium loading, distribution, and hydrogenolysis activity. Although not important from the aspect of developing improved coal liquefaction catalysts, experiments with noble metals are important for determining the generic applicability of HTO thin films as catalysts supports.

Like the submonolayer coatings, multilayer coatings of HTO films also require substantially different deposition techniques than multilayer titania coatings. Addition of water to the precursor mixture is not effective since the accelerated hydrolysis of the HTO precursor relative to TBOT results in precipitation of bulk HTO. Instead, an attempt was made to achieve multilayer HTO coatings by using multiple deposition steps. Accordingly, the procedure outlined above for producing submonolayer coatings was repeated a total of four times, and the resulting materials were dried overnight at 110°C. BET measurements of silica spheres coated in this manner show a substantial increase in total surface area, but until TEM measurements are made, we cannot be sure that this increase is the result of a high surface area coating, rather than the presence of some precipitated bulk HTO material. An HTO coating prepared in this manner on a high surface area silica gel shows no change in BET surface area, indicating that at most a monolayer film was formed. Because of the difficulties described earlier with using the isopropanol dehydration rate to measure HTO surface area, we are currently unable to distinguish between monolayer and submonolayer HTO coatings, but anticipate that analysis of these films by TEM will help to clarify this question.

Titania Thin Film Formation on Alumina

In addition to our work with silica substrates, we have also directed effort toward developing coating techniques for alumina substrates. Monolayer films have been formed on a low surface area α-alumina using methods similar to those developed for silica substrates. The films do not alter the BET surface area of the substrate, and calculations based on bulk titania content indicate that the amount of titania present is adequate to form a complete a monolayer. These films do not alter the appearance of the substrate as viewed by TEM, indicating the absence of any agglomeration or particle formation. PZC and isopropanol dehydration measurements are underway to further characterize the films, and studies on higher surface aluminas are planned for the coming year.

MoS_2 Formation and Hydrodesulfurization Activity on Titania Thin Films

Titania films on both silica and α-alumina substrates have been loaded with molybdenum using incipient wetness techniques, calcined at 500°C, and sulfided at 400°C in a 10% H_2S in hydrogen mixture to produce MoS_2 particles. For comparison, uncoated substrates have also been prepared with similar MoS_2 loadings. TEM analysis has been performed on both the alumina and silica substrates and testing for HDS activity has been performed on the silica substrate materials. TEM of coated (17 wt% TiO_2) and uncoated silica containing ~6 wt% MoS_2 (figure 3) shows important differences between the morphologies of the MoS_2 particles in the two cases. On pure silica multilayered MoS_2 structures are visible, while on the titania coated silica MoS_2 tends to form mostly single layer structures. Furthermore, the MoS_2 particles in the coated sample tend to be associated with the small crystalline titania particles rather than with the silica support.

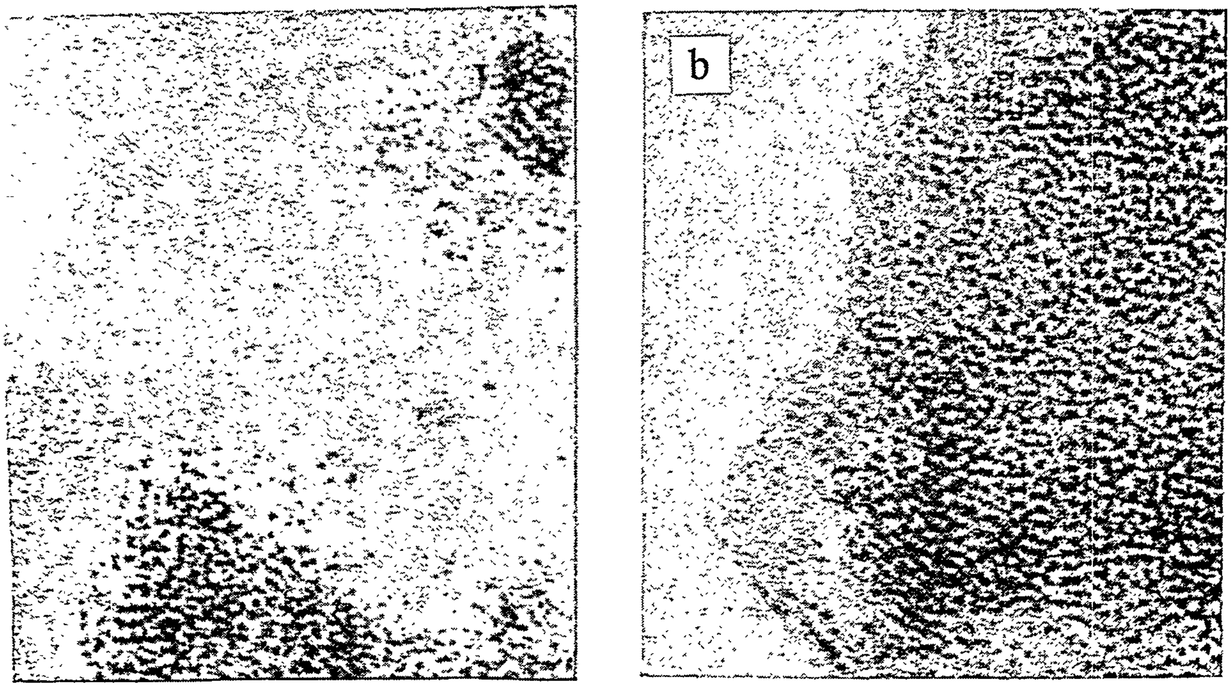

Figure 3: TEM Images of a) 6 wt% MoS_2 on Silica and b) 6 wt% MoS_2 on Titania Coated Silica.

Batch HDS activity measurements on the coated and uncoated silica materials show that the catalytic activity reflects the differences in MoS_2 morphology (Table I). For the same MoS_2 loading, the activity of the titania coated silica is approximately 7 times greater than that of the uncoated silica. Either the single layer structures are inherently more active than multilayered structures, or the formation of single layers increases the fraction of molybdenum atoms located on particle edges, which are widely believed to be the active sites in this class of catalysts. Note also that the as the MoS_2 loading increases on the titania coated materials, the

Table I

Batch HDS activity of supported MoS_2 Catalysts

350°C, 1200 psig H_2, 50 mg catalyst, 100 mg DBT in 1000 mg hexadecane (solvent)

Sample	Psuedo-First Order Rate Constant (moles DBT/mole Mo/s)
6 wt% MoS_2/SiO_2	0.87
6 wt% MoS_2/17 wt% TiO_2/SiO_2	6.13
12 wt% MoS_2/17 wt% TiO_2/SiO_2	5.68
18 wt% MoS_2/17 wt% TiO_2/SiO_2	2.39

activity per molybdenum atom declines. This decrease is expected since the weight loading at which the amount of MoS_2 exceeds the monolayer capacity of the support is near 10-12 wt%. Above this loading, multilayer structures must necessarily form, and the apparent advantages of single layer particles are lost. At the time of writing, TEM images of the higher weight loading materials were unavailable, but it is anticipated that these images will show an increase in the number of multilayer particles as the loading increases.

Although activity testing for the coated alumina particles is not yet complete, TEM images of these materials provide some information and allow the prediction of catalytic behavior. Upon initial inspection, TEM images of α-alumina loaded with an amount of molybdenum equivalent to a ~1.7 layers of MoS_2 give little evidence for an effect of the titania monolayer (figure 4). Upon closer examination, however, the MoS_2 particles on the uncoated alumina appear to consist of extended single layers of MoS_2 exposing few edge sites. On the alumina coated with a monolayer of titania, the surface appears much rougher than the uncoated alumina, and the MoS_2 particles appear much less continuous, and therefore likely to expose a higher fraction of molybdenum at the active edge sites. For this reason it is anticipated that the titania coated material will show superior activity to the uncoated alumina.

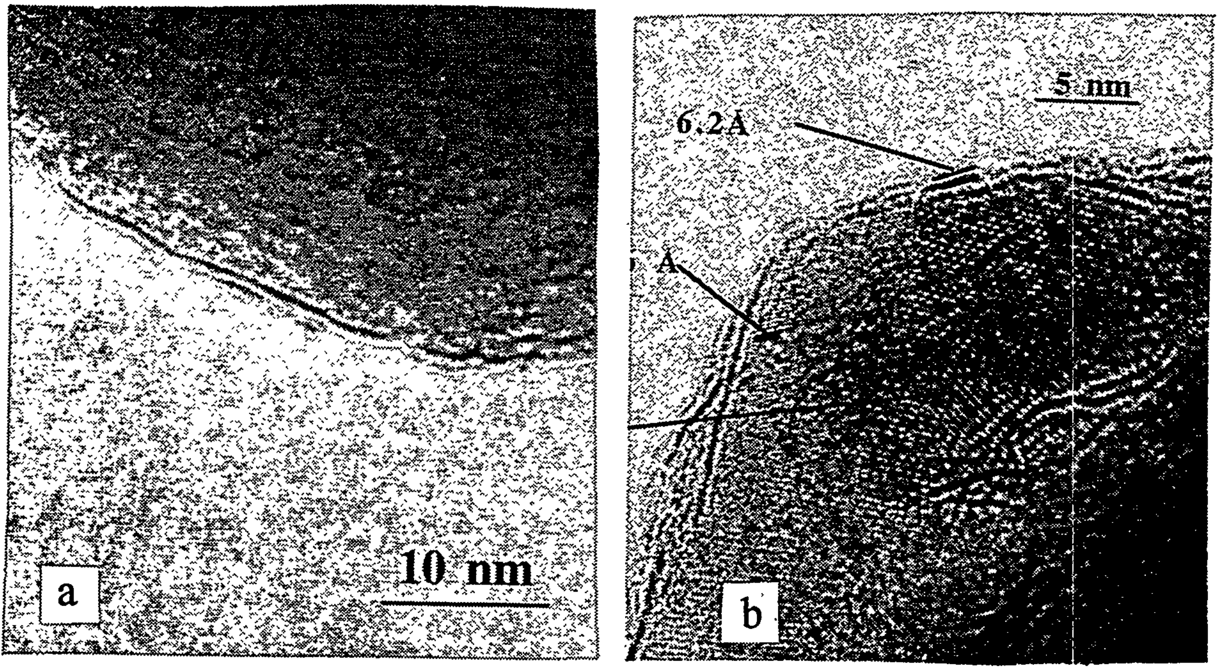

Figure 4 - TEM images of a) MoS_2 on α-Alumina and b) MoS_2 on Titania Coated α-Alumina.

CONCLUSIONS

Substantial progress has been made in the development of thin film deposition techniques for forming titania and HTO films on silica and alumina substrates. On nonporous silica spheres monolayer and multilayer titania coatings can be formed with surface areas exceeding those of the substrate. On high surface area silica gels, multilayer coatings have also been formed using a water soluble titania precursor. Titania film deposition on alumina substrates is also under investigation, and initial results suggest that techniques developed for silica substrates will be effective with alumina substrates as well. MoS_2 particles have been formed on both coated and uncoated silica and alumina substrates, analyzed by TEM, and tested for HDS catalytic activity. Although testing is still underway, TEM results show clear differences between MoS_2 particles supported on coated and uncoated substrates. These morphological differences are reflected in the catalytic activity of the materials, with the coated materials showing superior activity.

Substantial progress has also been made in the development of thin film deposition techniques for the HTO system. Results to date show that substantial coverages of HTO materials can be achieved on both silica spheres and high surface area silica gels. The ion-exchange and catalytic behavior of these films is under investigation. In addition to their utility as MoS_2 catalyst supports for direct coal liquefaction, these materials also offer significant advantages as supports for a diverse range of catalytic applications, including hydrogenolysis and selective dehydrogenation. In addition to evaluation of HTO thin film materials as supports for coal liquefaction catalysts, we are therefore also exploring the generic applicability of HTO thin film technology by evaluating these materials for both hydrogenolysis and selective dehydrogenation.

REFERENCES

1. (a) R. G. Dosch, H. P. Stephens, F. V. Stohl, B. C. Bunker, and C. H. F. Peden, "Hydrous Metal Oxide-Supported Catalysts: Part I. Preparation and Physical and Chemical Properties," *Sandia Report* (SAND89-2399). (b) R. G. Dosch, H. P. Stephens, and F. V. Stohl, "Hydrous Metal Oxide-Supported Catalysts: Part II. Catalytic Properties and Applications," *Sandia Report* (SAND89-2400). (c) R. G. Dosch and L. I. McLaughlin, "Hydrous Metal Oxide-Supported Catalysts: Part III. Development of NiMoHMO Catalysts," *Sandia Report* (SAND92-0388).

2. S. L. Anderson, A. K. Datye, E. J. Braunschweig, and C. H. F. Peden, *Appl. Catal.*, 82 (1992)185.

3. T. J. Gardner, C. H. F. Peden, and A. K. Datye, *Catal. Lett.*, 15 (1992) 111.

4. A. G. Sault, *J. Catal.*, in press.

5. A. G. Sault, T. J. Gardner, S. Srinivasan, A. Hanprasopwattanna, and A. K. Datye, in Proceedings of the Eighth Annual Conference on Fossil Energy Materials, Department of Energy, Oak Ridge, TN, May, 1994, p.145.

6. C. R. Narayanan, S. Srinivasan, A. K. Datye, R. Gorte, and S. Biaglow, *J. Catal.*, 138 (1992) 659.

7. S. Subramanian, J. S. Noh, and J. A. Schwartz, *J. Catal.*, 114(1988) 433.

APPENDIX A

FINAL PROGRAM
FOR THE NINTH ANNUAL
CONFERENCE ON FOSSIL ENERGY MATERIALS

FINAL PROGRAM
CONFERENCE ON FOSSIL ENERGY MATERIALS
Oak Ridge, Tennessee
May 16-18, 1995

SESSION I - Ceramic Composites

Tuesday, May 16, 1995

7:00 a.m. Registration and Refreshments

8:00 *Welcome and Introductory Remarks,* Program Managers, Department of Energy and Oak Ridge National Laboratory

8:10 *Keynote Address* - Dr. John Longwell, Chairman of the Committee on the Strategic Assessment of the U.S. Department of Energy's Coal Program

9:00 *AR&TD Materials Program Overview* - James P. Carr, DOE/HQ Program Manager

9:30 *Oxidation-Resistant Interfacial Coatings for Continuous Fiber Ceramic Composites,* D. P. Stinton, Oak Ridge National Laboratory

9:55 *Modeling of Fibrous Preforms for CVI Fabrication,* T. L. Starr, Georgia Institute of Technology

10:20 **BREAK**

10:45 *Engineering Scale Development of the Vapor-Liquid-Solid (VLS) Process for the Production of Silicon Carbide Fibrils and Linear Fibril Assemblies,* M. A. Tenhover, The Carborundum Company and F. Ko, APD Inc.

11:10 *Mechanical Properties of Ceramic Composite Tubes,* W. A. Curtin, Virginia Polytechnic Institute and State University

11:35 *Joining of SiC Ceramics and SiC/SiC Composites,* B. H. Rabin, Idaho National Engineering Laboratory

12:00 *Comparison of High Temperature Mechanical Properties of Two Monolithic SiC Ceramics and an* Al_2O_3 *SiC Composite,* K. Breder, Oak Ridge National Laboratory

12:25 **LUNCH**

1:45 *Factors Effecting the Corrosion Rates of Ceramics in Coal Combustion Systems,* J. P. Hurley, University of North Dakota

2:10 *Corrosion Performance of Materials for Advanced Combustion Systems,* K. Natesan, Argonne National Laboratory

2:35 *Mullite Coatings for Corrosion Protection of Silicon Carbide,* V. Sarin, Boston University

3:00 *Mechanical Behavior of Ceramic Composite Hot-Gas Filters After Exposure to Severe Environments,* D. J. Pysher, 3M Company

3:25 **BREAK**

3:50 *Fracture Behavior of Advanced Ceramic Hot-Gas Filters,* J. P. Singh, Argonne National Laboratory

4:15 *High Temperature Corrosion of Advanced Ceramics Material for Hot-Gas Filters and Heat Exchangers,* R. E. Tressler, Pennsylvania State University

4:40 *Thermal and Structural Analyses of a Filter Vessel Ceramic Tubesheet,* R. H. Mallett, Mallett Technology, Inc.

5:05 *Processing of Nanosize Silicon Nitride and Alumina Powders,* S. G. Malghan, National Institute of Standards and Technology

5:30 **ADJOURN**

FINAL PROGRAM
CONFERENCE ON FOSSIL ENERGY MATERIALS
Oak Ridge, Tennessee
May 16-18, 1995

SESSION II - Ceramics and New Alloys

Tuesday, May 16, 1995
6:30 - 8:30 p.m.

POSTER PRESENTATIONS - BUFFET RECEPTION

Development of Nondestructive Evaluation Methods and Prediction of Effects of Flaws on the Fracture Behavior of Structural Ceramics, W. A. Ellingson and J. P. Singh, Argonne National Laboratory

Fabrication of Fiber-Reinforced Composites by Chemical Vapor Infiltration, D. P. Stinton and W. M. Matlin, Oak Ridge National Laboratory

Transport Properties of Ceramic Composites, T. L. Starr, Georgia Institute of Technology

Development of Materials for Microwave-Heated Diesel Particulate Filter, M. A. Janney, Oak Ridge National Laboratory

High Temperature Inorganic Membranes for Separating Hydrogen, D. E. Fain, Oak Ridge K-25 Site

Mixed Oxygen Ion/Electron-Conducting Ceramics for Oxygen Separation, L. R. Pederson, Pacific Northwest Laboratory

Proton Conducting Cerate Ceramics, L. R. Pederson, Pacific Northwest Laboratory

Synthesis of Silicon Nitride Powders in Pulsed Rf Plasmas, R. J. Buss, Sandia National Laboratories

Mechanically Reliable Surface Oxides for High-Temperature Corrosion Resistance, K. Natesan, Argonne National Laboratory

Plasma Synthesis of Alumina Films on Metal and Ceramic Substrates, I. Brown, Lawrence Berkeley Laboratory

Mechanically Reliable Scales and Coatings, P. F. Tortorelli, Oak Ridge National Laboratory

Welding and Mechanical Properties of Cast FAPY (Fe-16 at. % Al-Based) Alloy Slabs, V. K. Sikka, Oak Ridge National Laboratory

The Influence of Processing on the Microstructure and Properties of Iron Aluminides, R. N. Wright, Idaho National Engineering Laboratory

Weld Overlay Cladding With Iron Aluminides, G. M. Goodwin, Oak Ridge National Laboratory

High-Temperature Corrosion Behavior of Iron-Aluminide Alloys and Coatings, P. F. Tortorelli, Oak Ridge National Laboratory

Effect of Surface Condition on the Aqueous Corrosion Behavior of Iron Aluminides, R. A. Buchanan, University of Tennessee

Pack Cementation Cr-Al Coating of Steels and Ge-Doped Silicide Coating of Cr-Nb Alloy, R. A. Rapp, Ohio State University

Microstructure Characterization and Weldability Evaluation of the Weld Heat Affected Zone (HAZ) in 310HCbN Tubing, C. D. Lundin, University of Tennessee

The Effects of Microstructural Control on the Mechanical Behavior of Cr_2Nb-Based Alloys, P. Liaw, University of Tennessee

SESSION III - WORKSHOP ON MATERIALS CHALLENGES IN ADVANCED FOSSIL FUELED POWER SYSTEMS

Wednesday, May 17, 1995

8:00 - 11:45	**PLENARY SESSION** - Panel Discussion Moderator - Rod Judkins	
	Larry Ruth	Pittsburgh Energy Technology Center; Pittsburgh, Pennsylvania
	Dan Seery	United Technologies Research Center; East Hartford, Connecticut
	Nguyen Minh	AlliedSignal Inc.; Torrance, California
	Tom Gibbons	ABB Combustion Engineering; Windsor, Connecticut
9:45 - 10:00	**BREAK**	
	Ted McMahon	Morgantown Energy Technology Center; Morgantown, West Virginia
	Juhani Isaksson	Ahlstrom Pyropower; Karhula, Finland
	Gerry Bruck	Westinghouse Electric Corporation; Pittsburgh, Pennsylvania
	Mo Bary	Black & Veatch, Overland Park, Kansas
	John Mundy	DOE-Basic Energy Sciences; Washington, DC
11:45 - 1:00	**LUNCH**	
1:00 - 2:30	**SESSION A - HOT GAS FILTERS** Rapporteurs - Dave Stinton and John Hurley	
	SESSION B - METALLIC HEAT EXCHANGERS Rapporteurs - Ian Wright and Ken Natesan	
2:30 - 2:45	**BREAK**	
2:45 - 4:15	**SESSION C - CERAMIC HEAT EXCHANGERS** Rapporteurs - Dave Stinton and Kristin Breder	
	SESSION D - METALLIC COMPONENTS Rapporteurs - Ian Wright and Bob Swindeman	
4:15 - 4:30	**BREAK**	
4:30 - 5:30	**SUMMARY SESSION**	

FINAL PROGRAM
CONFERENCE ON FOSSIL ENERGY MATERIALS
Oak Ridge, Tennessee
May 16-18, 1995

SESSION IV - New Alloys and Functional Materials

Thursday, May 18, 1995

7:30 **Registration Desk Opens**

8:00 Welcome and Introductory Remarks

8:10 *Keynote Address,* Mr. Marvin Singer, DOE/Fossil Energy, Deputy Assistant Secretary for Advanced Research and Special Technologies

8:30 *ODS Iron Aluminides,* I. G. Wright, Oak Ridge National Laboratory

8:55 *Effects of Composition and Heat Treatment at 1150°C on Creep-Rupture Properties of Fe_3Al-Based Alloys,* C. G. McKamey, Oak Ridge National Laboratory

9:20 *Environmental Embrittlement of Iron Aluminides Under Cyclic Loading Conditions,* N. S. Stoloff, Rensselaer Polytechnic Institute

9:45 *The Effect of Alloying and Grain Refinement on the Room-Temperature Ductility of As-Cast Fe_3Al-Based Alloys,* Srinath Viswanathan, Oak Ridge National Laboratory

10:10 **BREAK**

10:30 *Weldability of Polycrystalline Aluminides,* G. R. Edwards, Colorado School of Mines

10:55 *Electro-Spark Deposited Coatings for Protection of Materials,* R. N. Johnson, Pacific Northwest Laboratory

11:20 Overview of BES and FE Joint Project, *Mechanically Reliable Scales and Coatings for High-Temperature Corrosion Resistance,* P. F. Tortorelli, Oak Ridge National Laboratory

11:45 *Cr_2Nb-Based Alloy Development,* C. T. Liu and P. F. Tortorelli, Oak Ridge National Laboratory

12:10 **LUNCH**

1:30 *Investigation of Austenitic Alloys for Advanced Heat Recovery and Hot-Gas Cleanup Systems,* R. W. Swindeman, Oak Ridge National Laboratory

1:55 *Fireside Corrosion Testing of Candidate Superheater Tube Alloys, Coatings, and Claddings - Phase II,* J. L. Blough, Foster Wheeler Development Corporation

2:20 *A Novel Carbon Fiber-Based Porous Carbon Monolith,* T. D. Burchell, Oak Ridge National Laboratory

2:45 *Carbon Fiber Composite Molecular Sieves for Gas Separation,* M. Jagtoyen, University of Kentucky

3:10 **BREAK**

3:30 *Stability of Solid Oxide Fuel Cell Materials,* L. R. Pederson, Pacific Northwest Laboratory

3:55 *Ceramic Catalyst Materials,* A. G. Sault, Sandia National Laboratories

4:20 **ADJOURN**

APPENDIX B

LIST OF ATTENDEES

LIST OF ATTENDEES

Ninth Annual Conference on Fossil Energy Materials
May 16-18, 1995
Oak Ridge, Tennessee

Charles T. Alsup
Morgantown Energy Technology Center
P.O. Box 880
3610 Collins Ferry Road
Morgantown, WV 26505
(304) 285-5432
FAX 304-285-4403

Paul Apen
Los Alamos National Laboratory
MS-D453
Los Alamos, NM 87545
(505) 665-7513
FAX 505-665-2964

Pronob Bardhan
Corning Incorporated
SP-DV-1-9
Corning, NY 14831
(607) 974-3800
FAX 607-974-2171

Mohammad Bary
Black & Veatch
11401 Lamar
Overland Park, KS 66211
(913) 339-7842
FAX 913-339-2934

David Beecy
Department of Energy
Office of Advanced Research
FE-72, B-119
19901 Germantown Road
Germantown, MD 20585
(301) 903-2787
FAX 301-903-8350

T. M. Besmann
Oak Ridge National Laboratory
P.O. Box 2008
MS-6063
Oak Ridge, TN 37831-6063
(615) 574-6852

Nick Biery
University of Tennessee
Department of Materials Science &
Engineering
434 Doughtery Engineering Building
Knoxville, TN 37996-2200
(615) 974-6356
FAX 615-974-4115

Neil Birks
Materials Science & Engineering Department
University of Pittsburgh
848 Benedum Hall
Pittsburgh, PA 15261
(412) 624-9743
FAX 412-624-8069

Norm Bornstein
United Technologies Research Center
411 Silver Lane
East Hartford, CT 06108
(203-727-7487
FAX 203-727-7879

Daniel Boss
BIRL
1801 Maple Avenue
Evanston, IL 60201
(708) 491-3373
FAX 708-467-1022

William H. Boss
University of Tennessee Space Institute
UTSI-MS23
Goethert Parkway
Tullahoma, TN 73788
(615) 393-7414
FAX 615-393-7518

Ron Bradley
Oak Ridge National Laboratory
P.O. Box 2008
Oak Ridge, TN 37831-6067
(615) 574-6094
FAX 615-574-6098

Kristin Breder
Oak Ridge National Laboratory
P.O. Box 2008
Oak Ridge, TN 37831-6062
(615) 574-5089

Ian Brown
Lawrence Berkeley Laboratory
University of California
Berkeley, CA 94720
(510) 486-4174
FAX 510-486-4374

Gerald Bruck
Westinghouse Electric Corporation
Science and Technology Center
1310 Beulah Road
Pittsburgh, PA 15235-5098
(412) 256-2102

R. A. Buchanan
The University of Tennessee
Department of Materials Science
and Engineering
434 Dougherty Engineering Building
Knoxville, TN 37996-2200
(615) 974-4858

Tim Burchell
Oak Ridge National Laboratory
P.O. Box 2008
Oak Ridge, TN 37831-6088
(615) 576-8595

Rick Buss
Sandia National Laboratories
Properties of Organic Materials
Dept. 1812
MS-0367
Albuquerque, NM 87185-0367
(505) 844-3504
FAX 505-844-9624

Jason Canon
Oak Ridge National Laboratory
P.O. Box 2008
Oak Ridge, TN 37831-6062
(615) 574-5089

Gary A. Carlson
Sandia National Laboratories
Department 6211
MS-0710
P.O. Box 5800
Albuquerque, NM 87185-0710
(505)-844-8116
FAX 505-845-9500

J. P. Carr
U.S. Department of Energy
Fossil Energy
Office of Advanced Research
FE-72,
19901 Germantown, MD 20874
(301) 903-6519
FAX 301-903-8350

Nancy C. Cole
Oak Ridge National Laboratory
P.O. Box 2008
4500, MS-6153
Oak Ridge, TN 37831-6084
(615) 574-4824
FAX 615-574-5118

Jeff Cook
University of Tennessee
Department of Materials Science
and Engineering
434 Dougherty Engineering Building
Knoxville, TN 37996-2200
(615) 974-5336
FAX 974-4115

Kevin Cooley
Oak Ridge National Laboratory
P.O. Box 2008
Oak Ridge, TN 37831-6063
(615) 574-4559

William Curtin
Virginia Polytechnic Institute & State
University
Department of Engineering Science
and Mechanics
College of Engineering
Blacksburg, VA 24061-0219
(703) 231-5316

Steve Dekanich
Martin Marietta Energy Systems, Inc.
P.O. Box 2003
Oak Ridge, TN 37830-7271
(615) 576-2288

Alan Dragoo
Department of Energy
Office of Basic Energy Sciences
Chief of Metallurgy and Ceramics Branch
ER-131
19901 Germantown Road
Germantown, MD 20874-1290
(301) 903-3428

John DuPont
Lehigh University
Whitaker Lab
5E. Packer Avenue
Bethleham, PA 18015
(610) 758-3942
FAX 610-758-4244

G. R. Edwards
Colorado School of Mines
Center for Welding and Joining Research
Golden, CO 80401
(303) 273-3773
FAX 303-273-3795

William A. Ellingson
Argonne National Laboratory
9700 South Cass Avenue
Argonne, IL 60439
(708) 252-5068
FAX 708-252-4798

Douglas Fain
Oak Ridge K-25 Site
P.O. Box 2003
1004-L, MS 7271
Oak Ridge, TN 37831-7271
(615) 574-9932
FAX 615-576-2930

Albert Z. Fresco
Dupont Lanxide Composites, Inc.
1300 Marrows Road
P.O. Box 6077
Newark, DE 19714-6077
(302) 456-6241

Thomas B. Gibbons
ABB Combustion Engineering
Power Plant Laboratories
1000 Prospect Hill Road
Windsor, CT 06095
(203) 285-3593

G. M. Goodwin
Oak Ridge National Laboratory
P.O. Box 2008
4508, MS-6096
Oak Ridge, TN 37831-6096
(615) 574-4809
FAX 615-574-7721

Robert Hallstrom
Quality Assurance Department
DB Riley, Inc.
5 Neponset Street
Worcester, MA 01606
(508) 854-3927
FAX 508-852-7548

Yirong He
Department of Materials Science & Engineering
The Ohio State University
477 Watts Hall
2041 College Road
Columbus, OH 43210
(614) 292-3373-
FAX 614-292-1537

E. E. Hoffman
U. S. Department of Energy
Oak Ridge Operations
P.O. Box 2008
MS-6269
Oak Ridge, TN 37831
(615) 576-0735

Linda Horton
Oak Ridge National Laboratory
P.O. Box 2008
Oak Ridge, TN 37831-6134
(615) 574-5081

John Hurley
University of North Dakota EERC
P.O. Box 9018 University Station
Grand Forks, ND 58202
(701) 777-5159
FAX 701-777-5181

Juhani Isaksson
A. Ahlstrom Corporation
Ahlstrom Pyropower
Kanslerinkatu 14
Fin 33720
Tampere,
Finland
358-31-316-5076
FAX 358-31-316-5078

Marit Jagtoyen
The University of Kentucky
Center for Applied Energy Research
3572 Iron Works Pike
Lexington, KY 40511-8433
(606) 257-0213

Mark Janney
Oak Ridge National Laboratory
P.O. Box 2008
4508, MS-6087
Oak Ridge, TN 37831-6087
(615) 574-4281

R. N. Johnson
Pacific Northwest Laboratory
P. O. Box 999, K3-59
Battelle Boulevard
Richland, WA 99352
(509) 375-6906
FAX 509-375-3864

Roddie R. Judkins
Oak Ridge National Laboratory
P.O. Box 2008
4508, MS-6084
Oak Ridge, TN 37831-6084
(615) 574-4572
FAX 615-574-5812

Bruce Kang
Mechanical & Aerospace Engineering Department
West Virginia University
P.O. Box 6106
Morgantown, WV 26506
(304) 293-3111
FAX 304-293-6689

James Kelly
Rolled Alloys
125 West Sterns Road
P.O. Box 310
Temperance, MI 48182
(313) 847-0561

Frank Ko
APD Inc.
2500 Pearl Buck Road
Bristol, PA 19007
(215) 785-3230

Libby Kupp
Pennsylvania State University
226 Steidle Building
University Park, PA 16802
(814) 865-3953
FAX 814-865-2917

Peter Liaw
The University of Tennessee
Department of Materials Science &
Engineering
434 Doughtery Engineering Building
Knoxville, TN 37996-2200
(615) 974-6356
FAX 615-974-4115

C. T. Liu
Oak Ridge National Laboratory
P.O. Box 2008
Oak Ridge, TN 37831-6156
(615) 574-4459

John P. Longwell
Department of Chemical Engineering
Massachusetts Institute of Technology
Room 66-456
Cambridge, MA 02139
FAX 617-258-5042

Rick Lowden
Oak Ridge National Laboratory
P.O. Box 2008
Oak Ridge, TN 37831-6087
(615) 576-2769

Subhaus G. Malghan
National Institute of Standards and
Technology
Materials Building 223/A256
Gaithersburg, MD 20899
(301) 975-6101
FAX 301-990-8729

Robert Mallett
Mallett Technology
100 Park Drive, Suite 204
P.O. Box 14407
Research Triangle Park, NC 27709
(919) 406-1500
FAX 919-549-9679

Mahendra Mathur
U.S. DOE/PETC
P.O. Box 10940
Pittsburgh, PA 15236
(412) 892-4605
FAX 412-892-5104

W. M. Matlin
The University of Tennessee
Department of Materials Science &
Engineering
434 Doughtery Engineering Building
Knoxville, TN 37996-2200
(615) 974-6356
FAX 615-974-4115

Phil Maziasz
Oak Ridge National Laboratory
P.O. Box 2008
MS-6115, 4500S
Oak Ridge, TN 37831-6114
(615) 574-5082

Claudette McKamey
Oak Ridge National Laboratory
P.O. Box 2008
MS-6114, 4500S
Oak Ridge, TN 37831-6114
(615) 574-6917

Jerry McLaughlin
Oak Ridge National Laboratory
P.O. Box 2008
Bldg. 4515, MS-6063
Oak Ridge, TN 37831-6063
(615) 574-4559

Theodore J. McMahon
U. S. Department of Energy
Morgantown Energy Technology Center
P.O. Box 880
MS CO4
Morgantown, WV 26505
(304) 285-4865
FAX 304-285-4403

Nguyen Minh
AlliedSignal
2525 W 190th Street
Department 93140, MS T-41
Torrance, CA 90504-6099
(310) 512-3515

John N. Mundy
U. S. Department of Energy
BES
Division of Material Sciences
ER-131, MSG 236
Washington, DC 20585
(301) 903-4271

K. Natesan
Argonne National Laboratory
9700 South Cass Avenue
Argonne, IL 60439
(708) 252-5103
FAX 708-252-3604

Dick Nixdorf
President
Cer-Wat Corporation
1701 Louisville Drive
Suite C
Knoxville, TN 37922
(615) 588-8342
FAX 615-588-3453

L. R. Pederson
Pacific Northwest Laboratory
MS K2/44
P.O. Box 999
Richland, WA 99352
(509) 375-2731
FAX 509-375-2186

Robert Perrin
The University of Tennessee
Department of Materials Science
and Engineering
434 Dougherty Engineering Building
Knoxville, TN 37996-2200
(615) 974-4858

Bruce Pint
Oak Ridge National Laboratory
P.O. Box 2008
Oak Ridge, TN 37831-6156
(615) 576-2897
FAX 615-574-5118

Doug Pysher
3M Company
3M Center
Bldg 201-4N-01
St. Paul, MN 55144-1000
(612) 737-1797
FAX 612-737-4682

C. Y. (Paul) Qiao
The University of Tennessee
Materials Science & Engineering Department
434 Dougherty Engineering Building
Knoxville, TN 37996-2200
(615) 974-5310
FAX 615-974-0880

Barry H. Rabin
Idaho National Engineering Laboratory
P.O. Box 1625
Idaho Falls, ID 83415
(208) 526-0058
FAX 208-526-0690

George Roettger
Oak Ridge K-25 Site
P.O. Box 2003
1004-L, MS-7271
Oak Ridge, TN 37831-7271
(615) 574-7539

Glenn Romanoski
Oak Ridge National Laboratory
P.O. Box 2008
4508, MS- 6088
Oak Ridge, TN 37831-6088
(615) 574-4838
FAX 615- 586-8424

Larry Ruth
Department of Energy
PETC
P.O. Box 10940
Pittsburgh, PA 15236
(412) 892-4461
FAX 412-892-5917

Stephen M. Sabol
Westinghouse Electric Corporation
4400 Alafaya Trail
MC-303
Orlando, FL 32826-2399
(407) 281-5136
FAX 407-281-2334

Sankar Sambasivan
BIRL
1801 Maple Avenue
Evanston, IL 60201
(708) 491-4619
FAX 708-467-1022

Vinod K. Sarin
Boston University
College of Engineering
44 Commington Street
Boston, MA 02215
(617) 353-6451
FAX 617-353-5548

Allen G. Sault
Sandia National Laboratories
Department 6211
P.O. Box 5800
Albuquerque, NM 87185
(505) 844-8723
FAX 505-845-9500

Otto J. Schwarz
Oak Ridge National Laboratory
P.O. Box 2008
Oak Ridge, TN 37831-6087
(615) 576-2769

Rodger Seeley
Babcock & Wilcox International
581 Coronation Blvd.
Cambridge, Ontario
Canada NIR 5V3

Dan Seery
United Technologies Research Center
411 Silver Lane
East Hartford, CT 06108
203) 727-7150
FAX 203-727-2151

Vinod Sikka
Oak Ridge National Laboratory
P.O. Box 2008
4508, MS-6083
Oak Ridge, TN 37831-6083
(615) 574-5112

Marvin I. Singer
U. S. Department of Energy
Fossil Energy
FE 70,
4G-052/FORS
Washington, DC 20585
(202) 586-1577

J. P. Singh
Argonne National Laboratory
Bldg. 212
9700 South Cass Avenue
Argonne, IL 60439
(708) 252-5123
FAX 708-252-3604

Robert G. Smith
3M Company
Bldg. 203-1-01
3M Center
St. Paul, MN 55144-1000
(612) 733-2564
FAX 612-737-5484

Karl Spear
Pennsylvania State University
118 Steidle Bldg
University Park, PA 16802
(814) 863-0990
FAX 814-865-2917

Thomas L. Starr
Georgia Institute of Technology
Materials Science and Engineering
Bunger-Henry Building, Room 276
Atlanta, GA 30332-0245
(404) 853-0579
FAX 404-853-9140

David P. Stinton
Oak Ridge National Laboratory
P.O. Box 2008
4515, MS-6063
Oak Ridge, TN 37831-6063
(615) 574-4556

N. S. Stoloff
Rensselaer Polytechnic Institute
Materials Engineering Department
Troy, NY 12180-3590
(518) 276-6371
FAX 518-276-8554

Robert W. Swindeman
Oak Ridge National Laboratory
P.O. Box 2008
MS-6155, 4500S
Oak Ridge, TN 37831-6155
(615) 574-5108
FAX 615-574-5118

Mike Tenhover
The Carborundum Company
P.O. Box 832
Niagara Falls, NY 14302

Peter F. Tortorelli
Oak Ridge National Laboratory
P.O. Box 2008
Oak Ridge, TN 37831-6156
(615) 574-5119

Mladen Trubelja
Pennsylvania State University
110 Steidle Bldg
University Park, PA 16802
(814) 865-0634
FAX 814-865-2917

Özer Ünal
Ames Laboratory
207 Metals Development
Ames, IA 50011
(515) 294-4892
FAX 515-294-8727

John Vaklyes, Jr.
CeraMem Separations
952 East Fir Street
Palmyra, PA 17078
(717) 838-7911
FAX 717-838-7880

Stuart Van Weele
Foster Wheeler
12 Peach Tree Hill Road
Livingston, NJ 07039
(908) 236-1463
FAX 908-236-1352

Norm Vaughn
Oak Ridge National Laboratory
P.O. Box 2008
Oak Ridge, TN 37831-6087
(615) 576-2769

Srinath Viswanathan
Oak Ridge National Laboratory
P.O. Box 2008
4508, MS-6083
Oak Ridge, TN 37831-6083
(615) 576-9917

Jim Wessel
Dow Corning Corporation
1800 M Street, NW
Washington, DC 20036
(202) 785-0585
FAX 202-785-0421

Jeff Williams
Oak Ridge National Laboratory
P.O. Box 2008
Oak Ridge, TN 37831-6063
(615) 576-2896

Ian Wright
Oak Ridge National Laboratory
4500S, MS-6156
P.O. Box 2008
Oak Ridge, TN 37831-6156
(615) 574-4451
FAX 615-574-5118

Jill K. Wright
Idaho National Engineering Laboratory
P.O. Box 1625
Idaho Falls, ID 83415-2218
(208) 526-9723
FAX 208 526-0690

Richard N. Wright
Idaho National Engineering Laboratory
P.O. Box 1625
Idaho Falls, ID 83415-2218
(208) 526-6127
FAX 208 526-0690

Kim A. Wynns, P.E.
Alon Processing, Inc.
Grantham Street
Tarentum, PA 15084
1-800-367-2556

CONF-9505204
ORNL/FMP-95/1

INTERNAL DISTRIBUTION

1.	D. J. Alexander
2.	P. Angelini
3.	R. L. Beatty
4.	T. M. Besmann
5.	A. Bleir
6.	R. A. Bradley
7.	K. Breder
8.	T. D. Burchell
9.	J. Canon
10.	P. T. Carlson
11-14.	N. C. Cole
15.	K. M. Cooley
16.	S. DeKanich
17.	J. R. DiStefano
18.	D. E. Fain
19.	G. M. Goodwin
20.	L. L. Horton
21.	M. A. Janney
22-24.	R. R. Judkins
25.	M. A. Karnitz
26.	J. R. Keiser
27.	W. Y. Lee
28.	C. T. Liu
29.	R. A. Lowden
30.	W. M. Matlin
31.	P. J. Maziasz
32.	D. J. McGuire
33.	C. G. McKamey
34.	J. C. McLaughlin
35.	K. L. More
36.	A. Pasto
37.	B. Pint
38.	G. E. Roettger
39.	G. R. Romanoski
40.	A. C. Schaffhauser
41.	J. H. Schneibel
42.	O. J. Schwarz
43.	J. Sheffield
44.	V. K. Sikka
45.	P. S. Sklad
46.	D. P. Stinton
47.	R. W. Swindeman
48.	T. N. Tiegs
49.	N. Vaughn
50.	P. F. Tortorelli
51.	S. Viswanathan
52.	J. Williams
53.	D. F. Wilson
54.	I. G. Wright
55-56.	Central Research Library
57.	Document Reference Section
58.	ORNL Patent Section
59-60.	Laboratory Records Department
61.	Metals and Ceramics Records Office
62.	LRD-RC

EXTERNAL DISTRIBUTION

63-66. 3M COMPANY, 3M Center, St. Paul, MN 55144
J. H. Eaton (Bldg 203-1-01)
M. L. Leitheiser
D. Pysher
R. G. Smith (Bldg 203-1-01)

67. A. AHLSTROM CORPORATION, Ahlstrom Pyropower, Kanslerinkatu 14,
Fin 33720, Tampere, Finland
J. Isaksson

68. ABB Lummus Crest, 15 Broad St., Bloomfield, NJ 07003
M. Greene

69. ABB COMBUSTION ENGINEERING, 911 W. Main St.,
Chattanooga, TN 37402
D. A. Canonico

70. ABB COMBUSTION ENGINEERING, 1000 Prospect Hill Road,
Windsor, CT 06095
T. B. Gibbons

71. ADIABATICS, INC., 3385 Commerce Dr., Columbus, IN 47201
P. Badgley

72. ADVANCED REFRACTORY TECHNOLOGIES, INC., 699 Hertel Avenue,
Buffalo, NY 14207
K. A. Blakely

73. AEA INDUSTRIAL TECHNOLOGY, Harwell Laboratory, Materials
Development Division, Bldg. 393, Didcot, Oxfordshire,
OX110RA ENGLAND
H. Bishop

74. AIR PRODUCTS AND CHEMICALS, INC., 7201 Hamilton Blvd.,
Allentown, PA 18195-1501
P. Dyer

75. ALBERTA RESEARCH COUNCIL, Oil Sands Research Department,
P. O. Box 8330, Postal Station F, Edmonton, Alberta,
CANADA T6H5X2
L. G. S. Gray

76. ALLEGHENY LUDLUM STEEL, Technical Center, Alabama and Pacific
Avenues, Brackenridge, PA 15014
J. M. Larsen

77. ALLIEDSIGNAL, 2525 W 190th Street, Dept. 93140,
Torrance, CA 90504-6099
N Minh (MS T-41)

78. ALLIEDSIGNAL ENGINES, 111 S. 34th Street,
Phoenix, AZ 85071-2181
T. Strangman (MS 553-12)

79. ALLISON ENGINE COMPANY, Materials Engineering, P.O. Box 420,
Indianapolis, IN 46206-0420
L. E. Groseclose

80-82. ALLISON GAS TURBINE DIVISION, P. O. Box 420, Indianapolis, IN
46206-0420
P. Khandalwal (Speed Code W-5)
R. A. Wenglarz (Speed Code W-16)
J. R. Whetstone

83-84. ALON PROCESSING, INC., Grantham Street, Tarentum, PA 15084
W. P. Heckel, Jr.
K. A. Wynns

85. AMAX R&D CENTER, 5950 McIntyre St., Golden, CO 80403
T. B. Cox

86-87. AMERCOM, Advanced Material Division, Atlantic Research Corporation
8928 Fullbright Avenue, Chatsworth, CA 91311
J. O. Bird
W. E. Bustamante

88. AMOCO CHEMICAL COMPANY, P. O. Box 3011, D-2,
Naperville, IL 60566-7011
N. Calamur

89. ANSTO, New Illawarra Rd, Lucas Heights NSW 2234 PMB,
1 Menai NSW 2234, Australia
A.B.L. Croker

90. APD INC., 2500 Pearl Buck Road, Bristol, PA 19007
F. Ko

91. A. P. GREEN REFRACTORIES COMPANY, Green Blvd.,
Mexico, MO 65265
J. L. Hill

92-94. ARGONNE NATIONAL LABORATORY, 9700 Cass Ave.,
Argonne, IL 60439
W. A. Ellingson
K. Natesan
J. P. Singh

95. ARMY MATERIALS TECHNOLOGY LABORATORY SLCMT-MCC,
Watertown, MA 02172-0001
D. R. Messier

96. AVCO RESEARCH LABORATORY, 2385 Revere Beach Parkway,
Everett, MA 02149
R. J. Pollina

97-98. BABCOCK & WILCOX, Domestic Fossil Operations,
20 South Van Buren Ave., Barberton, OH 44023
M. Gold
D. Wasyluk

99-102. BABCOCK & WILCOX, Lynchburg Research Center, P. O. Box 11165,
Lynchburg, VA 24506
R. Goettler
J. A. Heaney
W. Long
H. H. Moeller

103. BABCOCK & WILCOX INTERNATIONAL, 581 Coronation Blvd.,
Cambridge, Ontario, Canada N1R 5V3
R. Seeley

104. BATTELLE COLUMBUS LABORATORIES, 505 King Ave.,
Columbus, OH 43201
D. Anson

105. BENNETT, Michael J., Three Chimneys, South Moreton Oxon, United Kingdom

106-107. BETHLEHEM STEEL CORPORATION, Homer Research Laboratories,
Bethlehem, PA 18016
B. L. Bramfitt
J. M. Chilton

108-109. BIRL, 1801 Maple Avenue, Evanston, IL 60201
D. Boss
S. Sambasivan

110. BLACK & VEATCH, 11401 Lamar, Overland Park, KS 66211
M. Bary

111. BOSTON UNIVERSITY, 44 Washington Street, Boston, MA 02215
V. K. Sarin

112-115. BRITISH COAL CORPORATION, Coal Technology Development Division,
P. O. Box 199, Stoke Orchard, Cheltenham, Glocester, ENGLAND GL52 4ZG
J. Oakey
N. Sims
M. A. Smith
I. Summerfield

116-117. CANADA CENTER FOR MINERAL & ENERGY TECHNOLOGY,
568 Booth St., Ottawa, Ontario Canada K1A OG1
R. W. Revie
M. Sahoo

118. CATERPILLAR INC., Technology Center, P.O. Box 1875,
Perioria, IL 61656-1875
D. I. Biehler

119. CERAMEM SEPARATIONS, 952 Eat Fir Street, Palmyra, PA 17078
J. Vaklyes, Jr.

120. CER-WAT CORPORATION, INC., 1701 Louisville Dr., Suite C,
Knoxville, TN 37921
D. Nixdorf

121. CHEVRON RESEARCH & TECHNOLOGY COMPANY, 100 Chevron Way,
Richmond, CA 94802-0627
D. J. O'Rear

122. CIEMAT, Avda. Complutense, 22, 28040-Madrid (SPAIN)
G. M. Calvo

123. COAL & SYNFUELS TECHNOLOGY, 1401 Wilson Blvd., Suite 900,
Arlington, VA 22209
E. Tilley-Hinkle

124. COAL & SYNFUELS TECHNOLOGY, 1616 N. Fort Myer Dr., Suite 1000,
Arlington, VA 22209
J. Bourbin

125-126. COAL TECHNOLOGY CORPORATION, 103 Thomas Road,
Bristol, VA 24201
R. A. Wolfe
R. E. Wright

127. COLORADO SCHOOL OF MINES, Dept. of Metallurgical Engineering,
Golden, CO 80401
G. R. Edwards

128-130. CONSOLIDATION COAL COMPANY, 4000 Brownsville Road,
Library, PA 15129
F. P. Burke
S. Harding
D. Nichols

131. CORNING INCORPORATED, SP-DV-1-9, Corning, NY 14831
P. Bardhan

132. CUMMINS ENGINE COMPANY, Box 3005, MC 50183,
Columbus, IN 47202-3005
T. M. Yonushonis

133. DB Riley, Inc., 5 Neponset Street, Worcester, MA 01606
R. Hallstrom

134. DEVASCO INTERNATIONAL, INC., 9618 W. Tidwell,
Houston, TX 77041
J. L. Scott

135. J. DOWICKI, P.E., 19401 Framingham Dr., Gaithersburg,
MD 20879

136. DUPONT LANXIDE COMPOSITES, INC., Pencader Plant, Box 6100,
Newark, DE 19714-6100
J. K. Weddell

137-138. DUPONT LANXIDE COMPOSITES, INC., 1300 Marrows Road,
P.O. Box 6077, Newark, DE 19714-6077
A. Z. Fresco
D. Landini

139. EC TECHNOLOGIES, INC., 3614 Highpoint Dr.,
San Antonio, TX 78217
D. J. Kenton

140-142. EG&G IDAHO, INC., Idaho National Engineering Laboratory,
P.O. Box 1625, Idaho Falls, ID 83415
B. H. Rabin
R. N. Wright
J. K. Wright

143-147. ELECTRIC POWER RESEARCH INSTITUTE, P.O. Box 10412,
3412 Hillview Avenue, Palo Alto, CA 94303
W. T. Bakker
R. A. Brown
S. Gehl
R. Goldstein
J. Stringer

148. ENERGY AND ENVIRONMENTAL RESEARCH CENTER, Box 8213,
University Station, Grand Forks, ND 58202
J. P. Hurley

149. ENERGY AND WATER RESEARCH CENTER, West Virginia University,
Morgantown, WV 26505-5054
C. L. Irwin

150. ENVIRONMENTAL PROTECTION AGENCY, Global Warming Control
Division (MD-63), Research Triangle Park, NC 27711
K. T. Janes

151. ERC, INC., P. O. Box 417, Tullahoma, TN 37388
Y. C. L. Susan Wu

152-153. EXXON RESEARCH AND ENGINEERING COMPANY, Clinton Township,
Route 2 East, Annandale, NJ 08801
M. L. Gorbaty
S. Soled

154. FERRO CORPORATION, Filtros Plant, 603 West Commercial St.
E., Rochester, NY 14445
P. S. Way

155. FORSCHUUGS ZENTRUM JÜLICH GmbH, ICT, Postfach 1913, D-5170
Jülich, Germany
H. Barnert-Wiemer

156-157. FOSTER WHEELER DEVELOPMENT CORPORATION, Materials
Technology Dept., John Blizard Research Center, 12 Peach Tree Hill
Road, Livingston, NJ 07039
J. L. Blough
S. Van Wheele

158. FRAUNHOFER-INSTITUT für WERKSTOFFMECHANIK, Wohlerstrass 11,
79108 Freiburg, West Germany
R. Westerheide

159. GAS RESEARCH INSTITUTE, 8600 West Bryn Mawr Avenue,
Chicago, IL 60631
H. S. Meyer

160. GENERAL APPLIED SCIENCE LABS, 77 Raynor Avenue,
Ronkonkoma, NY 11779
M. Novack

161. GEORGIA INSTITUTE OF TECHNOLOGY, Georgia Tech Research
Institute, 123D Baker Bldg., Atlanta, GA 30332-0245
T. L. Starr

162. GRI, 8600 W. Bryn Mawr, Chicago, IL 60656
D. Scarpiello

163. HAYNES INTERNATIONAL, INC., 1020 W. Park Avenue,
Kokomo, IN 46904
G. Y. Lai

164-165. HOSKINS MANUFACTURING COMPANY, 10776 Hall Rd.,
Hamburg, MI 48139
R. B. Brennan
F. B. Hall

166. ILLINOIS INSTITUTE OF TECHNOLOGY, METM Dept., Perlstein Hall,
IIT, Chicago, IL 60616
J. A. Todd-Copley

167. INCO ALLOYS INTERNATIONAL, INC., P. O. Box 1958,
Huntington, WV 25720
S. Tassen

168. INTECH, INC., 11316 Roven Dr., Potomac, MD 20854-3126
P. Lowe

169-170. IOWA STATE UNIVERSITY, Ames Laboratory, 107 Metals Development,
Ames, IA 50011
D. J. Sordelet
Ozer Unal

171. LIQUID CARBONIC INDUSTRIAS S.A, Avenida Rio Branco, 57-6° Andar,
Centro - 20090-004, Rio De Janeiro, Brazil
M. Saddy

172. JET PROPULSION LABORATORY, 4800 Oak Grove Dr., MS-79-21,
Pasadena, CA 91020
R. L. Chen

173. LANXIDE CORPORATION, 1 Tralee Industrial Park, Newark, DE 19711
E. M. Anderson

174. LAVA CRUCIBLE-REFRACTORIES CO., P.O. Box 278,
Zelienople, PA 16063
T. Mulholland

175-179. LAWRENCE BERKELEY LABORATORY, University of California,
1 Cyclotron Road, Berkeley, CA 94720
I. Brown - MS 53
T. M. Devine
P. Y. Hou - MS 62-203
G. Rosenblatt
S. Visco

180. LAWRENCE LIVERMORE NATIONAL LABORATORY, P.O. Box 808,
Livermore, CA 94551
J. H. Richardson (L-353)

181. LEHIGH UNIVERSITY, Energy Research Center, 5 E Packer Avenue,
Bethlehem, PA 18015
J. N. DuPont

182-184. LOCKHEED MARTIN-KAPL, P.O. Box 1072, MS G2-312,
Schenectady, NY 12301
J. J. Letko (MS D2-121)
G. A. Newsome
J. Woods

185. E. LORIA, 1829 Taper Drive, Pittsburgh, PA 15241

186-189. LOS ALAMOS NATIONAL LABORATORY, P.O. Box 1663,
Los Alamos, NM 87545
P. Apen - MS D453
R. G. Castro - MS G720
J. D. Katz
D. Phillips

190. LURGI LENTJES BABCOCK, Duisburger Strasse 375, D-46041 Oberhausen,
Germany
G. von Wedel

191. MALLETT TECHNOLOGY, 100 Park Drive, Suite 204, P.O. Box 14407,
Research Triangle Park, NC 27709
R. Mallett

192-193. MANUFACTURING SCIENCES CORPORATION, 804 Kerr Hollar Road,
Oak Ridge, TN 37830
R. Hayes
T. Muth

194. MASSACHUSETTS INSTITUTE OF TECHNOLOGY, Department of Chemical
Engineering, Room 66-456, Cambridge, MA 02139
J. Longwell

195. MER CORPORATION, 7960- S. Kolb Road, Tucson, AZ 85706
L. Leaskey

196-197. MOBIL RESEARCH & DEVELOPMENT CORPORATION,
P. O. Box 1026, Princeton, NJ 08540
R. E. Searles
S. T. Viscontini

198-201. NASA LEWIS RESEARCH CENTER, 21000 Brookpark Road,
Cleveland, OH 44135
J. P. Gyekenyesi
N. Jacobson - MS 106-1
S. R. Levine
R. Miller - MS 24-1

202-204. NATIONAL INSTITUTE OF STANDARDS AND TECHNOLOGY, Materials
Building, Gaithersburg, MD 20899
S. J. Dapkunas
L. K. Ives (Bldg. 220, Rm. A-215)
S. G. Malghan

205. NATURAL GAS AND OIL TECHNOLOGY PARTNERSHIP, 12434 Penthshire,
Houston, TX 77024
R. M. Whitsett

206. NEW ENERGY AND INDUSTRIAL TECHNOLOGY DEVELOPMENT
ORGANIZATION, 1800 K Street, N.W., Suite 924,
Washington, DC 20006
T. Fukumizu

207-209. NEW ENERGY AND INDUSTRIAL TECHNOLOGY DEVELOPMENT
ORGANIZATION, Sunshine 60 Bldg., P.O. Box 1151,
1-1 Higashi-Ikebukuro 3-Chome, Toshima-Ku, Tokyo, 170, Japan
S. Hirano
H. Narita
S. Ueda

210-211. NETHERLANDS ENERGY RESEARCH FOUNDATION ECN,
P.O. Box 1, 1755 ZG Petten, The Netherlands
P. T. Alderliesten
M. Van de Voorde

212. NORCONTROL, Duran Marquina 20, 15080 La Coruna, Spain
S. Gomez

213. NORTH CAROLINA A&T STATE UNIVERSITY, Department of Mechanical Engineering, Greensboro, NC 27411
J. Sankar

214. OFFICE OF NAVAL RESEARCH, Code 431, 800 N. Quincy St.,
Arlington, VA 22217
S. G. Fishman

215-216 OHIO STATE UNIVERSITY, Department of Metallurgical Engineering,
116 W. 19th Avenue, Columbus, OH 43210
Y. He
R. A. Rapp

217-219. PACIFIC NORTHWEST LABORATORIES, P.O. Box 999,
Richland, WA 99352
J. L. Bates
R. N. Johnson
L. R. Pederson

220. PALL CORPORATION, 5E Packer Avenue, Whitaker Laboratory #5,
Bethlehem, PA 18015
Tanweer Haq

221-224. PENNSYLVANIA STATE UNIVERSITY, 101 Steidle Building,
University Park, PA 16802
L. Kupp
K. Spear
R. Tressler
M. Trubelja

225. PSI TECHNOLOGY COMPANY, 20 New England Business Center,
Andover, MA 01810
L. Bool

226. RENSSELAER POLYTECHNIC INSTITUTE, Materials Engineering Department, Troy, NY 12180-3590
N. S. Stoloff

227. RIBBON TECHNOLOGY CORPORATION, P.O. Box 30758,
Columbus, OH 43230
T. Gaspar

228. RILEY STOKER CORPORATION, 5 Neponset Street, Worcester, MA 01606
D. P. Kalmanovitch

229. RISO NATIONAL LABORATORY, P.O. Box 49, DK-4000, Roskilde,
DENMARK
Aksel Olsen

230. ROLLED ALLOYS, 125 West Sterns Road, Temperance, MI 48182
J. C. Kelly

231. SANDIA NATIONAL LABORATORIES, 7011 East Avenue, P.O. Box 969
Livermore, CA 94551-0969
J. E. Smugeresky (MS-9402)

232-237. SANDIA NATIONAL LABORATORIES, P.O. Box 5800,
Albuquerque, NM 87185
L. L. Baxter
R. Bradshaw
R. Buss
G. Carlson
G. Samara
A. Sault

238-239. SARGENT AND LUNDY, 55 E Monroe Street, Chicago, IL 60603
R. J. Kerhin
D. G. Sloat

240-241. SCIENCE APPLICATIONS INTERNATIONAL CORPORATION,
1710 Goodridge Dr., McLean, VA 22102
J. T. Bartis
J. Ward (MS 2-20-1)

242. SFA PACIFIC, INC., 444 Castro Street, Suite 920, Mountain View, CA 94041
N. Korens

243. SHELL DEVELOPMENT COMPANY, P.O. Box 1380,
Houston, TX 77251-1380
L. W. R. Dicks

244. G. SORELL, 49 Brookside Terrace, N. Caldwell, NJ 07006

245. SOUTHERN RESEARCH INSTITUTE, 2000 Ninth Avenue South,
Birmingham, AL 35202
H. S. Starrett

246. SOUTHWEST RESEARCH INSTITUTE, 6620 Culebra Road,
P.O. Drawer 28510, San Antonio, TX 78284
F. F. Lyle, Jr.

247. SRI INTERNATIONAL, 333 Ravenswood Avenue, Meno Park, CA 04025
Y. D. Blum

248. SRS TECHNOLOGIES, 990 Explorer Blvd., Huntsville, AL 35806
J. H. Laue

249. STANTON ENERGY INDUSTRY CONSULTANTS, INC., RD #1, Liberty Court,
New Stanton, PA 15672-9621
R. J. Steffen

250. STATE ELECTRICITY COMMISSION OF VICTORIA, Herman Research
Laboratory Library, Howard St., Richmond, Victoria, 3121 Australia
H. Hodgskiss

251-252. STRESS ENGINEERING SERVICES, INC., 415 Glensprings Drive, Suite 200,
Cincinnati, OH 45246
C. Haynes
D. Marriott

253. SUNDSTRAND, 4747 Harrison Ave., Rockford, IL 61125
D. Oakey

254. SUPERKINETICS, 2881 Tramway Place, NE,
Albuquerque, NM 87122
J. V. Milewski

255. TECHNIWEAVE, INC., 109 Chestnut Hill Road, Rochester, NH 03868
J. A. LeCoustaouec

256. TECHNOLOGY ASSESSMENT AND TRANSFER, 133 Defense Highway,
Suite 212, Annapolis, MD 21401
J. Hanigofsky

257. TECHNOLOGY MANAGEMENT INC., 9718 Lake Shore Blvd.,
Cleveland, OH 44108
B. P. Lee

258. TELEDYNE ALLVAC, P.O. Box 5030, Monroe, NC 28110
A. L. Coffey

259-260. TENNESSEE VALLEY AUTHORITY, 3N66A Missionary Ridge Place,
Chattanooga, TN 37402-2801
J. B. Brooks
C. M. Huang

261. TEXAS EASTERN TRANSMISSION CORPORATION, P.O. Box 2521,
Houston, TX 77252
D. H. France

262. THE AMERICAN CERAMIC SOCIETY, INC., 735 Ceramic Place,
Westerville, OH 43081
L. Sheppard

263. THE CARBORUNDUM COMPANY, Technology Division, P. O. Box 832,
Niagara Falls, NY 14302
M. Tenhover

264. THE JOHNS HOPKINS UNIVERSITY, Materials Science & Engineering,
Maryland Hall, Baltimore, MD 21218
R. E. Green, Jr.

265. THE MATERIALS PROPERTIES COUNCIL, INC., United Engineering
Center, 345 E. Forty-Seventh St., New York, NY 10017
M. Prager

266. THE NORTON COMPANY, High Performance Ceramics Division,
Goddard Road, Northboro, MA 01532-1545
N. Corbin

267. THE RALPH M. PARSONS COMPANY, 100 West Walnut St.,
Pasadena, CA 91124
J. B. O'Hara

268. THE TORRINGTON COMPANY, Advanced Technology Center, 59 Field
Street, Torrington, CT 06790
W. J. Chmura

269. THIRD MILLENNIUM TECHNOLOGY, INC., 120 Sherlake Drive,
P.O. Box 23556, Knoxville, TN 37933-1556
C. F. VanConant

270. TRW, 1455 E. 195th Street, Cleveland, OH 44110
M. Kurup

271-273. UNITED TECHNOLOGIES RESEARCH CENTER, Materials Department,
411 Silver Lane, East Hartford, CT 06108
N. S. Bornstein
J. E. Holowczak
D. Seery

274. UNIVERSITY OF CALGARY, 2500 University Dr. NW, Calgary, Canada
S. X. Mao

275. UNIVERSITY OF CALIFORNIA, Department of Materials Science and
Mineral Engineering, University of California, Building 66-Room 247,
Berkeley, CA 94720
R. O. Richie

276-277. UNIVERSITY OF KENTUCKY, Center for Applied Energy Research,
3572 Iron Works Pike, Lexington, KY 40511-8433
F. Derbyshire
M. Jagtoyen

278. UNIVERSITY OF NORTH DAKOTA, P.O. Box 9018, University Station,
Grand Forks, ND 58202
J. P. Hurley

279. UNIVERSITY OF PITTSBURGH, Materials Science & Engineering
Department, 848 Brenedum Hall, Pittsburgh, PA 15261
N. Birks

280. UNIVERSITY OF SOUTH AUSTRALIA, Department of Metallurgy,
The Levels SA 5095 Australia
K. N. Strafford

281-286. UNIVERSITY OF TENNESSEE, Department of Materials Science and
Engineering, 434 Doughtery Engineering Building, Knoxville, TN 37996
N. Biery
R. A. Buchanan
P. Liaw
C. D. Lundin
R. Perrin
P. Qiao

287-289. UNIVERSITY OF TENNESSEE SPACE INSTITUTE, Tullahoma,
TN 37388
W. H. Boss
J. W. Muehlhauser
M. White

290. UNIVERSITY OF WASHINGTON, Department of Materials Science and
Engineering, 101 Wilson, FB-10, Seattle, WA 98195
T. G. Stoebe

291. UOP, 50 E. Algonquin Road, Des Plaines, IL 60017-5016
G. J. Antos

292-293. U.S. BUREAU OF MINES, Tuscaloosa Research Center, P. O. Box L,
Tuscaloosa, AL 35486
J. C. Debsikdar
J. Kwong

294. U.S. BUREAU OF MINES, P. O. Box 70, Albany, OR 97321
J. Woodyard

295. U.S. DEPARTMENT OF TREASURY, 1500 Pennsylvania Ave., N.W., Rm. 5132, Washington, DC 20220
J. Benton

296. VEBA OEL, P. O. Box 45, 4650 Gelsenkirchen-Buer, Germany
D. Fuhrmann

297-298. VIRGINIA POLYTECHNIC INSTITUTE AND STATE UNIVERSITY, Department of Materials Engineering, Blacksburg, VA 24061
W. Curtin
K. L. Reifsnyder

299. WESSEL, James K., 127 Westview Lane, Oak Ridge, TN 37830

300-301. WEST VIRGINIA UNIVERSITY, Mechanical & Aerospace Engineering Department, P.O. Box 6106, Morgantown, WV 26505
B. Kang
B. Cooper

302. WESTERN RESEARCH INSTITUTE, 365 N. 9th Street, P. O. Box 3395, University Station, Laramie, WY 82071
V. K. Sethi

303. WESTINGHOUSE ELECTRIC CORPORATION, 4400 Alafaya Trial, Orlando, FL 32826-2399
S. M. Sabol - MC 303

304-308. WESTINGHOUSE ELECTRIC CORPORATION, Research and Development Center, 1310 Beulah Road, Pittsburgh, PA 15235-5098
M. A. Alvin
G. Bruck
D. L. Keairns
T. Lippert
S. C. Singhal

309. WORCESTER POLYTECHNIC INSTITUTE, 100 Institute Road, Worcester, MA 01609
E. Ma

310. DOE CHICAGO OPERATIONS OFFICE, 9800 S. Cass Ave., Argonne, IL 60439
J. Jonkouski

311. DOE IDAHO OPERATIONS OFFICE, 765 DOE Place, Idaho Falls,
ID 83406
J. B. Malmo

312-326. DOE MORGANTOWN ENERGY TECHNOLOGY CENTER,
P.O. Box 880, Morgantown, W VA 26505
C. T. Alsup
R. A. Bajura
R. C. Bedick
D. C. Cicero
F. W. Crouse, Jr.
R. A. Dennis
U. Grimm
J. S. Halow
N. T. Holcombe
W. J. Huber
T. J. McMahon
W. R. Miller
H. M. Ness
J. E. Notestein
C. M. Zeh

327-328. DOE OAK RIDGE OPERATIONS OFFICE, Oak Ridge, P. O. Box 2008,
Oak Ridge, TN 37831-6269
Assistant Manager for Energy Research and Development
E. E. Hoffman
M. H. Rawlins

329-330. DOE OFFICE OF BASIC ENERGY SCIENCES, Materials Sciences Division,
ER-131, 19901 Germantown Road, Germantown, MD 20874-1290
A. Dragoo
J. N. Mundy

331. DOE OFFICE OF COAL TECHNOLOGY, FE-232 GTN,
Washington, DC 20585
M. Perlsweig

332. DOE OFFICE OF ENERGY EFFICIENCY AND RENEWABLE ENERGY,
CE-12, Forrestal Building, Washington, DC 20545
J. J. Eberhardt

333-334. DOE OFFICE OF ENERGY RESEARCH, 14 Goshen Court,
Gaithersburg, MD 20882-1016
N. F. Barr
F. J. Wobber

335-342. DOE OFFICE OF FOSSIL ENERGY, Washington, DC 20585
W. Fedarko (FE-232)
K. N. Frye (FE-13)
S. C. Jain (FE-231)
C. E. Pax (FE 73)
T. B. Simpson (FE-231)
M. I. Singer (FE-70)
H. E. Thomas (FE-73)
G. F. Wheeler (FE-231)

343. DOE OFFICE OF INDUSTRIAL TECHNOLOGIES, 1000 Independence Avenue
S.W., Washington, DC 20585
S. Dillich (EE-20)

344. DOE OFFICE OF NAVAL REACTORS, NE-60, Crystal City Bldg.,
N.C.-2, Washington, DC 20585
J. Mosquera

345. DOE OFFICE OF PETROLEUM RESERVES, Analysis Division, FE-431,
1000 Independence Ave., Washington, DC 20585
D. de B. Gray

346-358. DOE PITTSBURGH ENERGY TECHNOLOGY CENTER,
P. O. Box 10940, Pittsburgh, PA 15236
A. H. Baldwin
J. L. Balzarini
R. A. Carabetta
R. C. Dolence
P. Goldberg
J. D. Hickerson
J. J. Lacey
S. R. Lee
M. E. Mather
G. V. McGurl
J. A. Ruether
L. Ruth
T. M. Torkos

359-360. DOE, OFFICE OF SCIENTIFIC AND TECHNICAL INFORMATION,
P.O.Box 62, Oak Ridge, TN 37831

For distribution by microfiche as shown in DOE/OSTI-4500,
Distribution Category UC-114 (Coal Based Materials and Components)